UNIVERSITY OF BELGRADE
FACULTY OF PHYSICS

Bojan V. Zlatkovic

FOUR WAVE MIXING IN HOT POTASSIUM VAPOR

Doctoral Dissertation

Belgrade, 2022

UNIVERZITET U BEOGRADU
FIZICKI FAKULTET

Bojan V. Zlatkovic

ČETVOROTALASNO MEŠANJE U PARI KALIJUMA

Doktorska disertacija

Beograd, 2022

Abstract

In this dissertation we present the investigation of optical non-degenerate four wave mixing (FWM) in co-propagating geometry and slowing of the short light pulses in hot vapor of potassium ^{39}K atoms. The enhancement of nonlinear coefficients is achieved by using the double-Λ scheme implemented on the D1 line of ^{39}K between hyperfine sublevels of the ground-state $^4S_{1/2}$ and the first excited state $^4P_{1/2}$ and the quantum coherence established between $F = 1$ and $F = 2$ sublevels of the ground-state by the strong pump beam.

In the first part of the thesis we've investigated the efficiency of the FWM process under different experimental circumstances and were set the find the values of experimental parameters that maximize it. The main figure of merit is the gain of the probe and the conjugate beam which represent the intensity amplification factor of these beams in the FWM process.

The dependence of the of gain on one-photon detuning reveals the competition between two effects - FWM and one-photon absorption. Both processes are inversely proportional to the one-photon detuning and we set out to find the point of best trade-off between them. The best result found was for 700 MHz where we measured the conjugate gain of 82. In all of the measurements we have adjusted the two-photon detuning to account for the AC Stark shift introduced by the strong pump. The strength of AC Stark shift effect drops as we move away from the resonance which was verified by the smaller value of two-photon detuning needed for obtaining the maximal gain for higher values of one-photon detuning.

Dependence on temperature, the angle between the pump and the probe and on the pump intensity were also investigated. The increase in temperature leads both to the increase of the concentration of potassium atoms and and hence to the increase of cross-coupling susceptibilities responsible to FWM on one side and to the increase of Doppler width and one-photon absorption on the other. Due to this effects the higher gain for conjugate at higher temperatures wasn't observed but we did measure the highest gain of 63 for the probe beam at $150°C$. Like in other alkali vapors a small angle between the pump and the probe was needed for achieving the best phase matching. In the case of potassium that angle was measured to be 2 mrad. Finally we were able to observe FWM for low pump intensities achievable by conventional diode lasers which opens up the possibility of investigation these kind of phenomena with less expensive and more maintainable types of lasers.

Next we've searched for the optimum experimental parameters that would give the best results for the slowing of short Gaussian light pulses in terms of fractional delay and fractional broadening. The best results achieved was the fractional delay of 1.1 with the fractional broadening of 1.2 for pulse length of τ = 120 ns and δ = 2 MHz, Δ = 1 GHz, T = 120^oC, I_{pump} = 200 mW, I_{ref} = 20μW, Θ = 3mrad with the probe gain of 16. Subsequent research has showed a rather flat dependency on two-photo detuning and the pump intensity which stands in contrast with the investigation in rubidium and sodium.

We've also performed research over several lengths of Gaussian light pulses. With lowering the temporal width of the light pulse its width in frequency domain increases which leads to the different slowing of larger number of Fourier components and to the larger broadening of the light pulse. In that sense the optimal length of the light pulse which would have a fractional delay larger than one (a condition needed for the use of short light pulses in optical delay lines) and minimal broadening was 120 ns.

We have also compared our results with the results of slowing pulses in sodium and rubidium vapor and concluded that results in potassium are better or comparable for similar experimental conditions.

Keywords: Four Wave Mixing, Potassium, Slow Light

Scientific field: Physics

Research area: Quantum optics, Nonlinear optics

Sažetak

U ovoj disertaciji je predstavljeno istraživanje optičkog nedegenerisanog četvorotalasnog mešanja (ČTM) u kopropagirajućoj geometriji i usporavanje kratkih svetlosnih impulsa u toploj pari atoma kalijuma ^{39}K. Pojačavanje nelinearnih koeficijenata ostvarano je korišćenjem dvostruke Λ šeme implementirane na D1 liniji ^{39}K izmedju hiperfinih podnivoa osnovnog stanja $^4S_{1/2}$i prvog ekscitovanog stanja $^4P_{1/2}$ i kvantne koherencije ostvarene izmedju $F = 1$ i $F = 2$ podnivoa osnovnog stanja delovanjem jakog pumpnog snopa.

U prvom delu teze istraživana je efikasnost ČTM u različitim eksperimentalnim uslovima sa ciljem nalaženja vrednosti eksperimentalnih parametara koji je maksimalizuju. Glavna merena veličina je pojačanje probnog i konjugovanog snopa. Ona predstavlja faktor pojačanja ovih snopova u procesu ČTM.

Zavisnost pojačanja od jednofotonskog razdešenja otkriva kompeticiju izmedju dva efekta - ČTM i jednofotonske apsorpcije. Oba procesa su obrnuto proporcionalna jednofotonskom razdešenju i cilj je bio naći tačku kompromisa izmedju njih. Najbolji rezultat je postignut za 700 MHz gde je izmereno pojačanje konjugovanog snopa od 82. U svim merenjima dvofotonsko razdešenje je podešavano tako da poništi uticaj AC Štarkovog pomeraja koji se javlja usled delovanja jakog pumpnog snopa. Jačina efekta AC Štarkovog pomeraja opada sa odmicanjem od rezonance što se može videti iz manje vrednosti dvofotonskog razdešenje potrebnog za anuliranje ovog efekta za veće vrednosti jednofotonskog razdešenja.

Zavisnost od temperature, ugla izmedju pumpe i probe i intenziteta pumpe je takodje istraživana. Povećanje temperature dovodi do povećanja koncetracije atoma kalijuma i shodno do povećanja unakrsno spregnutnih susceptibinosti odgovornih za ČTM sa jedne i do povećanja Doplerove širine i jednofotonske apsorpcije sa druge strane. Zbog ovih efekata veće pojačanje konjugovanog snopa na višim temperaturama nije opažen ali jeste izmereno najveće pojačanje za probni snop koje je iznosilo 63 na temperaturi od 150°C. Kao i u ostalim alkalnim parama mali ugao izmedju pumpe i probe je potreban za postizanje najboljeg faznog podudaranja. U slučaju kalijuma izmereni ugao iznosi 2 mrad. Konačno bili smo u mogućnosti da opazimo

ČTM pri niskim intenzitetima pumpe koje je moguće ostvariti korišćenjem konvencionalnih diodnih lasera čime se otvara mogućnost istraživanja ovavih fenomena sa jeftinijim i jednostavnijim tipovima lasera.

Zatim istraživani su optimalne vrednosti experimentalnih parametara koji bi dali najbilje rezultate usporavanja kratkih gausovskih svetlosnih impulsa u smislu frakcionog kašnjenja i frakcionog širenja. Najbolji postignut rezultat je 1.1 za frakciono kašnjenje uz vrednost frakcionog širenja od 1.2 za talasni impuls dužine $\tau = 120$ ns i $\delta = 2$ MHz, $\Delta = 1$ GHz, T = 120^oC, $I_{pump} = 200$ mW, $I_{ref} = 20\mu$W, $\Theta = 3$mrad gde je vrednost pojačanja probe iznosila 16. Dalja istraživanja su pokazala gotovo ravnu zavisnost od dvofotonskog razdešenja i intenziteta pumpe što je u kontrastu sa istraživanjima u natrijumu i rubidijumu.

Takodje ispitali smo nekoliko dužina trajanja Gausovskih svetlosnih impulsa. Sa smanjenjem vremeske dužine svetlosnog impulsa njegova širina u frekventnom domenu raste dovodeći do nejednakog usporavanja većeg broja Furijeovih komponenti i dodatnog širenja svetlosnog impulsa. U tom smislu, optimalna dužina svetlosnog impulsa sa frakcionim kašnjenjem većim od jedan (uslov potreban za primenu u optičkim linijama kašnjenja) i mimalnim širenjem je 120 ns.

Uporedjeni su i rezultati usporavanja u kalijumu sa rezultatima postignutim u natrijumu i rubidijumu i pokazano je da su rezultati u kalijumu bolji ili uporedljivi pri sličnim eksperimentalnim uslovima.

Ključne reči: Četvorotalasno mešanje, kalijum, spora svetlost

Naučna oblast: Fizika

Oblast istraživanja: Kvantna optika, Nelinearna optika

Content

1 Introduction

Nonlinear and quantum optics are two closely related and intertwined fields of physics. The field of study of quantum optics is the interaction of electromagnetic waves and matter. This interaction is described using the apparatus of quantum mechanics. Although the quantum nature of light was discovered a century ago thanks to the pioneering work of Max Planck, Albert Einstein, Arthur Compton and others, quantum optics is a relatively young scientific discipline which started developing in the second half of twentieth century. Today research in this field is very intensive both because of potential applications in different areas of industry on one side and fundamental insights into quantum mechanical nature of light and matter on the other.

The field of nonlinear optics studies phenomena which originate from the change of optical properties of the material caused by incident light. The *nonlinear* here stands for the situation in which the change of the optical properties of the medium scales nonlinearly with the strength of the incident light. For example in the pioneering work by Franken *et al* [1] it was shown that the second harmonic generation depends quadratically on the strength of the optical field. This work also showed that in situations where the wavelengths of the electromagnetic fields are close to the atomic scale of the underlying material medium (*i.e.* in the case of optical fields) very large field intensities are needed to achieve nonlinear effects. This fact illustrates the crucial role that *lasers* play in nonlinear optics. In fact the demonstration of the first working laser by Maiman *et al* [2] just one year before enabled the second harmonic generation by Franken. On the other side due to their coherent properties (among the other desirable qualities) lasers are used as almost the only light source in quantum optics as well. One could say that the birth of fields of quantum and nonlinear optics was made possible by the invention of lasers.

In the following decades researchers tried to lower the intensity threshold for mixing of the optical waves. Taking into account the coherence of laser light and crystal structure of solid state mediums through *phase matching* led to longer interaction lengths and hence higher efficiencies of the mixing processes [3]. On the other side optical mixing near atomic or molecular resonances, especially two-photon resonances have also been proved to enhance nonlinear effects [4]. Unfortunately nonlinear mixing in the vicinity of two-photon resonances was plagued with single-photon effects like single-photon absorption, phase shift, self-focusing and beam distortion. A way to mitigate this problem is to coherently excite superpositions of quantum states of the medium which results in change of its optical proprieties. Several examples demonstrate the power of coherent excitation: coherent population trapping ([5], [6]) and electromagnetically induced transparency ([7], [8], [9]), resonantly enhanced index of refraction ([10]), [11]), lasing without inversion ([12], [13], [14]). Experimental work presented in this thesis is based on the so called *double-*Λ *scheme*. Theoretical insights by Lukin, Hemmer, Scully and others have shown that it is possible to achieve very high nonlinear conversion efficiencies by exploiting coherent superposition in this type of systems without the unwanted single-photon effects ([15], [16]). The main nonlinear effect that occurs in this system is *four wave mixing* (FWM) in which four modes of electromagnetic field transfer energy among them ([17]). Lets take a look at the expression for polarization of the material medium given in the presence of an electric field:

$$\vec{P} = \epsilon_0(\chi^{(1)}\vec{E} + \chi^{(2)}\vec{E}^2 + \chi^{(3)}\vec{E}^3 + ...) \tag{1}$$

where $\chi^{1,2,3....}$ are orders of susceptibility tensor ([17]). In general higher order of susceptibility tensor are responsible for nonlinear effects. Material mediums in which nonlinear effects occur are called *nonlinear mediums* and are characterized by the existence of higher orders of susceptibility tensor. Most common nonlinear mediums are crystals and alkaline metal vapors. Alkaline metal vapors are centrosymmetric and isotropic mediums and hence have only odd orders of susceptibility tensor ([17]). First nonzero higher order is the third order of the susceptibility tensor χ^3 which is responsible for four wave mixing. Alkaline metal atomic structure is ideally suited for realization of double-Λ scheme. Usually two lower levels are the hyperfine sublevels of the atomic ground state. The quantum coherence between these two sublevels is responsible for high values of higher orders of susceptibility tensor which give rise to nonlinear effects ([15], [16]).

Numerous features of FWM as well as the effects based on it are of high scientific importance. Phenomena like optical phase conjugation, amplified reflection and oscillations ([18], [19]), reflection with conjugation and transmission of the EM field ([20], [20]) were studied both experimentally and theoretically. Many factors may influence the process of FWM. They range from intensities of laser beams ([21], [22], [23]) and EM field polarization ([24], [25]) to Zeeman coherences ([26]), atomic motion of the nonlinear medium ([27]) and dependency of beam intersection angle ([28]).

Experiments aimed at research of quantum optical and nonlinear effects in alkaline metals are usually realised in transparent glass cells which are filled atomic alkaline metal vapor. Coherent laser radiation with wavelength in narrow range around a specific atomic transition is traversing the cell and interacting with the atomic gas ensemble. Four wave mixing in alkaline metals, being a nonlinear effect, is also done this way. Very often the goal of FWM experiments is to get a very high efficiency of the FWM process (which is reflected in amplification of the conjugate beam). Experiments of this kind were performed in different metal vapors and in different experimental settings. In the so called counter-propagating geometry - a case where the pump and the probe beam propagate in the opposite directions - FWM efficiency was studied in sodium ([20]) , rubidium ([29]), potassium ([29]), cesium ([21]) and ytterbium ([30]). In the so called co-propagating geometry - a case where the pump and the probe beam propagate in the same direction - experiments were performed in sodium ([31]) , rubidium ([32]), cesium ([33]) and potassium ([34]).

Photons created in the FWM process show some very interesting quantum mechanical properties. Some of these properties are relative amplitude squeezing and quantum entanglement ([35], [36]). Relative intensity squeezing is a phenomena that stems from quantum correlations between photons generated in a nonlinear process. So if we have two separate beams that consist of mutually correlated photons we would consequently have two beams with correlated intensities. This results in noise reduction below the standard quantum limit (SQL) when measuring intensity difference between these beams. This effect has found its application in high-precision laser spectroscopy ([37]) and measurements below standard quantum limit ([38],

[39]). The nonlinear process of FWM also gives rise to quantum entanglement of generated photons ([40]) which makes FWM an important source of continuous entangled light ([41]). Entangled light is important from fundamental perspective since Bell inequalities can be violated only when the constituents of the quantum system are entangled ([42], [43]). In this sense the existence of entangled photons proves the non-local nature of quantum mechanics. On the other side entangled light has many potential applications. The promising field of quantum information is founded on entangled particles as a resource for algorithm optimization ([41]). The very important topic of secure communications is addressed by the field of quantum cryptography. Quantum cryptography also uses particle entanglement as a mean of creating absolutely secure information transportation channels ([44]).

For efficient optical communication and for all-optical signal processing in general, it is important to have control over optical impulses. This where the notion of *slow light* comes in. Slow light is phenomena where the group velocity of the photons is reduced ([17]). If we are able to control the amount of light slowing we would achieve the desired optical impulse control. Also the reduction of light speed is prerequisite for light stoppage and light storage which opens the possibility of direct storing of information coded into the optical signal, in other words optical memory ([45]). It was also shown that it is possible to manipulate with delay of quantum correlations and quantum entanglement using slow light giving more control over resources needed for quantum computing [46]. Other applications utilizing slow light are optical delay lines ([47], [48]), slow-light buffers ([48]), Phased Array Radar Beam Steering ([48]) and many others.

First dramatic reduction of light speed was achieved in ultra cold atomic gas by Hau and coworkers ([49]). After this success the field opened up to the various new ways of creating slow light. These techniques have one thing in common - they are all based on exploiting large dispersion which accompanies narrow transparency windows. In gaseous mediums slow light was generated using narrow EIT resonances ([50]) in both cold ([47], ([51]) and hot gases ([52], [53]). Double absorption resonances also proved able to generate slow light in gaseous media ([54]). Solid state mediums could also be used for slow light generation. Double dark states ([55]), spectral hole burning ([56]) coherent population oscillations ([57], [58]) and EIT ([59], [60]) have all been successfully used for slow light generation in solids. It is also interesting to try to achieve slow light directly in the medium that carries optical communications - namely in optical fibers. Successful slow light experiments in optical fibers encompass usage of Brillouin scattering ([61]) and stimulated Raman scattering ([62]).

As mentioned earlier slow light is needed for better control of optical communications but it is also important that we introduce minimum of signal distortion and attenuation in the process of light slowing. Unfortunately all of the techniques mentioned so far introduce signal attenuation through absorption. In order to tackle this problem researchers started studying light amplifying mediums ([61], [63], [64]). But light amplification comes with a price of introducing quantum noise in the signal which is an unwanted effect in quantum information applications ([65], [66]). Recently candidates to address both the problem of absorption and quantum noise introduction emerged in form of mediums suitable for double-Λ scheme implementation ([15], [16], [67], [68], [69]). Initial proposal by Lukin *et al* [16] suggested that it is possible to achieve two-photon resonance and have large nonlinearities associated with it while having no absorption through the effect of EIT. But experiments showed that EIT effect in hot alkaline gasses was plagued with effects like finite transit time of the atoms in the laser beams, Doppler broadening, and the existence of hyperfine sublevels out of the double-Λ that could also be excited. These all led to the decoherence between ground state sublevels that resulted in residual absorption and introduction of quantum noise. The quantum noise introduction manifested through low levels of squeezing in this type of scheme ([70]). In order to mitigate this unwanted effects researchers reduced the absorption by moving away from the resonance. The lower off-resonant nonlinear efficiencies were compensated with usage of high laser powers. These changes resulted in high levels of relative intensity squeezing, quantum correlations and entanglement ([32], [71], [72], [73], [40]). It was also shown that the spectral widths of FWM resonances obtained are narrow enough to produce substantial slowing of optical pulses ([69], [74], [75]).

Before the start of our work on potassium we've conducted a deep search through the literature and concluded that potassium hasn't been used in aforementioned co-propagating double-Λ off-resonant setting. Apart from that potassium is interesting because it has the smallest hyperfine splitting of the ground state among alkali metals (taking into account only stable isotopes) [76]. Theoretical model developed by Turnbull *et al* [77] suggest that smaller hyperfine splitting of the ground state produces higher gains of probe and conjugate beams in process of FWM. Higher gains lead to increasing the slowing of light pulses [74] and to higher amount of squeezing [78]. All of the above considerations have motivated us to start research of FWM and FWM related phenomena in hot potassium vapor. Concretely the aim of this thesis is two-fold:

- Observing non-degenerate FWM in hoot potassium vapor in co-propagating geometry
- Observing of slowed light pulses created in the FWM process in hot potassium vapor

We've chosen these aims because of numerous possible contributions. First, since FWM hasn't been observed in this setting, is to experimentally verify that this is possible. Consequently slowing of light pulses in these setting hasn't been done in potassium vapor so experimentally observing this effect would also be important. Besides the possible pioneering work in new nonlinear medium potassium is also interesting because of aforementioned low hyperfine splitting of its ground state. Low hyperfine splitting gives rise to high value of the third order of the susceptibility tensor $\chi^{(3)}$ [16]. High value of $\chi^{(3)}$ is the fundamental reason of high gains in the process of FWM shown by Turnbull in [77]. This fact is important for several reasons. Since the index of refraction of a medium is proportional to the real part of susceptibility of the medium [17] high values of $\chi^{(3)}$ would lead to big dispersion of the optical medium (in the narrow frequency window) and to large reducing of light speed [48]. The bigger the light speed reduction achieved the better it is for slow light applications that we've already discussed. Low hyperfine splitting of potassium ground state indicates the existence of high χ^3 and indicates that it is possible to achieve the biggest reduction of light speed among all alkali metals. High χ^3 also indicates that large gains in the process of FWM are possible which would lead to the bigger amounts of relative intensity squeezing and quantum entanglement between the probe and conjugate beam. This could improve the effects, techniques and applications based on squeezing and entanglement and would distinguish potassium vapor as one of the best sources of squeezed and entangled light. Regardless of the amount of relative intensity squeezing achieved in hot potassium vapor the methods based on this phenomena, as already mentioned high-precision spectroscopy and measurements below standard quantum limit, would find new application on new wavelengths - namely D1 and D2 lines of potassium (770nm and 766nm respectively for ^{39}K [76]).

In the end the this dissertation has the importance for the Quantum Optics Laboratory of the Photonics Centre at Institute of Physics in Belgrade. It presents the widening of the field of research of the Laboratory in the direction of nonlinear mediums, precision measurements and high power lasers.

2 Theoretical foundations of wave mixing

2.1 Wave equation in nonlinear media

Following considerations are based on [17]. Electromagnetic phenomena are described by Maxwell's equations:

$$\nabla \cdot \vec{D} = \rho \tag{2}$$

$$\nabla \cdot \vec{B} = 0 \tag{3}$$

$$\nabla \times \vec{E} = -\frac{\partial \vec{B}}{\partial t} \tag{4}$$

$$\nabla \times \vec{H} = -\frac{\partial \vec{D}}{\partial t} + \vec{J} \tag{5}$$

where $\vec{D}$ is vector of electric displacement, $\vec{B}$ is vector of magnetic induction, $\vec{E}$ is vector of electric field, $\vec{J}$ is vector of electric current and ρ is density of free electric charge.

We will assume that there are no free charges or currents so that

$$\rho = 0 \tag{6}$$

$$\vec{J} = 0 \tag{7}$$

and that the material is nonmagnetic so

$$\vec{B} = \mu_0 \vec{H} \tag{8}$$

The medium may be nonlinear which expressed through relation between electric displacement and magnetic induction:

$$\vec{D} = \epsilon_0 \vec{E} + \vec{P} \tag{9}$$

Using vector transformations and equations (4), (7) and (8) we arrive at general form of wave equation in nonlinear optics:

$$\nabla \times \nabla \times \vec{E} + \frac{1}{c^2}\frac{\partial^2}{\partial t^2}\vec{E} = -\frac{1}{\epsilon_0 c^2}\frac{\partial^2}{\partial t^2}\vec{P} \tag{10}$$

The first term on the left-hand side of equation (11) can be further transformed using the vector identity $\nabla \times \nabla \times \vec{E} = \nabla(\nabla \cdot \vec{E}) - \nabla^2 \vec{E}$. First term of the right hand side of equation (12) can usually be omitted. For example in the case of transverse, infinite plane waves $\nabla \cdot \vec{E}$ vanishes identically. In other cases, if the rotating wave approximation is valid, it can often be shown that this term is small. Based on this considerations we will assume that contribution from the $\nabla(\nabla \cdot \vec{E})$ is negligible. Now we can rewrite equation (11) in the following form:

$$\nabla^2 \vec{E} - \frac{1}{c^2}\frac{\partial^2}{\partial t^2}\vec{E} = \frac{1}{\epsilon_0 c^2}\frac{\partial^2}{\partial t^2}\vec{P} \tag{11}$$

or equivalently (using equation (8)):

$$\nabla^2 \vec{E} - \frac{1}{c^2}\frac{\partial^2}{\partial t^2}\vec{D} = 0 \tag{12}$$

Polarization $\vec{P}$ is usually split into linear and nonlinear part:

$$\vec{P} = \vec{P}^{(1)} + \vec{P}^{NL} \tag{13}$$

where linear part $\vec{P}^{(1)}$ depends linearly on electric field $\vec{E}$. Displacement field $\vec{D}$ can also be split into linear and nonlinear part

$$\vec{D} = \vec{D}^{(1)} + \vec{P}^{NL} \tag{14}$$

with linear part equal to:

$$\vec{D}^{(1)} = \epsilon_0 \vec{E} + \vec{P}^{(1)} \tag{15}$$

Now we can rewrite equation (13) in terms of linear part of displacement field $\vec{D}^{(1)}$:

$$\nabla^2 \vec{E} - \frac{1}{\epsilon_0 c^2}\frac{\partial^2}{\partial t^2}\vec{D}^{(1)} = \frac{1}{\epsilon_0 c^2}\frac{\partial^2}{\partial t^2}\vec{P}^{NL} \tag{16}$$

Now lets consider lossless and dispersionless medium. In this case linear part of displacement field $\vec{D}^1$ and electric field $\vec{E}$ are connected through dielectric tensor $\boldsymbol{\epsilon}^{(1)}$ which is real and frequency independent:

$$\vec{D}^{(1)} = \epsilon_0 \boldsymbol{\epsilon}^{(1)} \cdot \vec{E} \tag{17}$$

if in addition the given medium is isotropic equation (19) reduces to

$$\vec{D}^{(1)} = \epsilon_0 \epsilon^{(1)} \cdot \vec{E} \tag{18}$$

where $\epsilon^{(1)}$ is a scalar. So for lossless, dispersionless, isotropic medium the wave equation reads:

$$-\nabla^2\vec{E} + \frac{\epsilon^{(1)}}{c^2}\frac{\partial^2}{\partial t^2}\vec{E} = -\frac{1}{\epsilon_0 c^2}\frac{\partial^2}{\partial t^2}\vec{P}^{NL} \tag{19}$$

which is a inhomogeneous wave equation with $\vec{P}^{NL}$ as a source term. If the source term is absent free waves propagating with velocity c/n are a possible solution. Here n is the linear index of refraction where $n^2 = \epsilon^{(1)}$.

In the case of dispersive medium it is needed to examine every field frequency component independently. To do this we first express electric field $\vec{E}$, linear part of the displacement field $\vec{D}^{(1)}$ and nonlinear part of polarization $\vec{P}^{NL}$ as the sums of its frequency components:

$$\vec{E}(\vec{r},t) = \sum_n \vec{E}_n(\vec{r},t) \tag{20}$$

$$\vec{D^{(1)}}(\vec{r},t) = \sum_n \vec{D}_n^{(1)}(\vec{r},t) \tag{21}$$

$$\vec{P}^{NL}(\vec{r},t) = \sum_n \vec{P}_n^{NL}(\vec{r},t) \tag{22}$$

where the summation is over positive frequencies. Frequency components are represented as:

$$\vec{E}_n(\vec{r},t) = \mathcal{E}_n e^{-i\omega_n t} + c.c \tag{23}$$

$$\vec{D}_n^{(1)}(\vec{r},t) = \mathcal{D}_n^{(1)} e^{-i\omega_n t} + c.c \tag{24}$$

$$\vec{P}_n^{NL}(\vec{r},t) = \mathcal{P}_n^{NL} e^{-i\omega_n t} + c.c \tag{25}$$

where $\mathcal{E}_n$, $\mathcal{D}_n^{(1)}$ and $\mathcal{P}_n^{NL}$ are complex amplitudes of $\vec{E}_n$, $\vec{D}_n^{(1)}$ and $\vec{P}_n^{NL}$ respectively. In non-dissipative medium the dependence between $\vec{D}_n^{(1)}$ and $\vec{E}_n$ can be expressed as:

$$\vec{D}_n^{(1)}(\vec{r},t) = \epsilon_0 \boldsymbol{\epsilon}^1(\omega_n)\cdot\vec{E}_n(\vec{r},t) \tag{26}$$

where $\boldsymbol{\epsilon}^1(\omega_n)$ is real, frequency-dependent dielectric tensor. Rearranging equation (19) using relations (20 - 25) we obtain wave equation for the frequency component of the field in the non-dissipative medium:

$$\nabla^2\vec{E}_n - \frac{\epsilon^{(1)}(\omega_n)}{c^2}\frac{\partial^2}{\partial t^2}\vec{E}_n = \frac{1}{\epsilon_0 c^2}\frac{\partial^2}{\partial t^2}\vec{P}_n^{NL} \tag{27}$$

In the case of dissipative medium dielectric tensor becomes complex and relates complex fields amplitudes (defined in (23),(24) and (25)) in the following manner:

$$\mathcal{D}_n^{(1)}(\vec{r}) = \epsilon_0 \epsilon^{(1)}(\omega_n) \cdot \mathcal{E}_n(\vec{r}) \tag{28}$$

Using this relation along with equation (21), and relations (22), (23) and (24) we can rewrite equation (18) in the following form:

$$\nabla^2 \mathcal{E}_n(\vec{r}) + \frac{\omega_n^2}{c^2} \boldsymbol{\epsilon}^1(\omega_n) \cdot \mathcal{E}_n = -\frac{\omega_n^2}{\epsilon_0 c^2} \frac{\partial^2}{\partial t^2} \mathcal{P}_n^{NL} \tag{29}$$

This equation is the wave equation for the frequency components of the field in the general case of dissipative, nonlinear medium.

2.2 Calculation of Nonlinear Optical Susceptibilities - Density Matrix approach

Nonlinear optical susceptibilities are characteristic of a given medium. They depend on the underlying atomic and molecular structure of the medium. Quantum mechanical apparatus enables us to find functional relationships between nonlinear susceptibilities of a medium and its parameters such as dipole transition moments and atomic energy levels.

From quantum mechanical perspective the problem of calculating nonlinear susceptibilities could be addressed using two approaches:

- Schrödinger equation approach
- Density matrix approach

Although the Schrödinger equation approach is simpler, it can only be used in cases of nonresonant response of atomic or molecular systems ([17]). In other cases where excitations or relaxations of atoms have to be dealt with or where the collisional or time-of-flight broadening of the atomic resonances have to be accounted for density matrix approach gives much better results ([17], [79]) . Because of these reasons we will treat the problem of finding nonlinear susceptibilities of a given material by using density matrix approach. Following derivation is based on [79].

The problem of finding nonlinear optical susceptibilities will be treated semiclassically which means that given medium will be treated quantum mechanically and the electromagnetic field with whom the medium interacts will be treated classically. Let ψ be the wave function that describes our medium. The density matrix operator is defined as ensemble average of the ket and bra state vectors:

$$\rho = \overline{|\psi\rangle\langle\psi|} \tag{30}$$

The ensemble average of quantity A is:

$$\langle A\rangle = \overline{\langle\psi|A|\psi\rangle} = \mathrm{Tr}(\rho A) \tag{31}$$

Using Schrödinger equation and definition (30) we can derive equation of motion for density matrix operator ρ (Liouville equation):

$$\frac{\partial\rho}{\partial t} = \frac{1}{i\hbar}[H, \rho] \tag{32}$$

where H is the total Hamiltonian of the system. Hamiltonian is usually split into three parts, namely the unperturbed, interaction and random Hamiltonian:

$$H = H_0 + H_{int} + H_{random} \tag{33}$$

Hamiltonian H_0 describes the unperturbed system with eigenstates $|n\rangle$ and corresponding eigenenergies E_n, so $H_0|n\rangle = E_n|n\rangle$ holds. The interaction Hamiltonian H_{int} describes the interaction between the material system and electromagnetic field. In the dipole approximation [ref] this Hamiltonian is given by:

$$H_{int} = -e\vec{r}\cdot\vec{E} \tag{34}$$

where e is the electron charge ($e = 1.60217662 \times 10^{-19}C$), $\vec{r}$ is the position of the electron and $\vec{E}$ is the electromagnetic field. We should mention that here we are taking only the electronic contribution to nonlinear susceptibilities while the possible ionic contributions are left out. The random Hamiltonian H_{random} describes mechanisms of interaction of material system with thermal reservoir; in other words it describes relaxations of the system. Using decomposition (35) we can rewrite equation (34) as:

$$\frac{\partial\rho}{\partial t} = \frac{1}{i\hbar}[H + H_{int}, \rho] + \left(\frac{\partial\rho}{\partial t}\right)_{relax} \tag{35}$$

with:

$$\left(\frac{\partial\rho}{\partial t}\right)_{relax} = \frac{1}{i\hbar}[H_{random}, \rho] \tag{36}$$

We can represent the wave function of our material system ψ in the basis of eigenstates of unperturbed Hamiltonian H_0 as $\psi = \sum_n a_n|n\rangle$. Now it is possible to gain an insight into the physical meaning of the matrix elements of the density matrix operator. Diagonal matrix elements are calculated as:

$$\rho_{nn} = \langle n|\rho|n\rangle = \overline{|a_n|^2} \tag{37}$$

and they represent the population of the system in the state $|n\rangle$. Off-diagonal elements are calculated as:

$$\rho_{nm} = \langle n|\rho|m\rangle = \overline{a_n a_m^*} \tag{38}$$

These off-diagonal elements give information about the amount of coherent admixture of the states $|n\rangle$ and $|m\rangle$ present in the system. If the relative phase between states $|n\rangle$ and $|m\rangle$ fluctuates randomly the ensemble average will yield $\rho_{nm} = 0$. For example systems which are in thermal equilibrium will have $\rho_{nm} = 0$ for $n \neq m$.

In order to get a better understanding of $(\partial\rho/\partial t)_{relax}$ term we should take a deeper look to the relaxation processes. The population relaxation is a result of transitions between states induced by the interaction with the thermal reservoir. Let denote the thermally induced transition rate from state $|n\rangle$ to state $|m\rangle$ as $Q_{n\to m}$. We can then write the equation for the relaxation rate of the population of state $|n\rangle$ as:

$$\left(\frac{\partial\rho_{nn}}{\partial t}\right)_{relax} = \sum_m (Q_{m\to n}\rho_{mm} - Q_{n\to m}\rho_{nn}) \tag{39}$$

We can see that there are two contributions to the relaxation rate of the population of the state $|n\rangle$. One is positive and it represents the net contribution from relaxation channels of all the states $|m\rangle$ to the state $|n\rangle$. Other is negative and it represents the sum of all possible relaxation channels from the state $|n\rangle$ to other states $|m\rangle$. If the system is in the thermal equilibrium all populations have constant values so we have:

$$\frac{\partial\rho_{nm}^{(0)}}{\partial t} = \sum_m (Q_{m\to n}\rho_{mm}^{(0)} - Q_{n\to m}\rho_{nn}^{(0)}) = 0 \tag{40}$$

Combining equations (41) and (42) we get:

$$\frac{\partial}{\partial t}[(\rho_{nn})_{relax} - \rho_{nn}^{(0)}] = \sum_m (Q_{m\to n}(\rho_{mm} - \rho_{mm}^{(0)}) - Q_{n\to m}(\rho_{nn} - \rho_{nn}^{(0)})) \qquad (41)$$

Equations for relaxation of off-diagonal elements are more challenging to derive ([80]). Fortunately in most cases we can assume that the phase coherence between energy levels decays exponentially, so we can write (for $n \neq n'$):

$$\left(\frac{\partial \rho_{nn'}}{\partial t}\right)_{relax} = -\Gamma_{nn'}\rho_{nn'} \qquad (42)$$

The constant of proportionality $\Gamma_{nn'}$ is symmetric, $\Gamma_{nn'} = \Gamma_{n'n}$. Its inverse $\Gamma_{nn'}^{-1} = (T_2)_{nn'}$ is characteristic relaxation time between the states $|n\rangle$ and $|n'\rangle$ and is often referred to as transverse relaxation time. Population relaxation time is referred to as longitudinal relaxation time and it is denoted as $(T_1)_n$. Longitudinal relaxation time is often approximated by:

$$\frac{\partial}{\partial t}\left(\rho_{nn} - \rho_{nn}^{(0)}\right)_{relax} = -(T_1)_n^{-1}\left((\rho_{nn}) - \rho_{nn}^{(0)}\right) \qquad (43)$$

In order to solve the wave equation in particular medium it is needed to calculate the ensemble average of polarization $\vec{P}$ in that medium, i.e. it is necessary to solve:

$$\langle \vec{P} \rangle = \overline{\langle \psi | \vec{P} | \psi \rangle} = \mathrm{Tr}\,(\rho \vec{P}) \qquad (44)$$

In principle if unperturbed Hamiltonian H_0, interaction Hamiltonian H_{int} and $(\partial\rho/\partial t)_{relax}$ are known than equation of motion for density matrix operator (32) together with (44) completely describe the response of material medium to incoming field $\vec{E}$. The problem is that in general it is not possible to combine equations (32) and (44) into single equation of motion for $\langle \vec{P} \rangle$. Here we will only consider the steady-state response of the medium where $\langle \vec{P} \rangle$ is expandable into power series in $\vec{E}$ and use the perturbation theory in order to solve for $\vec{P}$.

First we denote the density matrix operator at thermal equilibrium as $\rho^{(0)}$. We also assume that there is no permanent polarization of the medium. Then we can write density matrix operator and polarization of the medium using perturbation expansion:

$$\rho = \rho^{(0)} + \rho^{(1)} + \rho^{(2)} + ... \qquad (45)$$

$$\langle \vec{P} \rangle = \langle \vec{P}^{(1)} \rangle + \langle \vec{P}^{(2)} \rangle + ... \qquad (46)$$

where

$$\langle \vec{P}^{(n)} \rangle = \mathrm{Tr}\,(\rho^{(n)} \vec{P}) \tag{47}$$

and

$$\langle \vec{P}^{(0)} \rangle = 0 \tag{48}$$

because of the aforementioned absence of permanent polarization of the medium. We will also regard interaction Hamiltonian H_{int} as the first-order perturbation. If we insert expansions (43) and (44) back to the equation (33) and group terms of the same order in H_{int} we will obtain:

$$\frac{\partial \rho^{(1)}}{\partial t} = \frac{1}{i\hbar}\left[\left[H_0, \rho^{(1)}\right] + \left[H_{int}, \rho^{(0)}\right]\right] + \left(\frac{\partial \rho^{(1)}}{\partial t}\right)_{relax} \tag{49}$$

$$\frac{\partial \rho^{(2)}}{\partial t} = \frac{1}{i\hbar}\left[\left[H_0, \rho^{(2)}\right] + \left[H_{int}, \rho^{(1)}\right]\right] + \left(\frac{\partial \rho^{(2)}}{\partial t}\right)_{relax} \tag{50}$$

and so on.

Here we are interested in how our material system responds to a field that can be represented as a sum of its spectral components i.e. to the field that can be represented as $\vec{E} = \sum_n \mathcal{E}_n e^{-i\omega_n t}$ (equations (20) and (23)). Since the interaction Hamiltonian is proportional to the applied electric field (equation (34)) we can also write it as a sum of its frequency components:

$$H_{int} = \sum_i \mathcal{H}_{int}(\omega_i) \tag{51}$$

where $\mathcal{H}_{int}(\omega_i) \sim \mathcal{E}_n e^{-i\omega_i t}$. The density matrix operator can now also be expanded into a sum of its frequency components:

$$\rho^{(n)} = \sum_j \rho^{(n)}(\omega_j) \tag{52}$$

And we will also have:

$$\frac{\partial \rho^{(n)}(\omega_j)}{\partial t} = -i\omega_j \rho^{(n)}(\omega_j) \tag{53}$$

Now we are able to solve equations (49) and (50) for the frequency components of the density matrix operator:

$$\rho^{(1)}_{nn'}(\omega_j) = \frac{(\mathcal{H}_{int}(\omega_j))_{nn'}}{\hbar(\omega_j - \omega_{nn'} + i\Gamma_{nn'})}\left(\rho^{(0)}_{n'n'} - \rho^{0}_{nn}\right) \tag{54}$$

$$\begin{aligned}\rho^{(2)}_{nn'}(\omega_j + \omega_k) &= \frac{\left[\mathcal{H}_{int}(\omega_j), \rho^{(1)}(\omega_k)\right]_{nn'} + \left[\mathcal{H}_{int}(\omega_k), \rho^{(2)}\omega_j\right]_{nn'}}{\hbar(\omega_j + \omega_k - \omega_{nn'} + i\Gamma_{nn'})} \\ &= \frac{1}{\hbar(\omega_j + \omega_k - \omega_{nn'} + i\Gamma_{nn'})}\times \\ \sum_{n''}((\mathcal{H}_{int}(\omega_j))_{nn''}\,&\rho^{(1)}_{n''n'}(\omega_k) - \rho^{(1)}_{nn''}(\omega_k)\,(\mathcal{H}_{int}(\omega_j))_{n''n'} + \\ (\mathcal{H}_{int}(\omega_k))_{nn''}\,&\rho^{(1)}_{n''n'}(\omega_j) - \rho^{(1)}_{nn''}(\omega_j)\,(\mathcal{H}_{int}(\omega_k))_{n''n'})\end{aligned} \tag{55}$$

Here we have used the shorthand notation $(\mathcal{H}(\omega_i)_{int'})_{nn'}$ for the matrix elements of the interaction Hamiltonian, $(\mathcal{H}(\omega_i)_{int'})_{nn'} = \langle n|\mathcal{H}(\omega_i)_{int'}|n'\rangle$.

Whenever diagonal elements $\rho^{(n)}_{mm}(0)$ appear in the derivation, further approximation on $(\partial\rho_{mm}/\partial t)_{relax}$ in (42) is often necessary to find a closed form solution. We also note that the expression for $\rho^{(2)}_{nn'}(\omega_j + \omega_k)$ in (55) is valid even for $n = n'$ as long as $\omega_j + \omega_k \neq 0$ since the term $(\partial\rho^{(2)}_{nn}/\partial t)_{relax}$ can then be neglected in the calculation.

Now we can derive full expressions for nonlinear polarizations $\langle\vec{P}^{(n)}\rangle$ and the nonlinear susceptibilities $\langle\chi^{(n)}\rangle$. Using (47) and (55) with $\mathcal{H}_{int} = -e\vec{r}\cdot\vec{E}$ and $\vec{P} = -Ne\vec{r}$ we derive first-order and second-order susceptibilities due to electronic contribution (expressions are given in Cartesian coordinates):

$$\chi^{(1)}_{ij}(\omega_p) = \frac{P^{(1)}_{ij}(\omega_p)}{E_j(\omega_p)} = \frac{N}{\epsilon_0\hbar}\sum_n\left[\frac{\mu^i_{an}\mu^j_{an}}{\omega_{na} - \omega_p - i\Gamma_{na}}\right] + \left[\frac{\mu^i_{an}\mu^j_{na}}{\omega_{an} + \omega_p + i\Gamma_{na}}\right] \tag{56}$$

$$\begin{aligned}\chi^{(2)}_{ijk}(\omega_p + \omega_q, \omega_q, \omega_p) &= \frac{N}{2\epsilon_0\hbar^2}\sum_{lmn}\rho^{(0)}_{ll} \\ \Bigg(\frac{\mu^i_{ln}\mu^j_{nm}\mu^k_{lm}}{[\omega_{nl} - \omega_p - \omega_q - i\Gamma_{nl}][\omega_{ml} - \omega_p - i\Gamma_{ml}]} &+ \frac{\mu^i_{ln}\mu^k_{nm}\mu^j_{lm}}{[\omega_{nl} - \omega_p - \omega_q - i\Gamma_{nl}][\omega_{ml} - \omega_q - i\Gamma_{ml}]} + \\ \frac{\mu^k_{ln}\mu^i_{nm}\mu^j_{lm}}{[\omega_{mn} - \omega_p - \omega_q - i\Gamma_{mn}][\omega_{nl} + \omega_p + i\Gamma_{nl}]} &+ \frac{\mu^j_{ln}\mu^i_{nm}\mu^k_{lm}}{[\omega_{mn} - \omega_p - \omega_q - i\Gamma_{nm}][\omega_{nl} + \omega_q + i\Gamma_{nl}]} + \\ \frac{\mu^j_{ln}\mu^i_{nm}\mu^k_{lm}}{[\omega_{nm} + \omega_p + \omega_q - i\Gamma_{nl}][\omega_{ml} - \omega_p - i\Gamma_{ml}]} &+ \frac{\mu^k_{ln}\mu^i_{nm}\mu^j_{lm}}{[\omega_{nm} + \omega_p + \omega_q + i\Gamma_{nm}][\omega_{ml} - \omega_p - i\Gamma_{ml}]} + \\ \frac{\mu^k_{ln}\mu^j_{nm}\mu^i_{lm}}{[\omega_{ml} + \omega_p + \omega_q + i\Gamma_{ml}][\omega_{nl} + \omega_p + i\Gamma_{nl}]} &+ \frac{\mu^j_{ln}\mu^k_{nm}\mu^i_{lm}}{[\omega_{ml} + \omega_p + \omega_q + i\Gamma_{ml}][\omega_{nl} + \omega_q + i\Gamma_{nl}]}\Bigg)\end{aligned} \tag{57}$$

Expression for third-order susceptibility has total of 48 terms. In order to write this expression in condensed manner we will make use of permutation operator $\mathcal{P}_I$. Meaning of this operator is that everything to the right of it is to be averaged over all possible permutations of the input frequencies ω_p, ω_q, and ω_r , with the Cartesian indices h, i, j permuted simultaneously. Next, we rewrite this equation as eight separate terms by changing the dummy indices so that l is always the index $\rho_{ii}^{(0)}$. We also require that only positive resonance frequencies appear if the energies are ordered so that $E_\nu > E_n > E_m > E_l$, and we arrange the matrix elements so that they appear in "natural" order, $l \to m \to n \to \nu$ (reading right to left):

$$\chi^{(3)}_{kjih}(\omega_p+\omega_q+\omega_r,\omega_r,\omega_q,\omega_p) = \frac{N}{\epsilon_0\hbar^3}\mathcal{P}_I\sum_{\nu n m l}\rho_{ll}^{(0)}$$

$$\begin{aligned}
&(\frac{\mu^k_{l\nu}\mu^j_{\nu n}\mu^i_{nm}\mu^h_{ml}}{[\omega_{\nu l}-\omega_p-\omega_q-\omega_r-i\Gamma_{\nu l}][\omega_{nl}-\omega_p-\omega_q-\Gamma_{nl}][\omega_{ml}-\omega_p-i\Gamma_{ml}]}+\\
&\frac{\mu^h_{l\nu}\mu^h_{\nu n}\mu^j_{nm}\mu^i_{ml}}{[\omega_{n\nu}-\omega_p-\omega_q-\omega_r-i\Gamma_{n\nu}][\omega_{m\nu}-\omega_p-\omega_q-\Gamma_{m\nu}][\omega_{\nu l}+\omega_p+i\Gamma_{\nu l}]}+\\
&\frac{\mu^i_{l\nu}\mu^k_{\nu n}\mu^j_{nm}\mu^h_{ml}}{[\omega_{n\nu}-\omega_p-\omega_q-\omega_r-i\Gamma_{n\nu}][\omega_{\nu m}+\omega_p+\omega_q+\Gamma_{nl}][\omega_{ml}-\omega_p-i\Gamma_{ml}]}+\\
&\frac{\mu^h_{l\nu}\mu^i_{\nu n}\mu^k_{nm}\mu^j_{ml}}{[\omega_{mn}-\omega_p-\omega_q-\omega_r-i\Gamma_{mn}][\omega_{nl}+\omega_p+\omega_q+\Gamma_{nl}][\omega_{\nu l}+\omega_p+i\Gamma_{\nu l}]}+\\
&\frac{\mu^j_{l\nu}\mu^k_{\nu n}\mu^i_{nm}\mu^h_{ml}}{[\omega_{\nu n}+\omega_p+\omega_q+\omega_r+i\Gamma_{mn}][\omega_{nl}-\omega_p-\omega_q-\Gamma_{nl}][\omega_{ml}-\omega_p+i\Gamma_{ml}]}+\\
&\frac{\mu^h_{l\nu}\mu^j_{\nu n}\mu^k_{nm}\mu^i_{ml}}{[\omega_{nm}+\omega_p+\omega_q+\omega_r+i\Gamma_{nm}][\omega_{m\nu}-\omega_p-\omega_q-\Gamma_{m\nu}][\omega_{\nu l}\omega_p+i\Gamma_{\nu l}]}+\\
&\frac{\mu^i_{l\nu}\mu^j_{\nu n}\mu^k_{nm}\mu^h_{ml}}{[\omega_{nm}+\omega_p+\omega_q+\omega_r+i\Gamma_{nm}][\omega_{m\nu}+\omega_p+\omega_q+\Gamma_{m\nu}][\omega_{ml}-\omega_p+i\Gamma_{ml}]}+\\
&\frac{\mu^h_{l\nu}\mu^i_{\nu n}\mu^j_{nm}\mu^k_{ml}}{[\omega_{ml}+\omega_p+\omega_q+\omega_r+i\Gamma_{ml}][\omega_{nl}+\omega_p+\omega_q+\Gamma_{nl}][\omega_{\nu l}+\omega_p+i\Gamma_{\nu l}]}).
\end{aligned} \tag{58}$$

2.3 Nonlinear interactions between modes of optical field - coupled wave equations

In the last section it was shown how specific (nonlinear) mediums give rise to nonlinear interactions. In this section it will be shown how different modes of optical field can be coupled through this type of interaction. In order to emphasize the basic concepts of the coupling between the modes of the optical field, the interaction between two modes, namely sum-frequency generation, will be shown first.

We consider second-order, lossless nonlinear optical medium and two collimated, monochromatic, continuous-wave input beams. Incident beams fall on nonlinear medium at normal incidence. The optical field in the medium is:

$$\vec{E}(t) = \vec{E}_1 e^{-i\omega_1 t} + \vec{E}_2 e^{-i\omega_2 t} + c.c. \tag{59}$$

From equation (1) we have:

$$\vec{P}^{(2)}(t) = \epsilon_0 \chi^{(2)} \vec{E}(t)^2 \tag{60}$$

Substituting equation (59) into (60) we get:

$$\begin{aligned}\vec{P}^{(2)}(t) = {} & \epsilon_0 \chi^{(2)} (\vec{E}_1^2 e^{-2i\omega_1 t} + \vec{E}_2^2 e^{-2i\omega_2 t} + 2\vec{E}_1\vec{E}_2 e^{-i(\omega_1+\omega_2)t} + 2\vec{E}_1\vec{E}_2^* e^{-i(\omega_1-\omega_2)t} + c.c.) \\ & +2\epsilon_0\chi^{(2)}(\vec{E}_1\vec{E}_1^* + \vec{E}_2\vec{E}_2^*)\end{aligned}$$

We can always represent polarization as a sum of its frequency components :

$$\vec{P}^{(2)} = \sum_n \mathcal{P}(\omega_n) e^{-i\omega_n t}$$

Then different frequency components of nonlinear polarization can be expressed as:

$$\mathcal{P}(2\omega_1) = \epsilon_0\chi^{(2)}\vec{E}_1^2 \qquad \text{(SHG)} \tag{61}$$

$$\mathcal{P}(2\omega_2) = \epsilon_0\chi^{(2)}\vec{E}_2^2 \qquad \text{(SHG)} \tag{62}$$

$$\mathcal{P}(\omega_1+\omega_2) = \epsilon_0\chi^{(2)}\vec{E}_1\vec{E}_2 \qquad \text{(SFG)} \tag{63}$$

$$\mathcal{P}(\omega_1-\omega_2) = \epsilon_0\chi^{(2)}\vec{E}_1\vec{E}_2^* \qquad \text{(DFG)} \tag{64}$$

$$\mathcal{P}(0) = \epsilon_0\chi^{(2)}(\vec{E}_1\vec{E}_1^* + \vec{E}_2\vec{E}_2^*) \qquad \text{(OR)} \tag{65}$$

All terms in the second order nonlinear polarization expression represent a distinct physical phenomena. These are as second-harmonic generation (SHG), sum-frequence generation (SFG), difference-frequency generation (DFG), and optical rectification (OR).

We will consider the case of sum-frequency generation more closely (figure 1). Sum-frequency generation is a process in which two fields with frequencies ω_1 and ω_2 mix giving rise to the new field at frequency $\omega_3 = \omega_1 + \omega_2$. The wave equation (29) holds for every frequency field component. Here we don't have a source term so in the case of plane wave with frequency ω_3 we have:

$$\vec{E}_3(z,t) = A_3 e^{i(k_3 - \omega_3 t)} + c.c. \tag{66}$$

where k_3 stands for:

$$k_3 = \frac{n_3 \omega_3}{c}, \qquad n_3^2 = \epsilon^{(1)}(\omega_3)$$

The amplitude of the wave A_3 is constant. In the case where nonlinear term is small the solution of wave equation for this case will still be in the form (66) except that A_3 will become a slowly varying function of z.

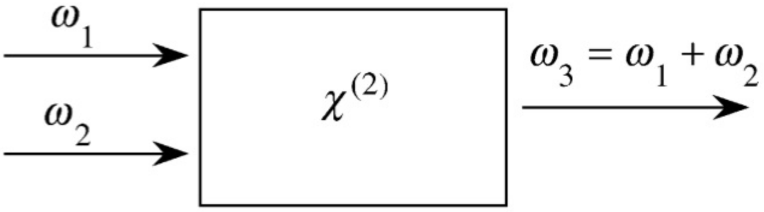

Figure 1: Sum-frequency generation - Two fields with frequencies ω_1 and ω_2 mix inside the $\chi^{(2)}$ nonlinear medium giving rise to the field with frequency ω_3. Picture taken from [17]

The polarization at frequency ω_3 is given by:

$$\vec{P}_3 = \mathcal{P}_3 e^{-i\omega_3} + c.c. \tag{67}$$

while from (63) we have:

$$\mathcal{P}_3 = \epsilon_0 \chi^{(2)} \vec{E}_1 \vec{E}_2$$

The input fields $\vec{E}_1$ and $\vec{E}_2$ are given in the following form:

$$\vec{E}_i(z,t) = A_i e^{-i(\omega_i t - k_i z)} + c.c \quad \text{where} \quad i = 1,2$$

We can then represent the amplitude of nonlinear polarization as:

$$\mathcal{P} = \epsilon_0 \chi^{(2)} A_1 A_2 e^{i(k_1+k_2)z} \equiv p_3 e^{i(k_1+k_2)z} \tag{68}$$

After some algebraic transformations and applying slowly varying envelope approximation we arrive at

$$\frac{dA_3}{dz} = \frac{i\chi^{(2)}\omega_3^{(2)}}{2k_3c^2}A_1A_2e^{i\Delta kz} \tag{69}$$

where:

$$\Delta k = k_1 + k_2 - k_3 \tag{70}$$

The newly introduced quantity Δk is called wavevector (or momentum) mismatch.

In similar manner we can derive equations for amplitudes A_1 and A_2 of the input fields with frequencies ω_1 and ω_2, respectively:

$$\frac{dA_1}{dz} = \frac{i\chi^{(2)}\omega_1^{(2)}}{2k_1c^2}A_3A_2^*e^{i\Delta kz} \tag{71}$$

$$\frac{dA_2}{dz} = \frac{i\chi^{(2)}\omega_2^{(2)}}{2k_2c^2}A_3A_1^*e^{i\Delta kz} \tag{72}$$

Equations (69), (70) and (71) are called coupled-amplitude equations. These equations demonstrate how the change of amplitude of output field on frequency ω_3 depends on amplitude of input fields on frequencies ω_1 and ω_2. Vice-versa change of amplitudes of input fields also depends on the amplitude of the other input field and the output field. In other words these fields are *coupled.* The coupling is made possible by the nonlinear polarization of the medium. The magnitude of the nonlinearity of the medium, expressed through coefficient χ, determines the strength of coupling between the fields.

If we examine coupled-amplitude equations more closely we would notice that apart from nonlinear susceptibility χ the strength of coupling between the mixing fields is also determined by the factor $e^{i\Delta kz}$. This factor introduces the influence of *phase matching*, which we discuss in the next section.

2.4 Phase matching

The concept of phase matching is of great importance for each type and order of wave mixing phenomena. Let's examine the the notion pf phase matching on sum-frequency generation example.

In the case of small energy transfer from mode of the field at frequency ω_1 and ω_2 to sum-frequency $\omega_3 = \omega_1 + \omega_2$ amplitudes A_1 and A_2 from equation (69) can be regarded as constants. If the condition :

$$\Delta k = 0 \tag{73}$$

is fulfilled, then the amplitude A_3 of the sum-frequency wave will rise linearly with z, and the field intensity will rise quadratically with z. The condition (73) is known as *perfect phase matching*. In cases when this condition holds, the newly generated wave with frequency $\omega_3 = \omega_1 + \omega_2$ extracts maximum energy from the incident waves at frequencies ω_1 and ω_2. This is possible because the generated wave and nonlinear polarization have constant phase difference which is favorable to this maximum energy transfer. Namely if we think of the nonlinear medium as consisting of microscopic atomic dipoles then perfect phase matching represents the situation in which these dipoles have perfect constant phase difference between them so the emitted field from each dipole coherently adds to the EM wave of frequency ω_3. Consequently the power of the field radiated scales with the number of atomic dipoles squared.

In situations when (73) isn't fulfilled the amount of mixing is smaller and consequently the intensity of output field is lower than in case of perfect phase matching. To get the amplitude of the output field in this case we integrate equation (73) from $z = 0$ to $z = L$, where L represents the length of the nonlinear medium in the z direction:

$$A_3(L) = \frac{i\chi^{(2)}\omega_3^2 A_1 A_2}{2k_3c^2} \int_0^L e^{i\Delta kz} dz = \frac{i\chi^{(2)}\omega_3^2 A_1 A_2}{2k_3c^2} \left(\frac{e^{i\Delta kL} - 1}{i\Delta k} \right) \tag{74}$$

If we average Poyniting vector over time we will get:

$$I_i = 2n_i\epsilon_0 c|A_i|^2 \qquad i = 1, 2, 3 \tag{75}$$

so for intensity of the output field we have:

$$I_3 = \frac{n_3\epsilon_0(\chi^{(2)})^2\omega_3^4|A_1|^2|A_2|^2}{8k_3^2c^3} \left| \frac{e^{i\Delta kL} - 1}{\Delta k} \right|^2 \tag{76}$$

After some transformations we arrive at the expression for the intensity of the output field I_3 :

$$I_3 = \frac{(\chi)^2\omega_3^2 I_1 I_2}{8n_1n_2n_3\epsilon_0c^2} L^2 \operatorname{sinc}^2 \left(\frac{\Delta kL}{2} \right) \tag{77}$$

We can see that the effect of phase matching on the intensity of the output field I_3 is included in the factor $\operatorname{sinc}^2(\Delta kL/2)$. This factor is known as *phase mismatch factor* (figure 2).

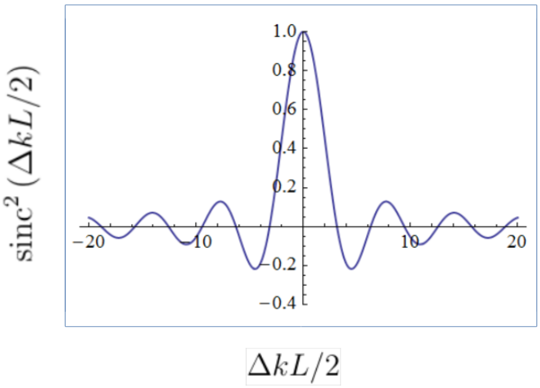

Figure 2: Phase mismatch factor - Influence of phase matching on the intensity of the output signal is given by $\operatorname{sinc}^2(\Delta kL/2)$

We observe that the efficiency of the wave mixing process generally decreases with $|\Delta k|\,L$ with some oscillations occurring. Oscillations can happen because the sum-frequency wave can go out of phase with nonlinear polarization of the medium which leads to energy transfer from sum-frequency wave back to incident waves of frequencies ω_1 and ω_2 (see equation (69)).

2.5 Four wave mixing and double Λ scheme

Usually magnitudes of nonlinear coefficients are very small ([17]), and hence the efficiencies on non-linear processes are small as well. Here we will examine a specific scheme, called the double Λ scheme, in which substantial enhancement of nonlinearity is possible (even without large initial coherence) ([16]). This scheme consist of four atomic levels which are coupled by four optical fields whose frequencies are tuned in the vicinity of these levels (figure 3). The transition between levels $|a\rangle$ and $|b\rangle$ is dipole-forbidden.

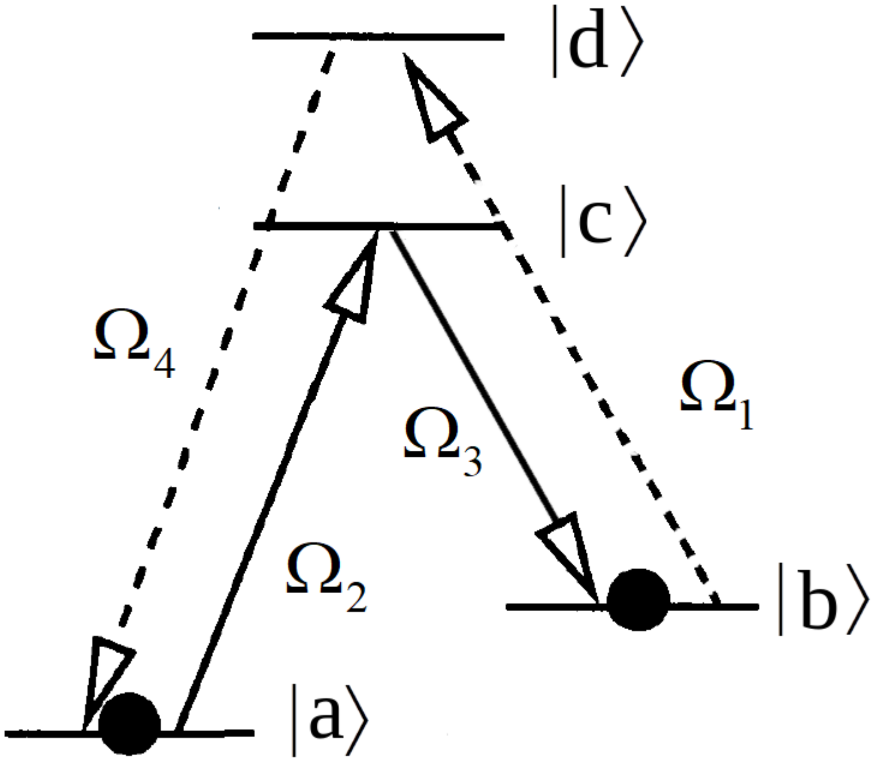

Figure 3: Λ scheme - Atomic levels are represented as $|a\rangle$, $|b\rangle$, $|c\rangle$ and $|d\rangle$ and optical fields coupling the atomic levels as Ω_1, Ω_2, Ω_3 and Ω_4

We will consider the case of two strong fields with frequencies ω_2 and ω_3 with respective Rabi frequencies Ω_2 and Ω_3 and two weak fields with frequencies ω_1 and ω_4 with respective Rabi frequencies Ω_1 and Ω_4. Essentially two strong fields interfere and create a running wave with wave vector $k = k_3 - k_2$. This running wave acts as a periodic grating from which a wave ω_1 can scatter and transfer energy to the wave at frequency ω_4. So strong fields ω_2 and ω_3 can be seen as mediators of the conversion from ω_1 to ω_4.

In our initial analysis we will make several assumptions. First all the fields examined are continuous waves. Second we assume that coherence on the dipole-forbidden transition $|a\rangle \rightarrow |b\rangle$ is long-lived. Third we assume that that both of the strong fields are perfectly tuned to the corresponding single-photon transitions (i.e. detuning is zero). Weak fields are detuned from their respective single-photon transitions by amount of Δ.

For describing this system we will use wave function approach. The wave function of the system can be written in the following form:

$$\Psi = a\,|a\rangle + b\,|b\rangle + c\,|c\rangle + d\,|d\rangle \tag{78}$$

where $|a\rangle$, $|b\rangle$, $|c\rangle$ and $|d\rangle$ are the atomic level eigenfunctions (figure 3). The Hamiltonian of this system is:

$$\begin{aligned} H = \hbar\omega_a\,|a\rangle\langle a| + \hbar\omega_b\,|b\rangle\langle b| + \hbar\omega_c\,|c\rangle\langle c| + \hbar\omega_d\,|d\rangle\langle d| \\ -\hbar(\Omega_1 cos(\nu_1 t)(|b\rangle\langle d|\,e^{i\phi_1} + |d\rangle\langle b|\,e^{-i\phi_1})) \\ -\hbar(\Omega_2 cos(\nu_2 t)(|a\rangle\langle c|\,e^{i\phi_2} + |c\rangle\langle a|\,e^{-i\phi_2}) \\ -\hbar(\Omega_3 cos(\nu_3 t)(|b\rangle\langle c|\,e^{i\phi_3} + |c\rangle\langle b|\,e^{-i\phi_3})) \\ -\hbar(\Omega_4 cos(\nu_4 t)(|a\rangle\langle d|\,e^{i\phi_4} + |d\rangle\langle a|\,e^{-i\phi_4})) \end{aligned} \tag{79}$$

where

$$\begin{aligned} \nu_1 &= \omega_d - \omega_b + \Delta \\ \nu_2 &= \omega_c - \omega_a \\ \nu_3 &= \omega_c - \omega_b \\ \nu_4 &= \omega_d - \omega_a + \Delta \end{aligned}$$

We see that Hamiltonian consists of two parts, first which gives the energies of atomic levels and second which describes the electromagnetic coupling between the atomic levels.

Now we can solve the Schrödinger equation (dot above symbol stands for time derivative):

$$|\dot{\Psi}\rangle = -\frac{i}{\hbar}\Psi H$$

substituting Ψ and H from (78) and (79) gives:

$$\begin{gathered}
\dot{a}\left|a\right\rangle + \dot{b}\left|b\right\rangle + \dot{c}\left|c\right\rangle + \dot{d}\left|d\right\rangle = \\
-\frac{i}{\hbar}\left[\left(\hbar\omega_a\left|a\right\rangle - \hbar\Omega_2 cos(\nu_2 t)e^{-i\phi_2}\left|c\right\rangle - \hbar\Omega_4 cos(\nu_4 t)e^{-i\phi_4}\left|d\right\rangle\right)\dot{a}\right] + \\
-\frac{i}{\hbar}\left[\left(\hbar\omega_b\left|b\right\rangle - \hbar\Omega_1 cos(\nu_1 t)e^{-i\phi_1}\left|d\right\rangle - \hbar\Omega_3 cos(\nu_3 t)e^{-i\phi_3}\left|c\right\rangle\right)\dot{b}\right] + \\
-\frac{i}{\hbar}\left[\left(\hbar\omega_c\left|d\right\rangle - \hbar\Omega_4^* cos(\nu_4 t)e^{i\phi_4}\left|a\right\rangle - \hbar\Omega_1^* cos(\nu_1 t)e^{i\phi_1}\left|b\right\rangle\right)\dot{d}\right] + \\
-\frac{i}{\hbar}\left[\left(\hbar\omega_c\left|c\right\rangle - \hbar\Omega_2^* cos(\nu_2 t)e^{i\phi_2}\left|a\right\rangle - \hbar\Omega_3^* cos(\nu_3 t)e^{i\phi_3}\left|b\right\rangle\right)\dot{c}\right]
\end{gathered} \tag{80}$$

After multiplying both sides of (80) with $\left\langle a\right|, \left\langle b\right|, \left\langle c\right|$ and $\left\langle d\right|$ from the left we get four following equations:

$$\begin{aligned}
\dot{a} =& - i\omega_a a + i\Omega_4^* cos(\nu_4 t)e^{i\phi_4} d + i\Omega_2^* cos(\nu_2 t)e^{i\phi_2} c \\
\dot{b} =& - i\omega_b b + i\Omega_1^* cos(\nu_1 t)e^{i\phi_1} d + i\Omega_3^* cos(\nu_3 t)e^{i\phi_3} c \\
\dot{c} =& - i\omega_c c + i\Omega_2 cos(\nu_2 t)e^{-i\phi_2} a + i\Omega_3 cos(\nu_3 t)e^{-i\phi_3} b - \gamma c \\
\dot{d} =& - i\omega_d d + i\Omega_4 cos(\nu_4 t)e^{-i\phi_4} a + i\Omega_1 cos(\nu_1 t)e^{-i\phi_1} b - \gamma d
\end{aligned}$$

In the above equations for excited levels $\left|c\right\rangle$ and $\left|d\right\rangle$ we've added phenomenologically the decay constant γ. If we make following substitutions:

$$\begin{aligned}
a =& a e^{-i\omega_a t} \\
b =& b e^{-i\omega_b t} \\
c =& c e^{-i\omega_c t} \\
d =& d e^{-i(\omega_d + \Delta)t}
\end{aligned}$$

We will get following set of equations for atomic levels:

$$\dot{a} = i\Omega_2^* d + i\Omega_4^* c \tag{81}$$

$$\dot{b} = i\Omega_3^* d + i\Omega_1^* c \tag{82}$$

$$\dot{c} = -\gamma c + i\Omega_2 a + i\Omega_3 b \tag{83}$$

$$\dot{d} = -(\gamma - i\Delta)d + i\Omega_4 a + i\Omega_1 b \tag{84}$$

In the case of equal values of the Rabi frequencies of driving fields , $|\Omega_2| \sim |\Omega_3| \sim \Omega\backslash\sqrt{2}$ the coherence between $|a\rangle$ and $|b\rangle$ is maximal. Solution of equation (80) in steady state is

$$d = i\frac{\Omega_4 a - \Omega_1 b}{\gamma - i\Delta} \tag{85}$$

We can also calculate the probability amplitudes of levels $|a\rangle$ and $|b\rangle$ in the case of maximal coherence. Also polarization of the levels coupled by the weak fields are proportional to the corresponding off-diagonal matrix elements ([17]). Putting these together gives us the expressions for the polarization of weak-field coupled levels:

$$\rho_{d,a} = da^* = \frac{i}{2(\gamma - i\Delta)}(\Omega_4 - \Omega_1\frac{\Omega_3^*\Omega_2}{\Omega^2}) \tag{86}$$

$$\rho_{d,b} = db^* = \frac{i}{2(\gamma - i\Delta)}(\Omega_1 - \Omega_4\frac{\Omega_3\Omega_2^*}{\Omega^2}) \tag{87}$$

Comparing the first and the second term in the expressions (86) and (87) we see that *linear and nonlinear part of the polarizations are of the same order.* This is stark contrast to the usual situations in which the nonlinear polarizations are smaller than linear by several orders of magnitude ([17]).

For the deeper analysis of coherently enhanced nonlinearities let's examine a slightly different scheme presented in figure 4.

Now two strong driving fields couple levels $|a\rangle \rightarrow |c\rangle$ with Rabi frequency Ω_2 and levels $|b\rangle \rightarrow |d\rangle$ with Rabi frequency Ω_1. These strong fields now convert to fields Ω_3 and Ω_4 which couple levels $|c\rangle \rightarrow |b\rangle$ and $|d\rangle \rightarrow |a\rangle$ respectively.

Our goal is to analyse the expressions for polarizations corresponding to the fields Ω_3 and Ω_4 which are being amplified in the process. We will assume that the populations of upper levels $|c\rangle$ and $|d\rangle$ in the double-Λ schemes are low (i.e.

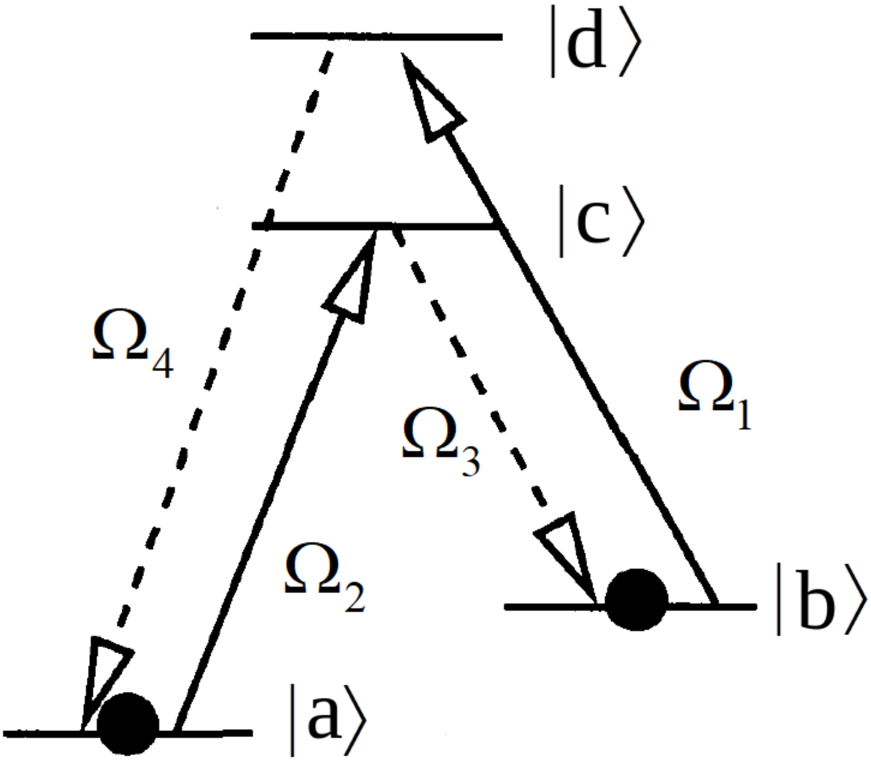

Figure 4: Λ scheme - Atomic levels are represented as $|a\rangle$, $|b\rangle$, $|c\rangle$ and $|d\rangle$ and optical fields coupling the atomic levels as Ω_1, Ω_2, Ω_3 and Ω_4

low saturation) and that transitions in the system are homogeneously broadened. Also for simplicity we consider the case of driving fields with equal strength ($|\Omega_1| = |\Omega_2| = |\Omega|$), infinitely long-lived coherency between ground state levels $|a\rangle$ and $|b\rangle$ ($\gamma_c \to 0$) and equal detuning for $|a\rangle \to |c\rangle$ and $|b\rangle \to |d\rangle$ one-photon transitions Δ.

We examine the steady-state density matrix of the system. If we want to have cross coupling via nonlinearity and energy flow from one optical mode to another we need to satisfy the energy conservation law e.g. we need to have:

$$\omega_1 + \omega_2 = \omega_3 + \omega_4 \tag{88}$$

After solving the equations of motion for populations and coherences for this system (assuming weak Ω_1 and Ω_4) ([16], [77]) we arrive at the following expression for polarizations on the $|c\rangle \to |b\rangle$ and $|d\rangle \to |a\rangle$ transitions:

$$P_1 = \epsilon_0 \chi_{11} E_1 + \epsilon_0 \chi_{14} e^{i\delta\vec{k}\vec{r}E_4^*} \tag{89}$$

$$P_4 = \epsilon_0 \chi_{44} E_4 + \epsilon_0 \chi_{41} e^{i\delta\vec{k}\vec{r}E_1^*} \tag{90}$$

where E_1 and E_4 are the electric fields corresponding to the Rabi frequencies Ω_1 and Ω_4 and $\vec{\delta k} = \vec{k}_1 + \vec{k}_2 - \vec{k}_3 - \vec{k}_4$ (k_i are wave vectors of the fields) is so called *geometric phase mismatch.* Here χ_{ii} are linear susceptibilities and χ_{ij} are χ^3 type, FWM susceptibilities. These susceptibilities have the following form ([16]):

$$\chi_{11}^* = i\frac{N\rho_1^2}{\epsilon_0\hbar}\frac{\Gamma_{bd}}{D}[A\frac{\Gamma_{cd}}{\Gamma_{cb}} - B(\frac{\Gamma_{ab}\Gamma_{cd}}{\Omega^2} + \frac{\Gamma_{cd}+\Gamma_{ab}}{\Gamma_{bd}} - \frac{\Gamma_{ab}}{\Gamma_{ca}})] \tag{91}$$

$$\chi_{14}^* = i\frac{N\rho_4\rho_1}{\epsilon_0\hbar}\frac{\Omega_1^*\Omega_4^*}{|\Omega|^2}\frac{\Gamma_{cb}}{D}[A(\frac{\Gamma_{ab}}{\Gamma_{bd}} + \frac{\Gamma_{cd}+\Gamma_{ab}}{\Gamma_{cb}}) + B\frac{\Gamma_{cd}}{\Gamma_{ac}}] \tag{92}$$

$$\chi_{41} = \frac{N\rho_4\rho_1}{i\epsilon_0\hbar}\frac{\Omega_1\Omega_4}{|\Omega|^2}\frac{\Gamma_{ad}}{D}[B(\frac{\Gamma_{cd}+\Gamma_{ab}}{\Gamma_{ad}} + \frac{\Gamma_{ab}}{\Gamma_{ca}}) + A\frac{\Gamma_{cd}}{\Gamma_{db}}] \tag{93}$$

$$\chi_{44} = \frac{N\rho_1^2}{i\epsilon_0\hbar}\frac{\Gamma_{ad}}{D}[B\frac{\Gamma_{cd}}{\Gamma_{ac}} - A(\frac{\Gamma_{ab}\Gamma_{cd}}{\Omega^2} + \frac{\Gamma_{cd}+\Gamma_{ab}}{\Gamma_{ad}} - \frac{\Gamma_{ab}}{\Gamma_{bd}})] \tag{94}$$

where $\Gamma_{ij} = \gamma_{ij} - i\Delta$ are complex relaxation rates between respective levels, and D is defined as:

$$D = (\Gamma_{cb} + \Gamma_{ad})(\Gamma_{cd} + \Gamma_{ab}) + \frac{\Gamma_{ad}\Gamma_{cb}\Gamma_{ab}\Gamma_{cd}}{|\Omega|^2}$$

If we assume large one-photon detuning ie $|\Delta| \gg \gamma_i, |\Gamma_{da}|, |\Gamma_{db}|$ most of the atoms remain in the state $|a\rangle$ (and hence we have $A \approx 0, B \approx 1$). In this approximation equation for susceptibilities (91 - 94) reduce to:

$$\chi_{11}^* \approx i\frac{N\rho_1^2}{\epsilon_0\hbar}\frac{\Gamma_{ab} + i|\Omega|^2/\Delta}{|\Omega|^2 + \Gamma_{ad}\Gamma_{ab}} \tag{95}$$

$$\chi_{14}^* \approx \frac{N\rho_4\rho_1}{\epsilon_0\hbar}\frac{\Omega_1^*\Omega_4^*}{\Delta}\frac{1}{|\Omega|^2 + \Gamma_{ad}\Gamma_{ab}} \tag{96}$$

$$\chi_{41} \approx \frac{N\rho_4\rho_1}{\epsilon_0\hbar}\frac{\Omega_1\Omega_2}{\Delta}\frac{1}{|\Omega|^2 + \Gamma_{ad}\Gamma_{ab}} \tag{97}$$

$$\chi_{44} \approx 0 \tag{98}$$

If we take a closer look to equation (95) we can see that the medium is no longer transparent even if the two-photon detuning is at resonance and the ground-state relaxation is zero ($\Gamma_{ab} \to 0$). At this point we see that the linear susceptibility is always larger than the corresponding nonlinear susceptibility. However, we can regain the transparency by setting the two-photon detuning to

$$\delta = \delta_0 \equiv |\Omega|^2/\Delta \tag{99}$$

which is needed to compensate the AC-Stark light shift. This small two-photon detuning does not affect the cross-coupling nonlinearity as long as $|\Delta| \gg |\Gamma_{da}|$ ie as long as our approximation is valid. So now if we compensate for the AC-Stark shift by a small two-photon detuning we would again have the favourable situation where nonlinear cross-couplings exceed the linear susceptibility if we have $|\Omega|^2 > |\Delta|\gamma_{ab}$. Consequently if these conditions are met we could have very efficient energy transfer between strong and weak fields in our double-Λ scheme. From the equations (96) and (97) we see that cross susceptibilities χ_{14} and χ_{41} scale inversely with the detuning of the field E_4 so it is desirable to have it as small as possible. On the other side this analysis breaks down when optical pumping out of the state $|a\rangle$ becomes significant. This happens when $\gamma_{ca}\Omega^2 \sim \gamma_{ab}|\Delta|^2$. In our approximation all fields have the same detuning Δ so both fields E_1 and E_2 have similar optical pumping rates which results in evenly distributed population between lower, metastable, levels $|a\rangle$ and $|b\rangle$. It is shown ([16]) that in this case linear part of susceptibilities vanish at the point of two-photon resonance and nonlinearities become resonantly large:

$$\chi_{14} \;=\; \chi_{41} \;=-i\frac{\rho_1\rho_4}{\hbar\epsilon_0}\frac{N\Omega_1\Omega_4 2\gamma_0(\rho_{uu}-\rho_{ll})}{\Gamma_0(|\Gamma_0|^2\gamma_{ab}+2|\Omega|^2\gamma_0)} \tag{100}$$

($\rho_{uu} - \rho_{ll}$ is population difference between upper and lower level). This expression resembles the familiar expression for the linear susceptibility of a two-level system. In other words the nonlinear polarization excited under these conditions is of the same order as the "bare" resonant polarization. This point is graphically expressed in Figure 5.

From figure 5 we see that there is a *large dispersion of the refractive index* around the resonance which is important in two ways:

1.) It can be used to eliminate any residual phase mismatch that may arise (for example in the non-perfect colinear propagation of optical fields) by small two-photon detuning.

2.) Large dispersion of index of refraction gives rise to the *small light group velocity*

Now that we have calculated the susceptibilities we can use them to get the equations for the electric fields. We will consider the case of co-propagating strong driving (or "pump") fields E_2 and E_3 together with a signal wave E_1. Field E_4 is generated in a four-wave mixing process. We will also neglect the effects of depletion and absorption of the driving fields and treats the signal and generated fields only to the

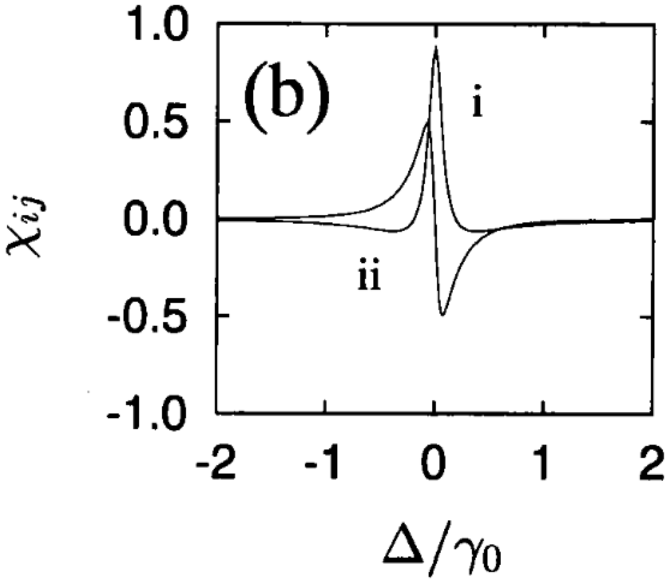

Figure 5: Susceptibility spectrum for the resonantly driven closed system of Fig. 6. (i) $-Im(\chi_{ij})$ (ii) $Re(\chi_{ij})$

first order. Using Maxwell's equation for signal and generated field we get:

$$(\frac{1}{c}\frac{\partial}{\partial t} + \frac{\partial}{\partial z})E_{1,4} = i\frac{k_{1,4}}{2\epsilon_0}P_{1,4} \tag{101}$$

If we substitute the values for $P_{1,2}$ from equations (89) and (90) we get ([16], [77]):

$$(\frac{1}{c}\frac{\partial}{\partial t} + \frac{\partial}{\partial z})E_1 = \frac{i}{2}k_1\chi_{11}E_1 + \frac{i}{2}k_1\chi_{14}e^{i\delta\vec{k}\vec{r}}E_4^* \tag{102}$$

$$(\frac{1}{c}\frac{\partial}{\partial t} + \frac{\partial}{\partial z})E_4 = \frac{i}{2}k_2\chi_{44}E_4 + \frac{i}{2}k_4\chi_{41}e^{i\delta\vec{k}\vec{r}}E_1^* \tag{103}$$

We've assumed that $E_1(0) = E^0$ and $E_4(0) = 0$ so the solution to the above system is:

$$E_1(L) = E^0e^{\delta aL}[\cosh(\xi L)\frac{a}{\xi}\sinh(\xi L)] \tag{104}$$

$$E_4(L)^* = E^0e^{\delta aL}[\frac{a_{41}}{\xi}\sinh(\xi L)] \tag{105}$$

Where $a_{1j} = ik_1\chi_{1j}/2, a_{4j} = ik_4\chi_{4j}^*/2, \delta a = (a_{11} - a_{44} + i\Delta k_z)/2, a = (a_{11} + a_{44} + i\Delta k_z)/2$ and $\xi = \sqrt{-a_{14}a_{41} + a^2}$. In these expressions we also have Δk_z which is the z-component of the total phase mismatch $\Delta\vec{k}$, z being the axis of propagation of the driving fields.

The important thing to note is that if we satisfy the phase matching condition i ($Re(a) = 0$) by small two-photon detuning, and non-linear term exceeds linear

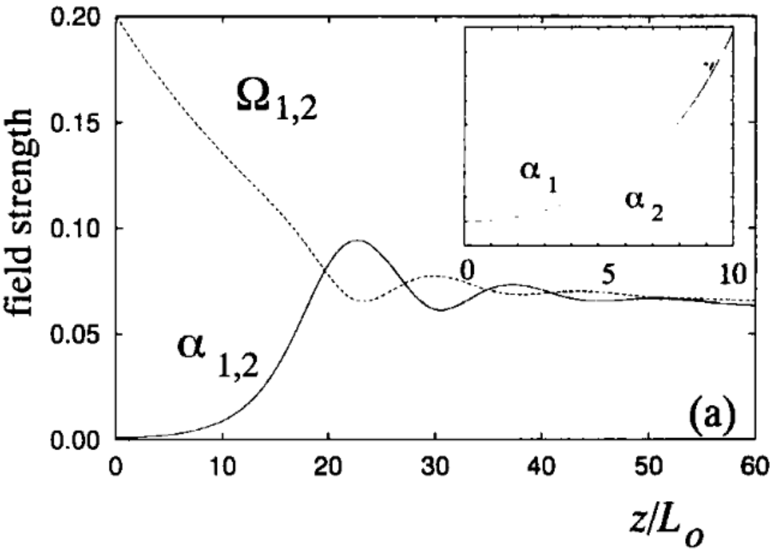

Figure 6: Intensity of the signal and newly generated fields (solid) and the driving fields (dashed) as a function of propagation distance

absorption, the fields E_1 and E_4 will grow exponentially with coefficient proportional to $|k_i|\chi_{ij}$ (Figure 5).

From figure 6 we see that the energy is being transferred from pump fields to newly generated fields. After initial exponential energy transfer the system becomes saturated and fields propagate in free-space like manner.

2.6 Slow light

In mediums with large dispersion an interesting phenomena is observed: short light pulses propagate through the mediums with speed several orders of magnitude smaller than in vacuum. This phenomena is known slowing of light pulses or slow light ([47]).

In order to better understand the phenomena of slow light let us define *phase velocity* v_f and *group velocity* v_g of electromagnetic wave. Phase velocity is the velocity at which the phase of any frequency component of the electromagnetic wave travels. On the other hand group velocity is the velocity at which the envelope of the electromagnetic wave's amplitude propagates. In general, in material medium, we can control the group velocity of wave package defined by the time shape of its amplitude. In this sense slow light refers to the phenomena when we are able to reduce the group velocity significantly ie when we have $v_g \ll v_p$.

Experimentally, the effect is observed when a short laser pulse is divided with a beam splitter and one beam is directed to a medium with high dispersion and other beam propagates the same distance through air. Both pulses are detected with identical photodiodes. In general two effects are observed:

1.) The beam that propagates through dispersive medium is delayed - slow light

2.) The beam that propagates through dispersive medium is distorted (broadened)

Why do these effects occur? Let τ be the time-width of the light pulse and let ω be its center angular frequency. According to Heisenberg uncertainty relations the light pulse has energy uncertainty ΔE and, since $E = \hbar\omega$, frequency width $\Delta\omega$. Again using Heisenberg uncertainty relations we conclude that frequency width $\Delta\omega$ must be larger or equal to inverse time-width of the light pulse:

$$\Delta E\tau \geq \hbar \;\Rightarrow\; \hbar\Delta\omega\tau \geq \hbar \;\Rightarrow\; \Delta\omega \geq \frac{1}{\tau} \tag{106}$$

In other words light pulse is comprised of Fourier components which have frequencies

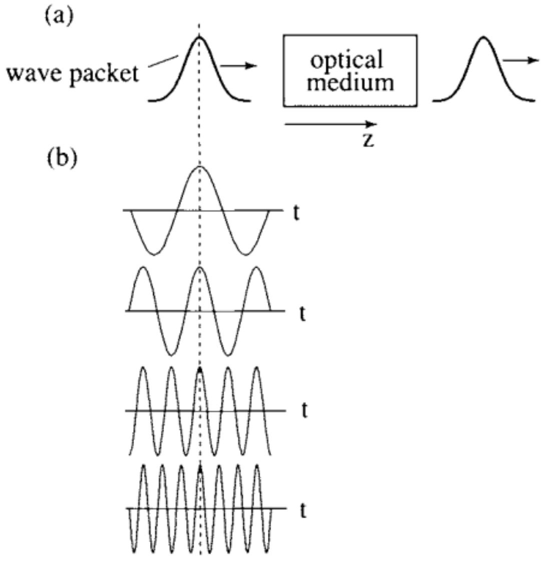

Figure 7: Intensity of the signal and newly generated fields (solid) and the driving fields (dashed) as a function of propagation distance

in interval $\omega \pm \Delta\omega$ (figure 7). Phase of the monochromatic plane wave $E(z,t) =$

$Ae^{i(kz-\omega t)} + c.c.$ propagating through a medium with refractive index n is given by:

$$\phi = kz - \omega t \tag{107}$$

where $k = \frac{n\omega}{c}$. If we want to have pulse propagation without distortion Fourier components must add in phase for all values of the propagation distance z. So if we write the phase as $\phi = \frac{n\omega z}{c} - \omega t$ and require that there be no change in ϕ to the first order in ω we arrive at the condition:

$$\frac{d\phi}{d\omega} = 0 \tag{108}$$

Substituting ϕ from eq (107) we get:

$$\frac{dn}{d\omega}\frac{\omega z}{c} + \frac{nz}{c} - t = 0 \tag{109}$$

We can express group velocity as change of the z coordinate in time, ie $v_{gr} = z/t$ so we get:

$$v_{gr} = \frac{c}{n + \omega\frac{dn}{d\omega}} = \frac{c}{n_{gr}} \tag{110}$$

where $n_{gr} = n + \omega\frac{dn}{d\omega}$ is the *group index of refraction.* In cases where the dispersion of index of refraction is positive ($\frac{dn}{d\omega} > 0$) we have so called *normal dispersion* of index of refraction. From (110) we see that normal dispersion of index of refraction leads to group velocity being smaller that phase velocity, $v_{gr} < v_{ph}$. It is also clear that larger dispersion (larger $\frac{dn}{d\omega}$) leads to greater reduction of group velocity v_{gr}. If we take a look at equation (100) and figure 5 we can see that steep change of index of refraction is generated by the four wave mixing resonances. Moreover, narrower resonances lead to larger reduction of group velocity.

On the other side from equation (110) we see that every Fourier component of the wave package has its own velocity defined by its angular frequency. In case of very dispersive mediums this will lead to pulse widening or even pulse distortion. If we expand the propagation constant $k(\omega)$ in power series around the light pulse's central frequency ω_0 we get ([47]):

$$k(\omega) = k_0 + k_1(\omega - \omega_0) + \frac{1}{2}k_2(\omega - \omega_0)^2 + ... \tag{111}$$

Here k_0 is the mean wavevector magnitude of the optical pulse, first derivative with respect to frequency, k_1, is the inverse of the group velocity

$$k_1 = \frac{dk}{d\omega}\bigg|_{\omega=\omega_0} = \frac{1}{v_{gr}} = \frac{n_{gr}}{c} \tag{112}$$

and second derivative with respect to frequency, k_2, is the dispersion in the group velocity:

$$k_2 = \frac{d^2k}{d\omega^2}\bigg|_{\omega=\omega_0} = \frac{d(1/v_{gr})}{d\omega} = \frac{1}{c}\frac{dn_{gr}}{d\omega} \tag{113}$$

If the length of the dispersive medium is L then transit time of the light pulse through the medium is given by:

$$T = \frac{L}{v_{gr}} = Lk_1 \tag{114}$$

and the spread of transit times is given approximately by:

$$\Delta T = Lk_2\Delta\omega \tag{115}$$

where the frequency bandwidth of the pulse is given by $\Delta\omega_0$. From these expressions we can identify the two main factors that influence light pulse broadening:

1.) Spectral width of the light pulse $\Delta\omega$

2.) Propagation distance through the dispersive medium L

It becomes clear that if we want to bring pulse broadening to the minimum we should use spectrally narrow light pulses (which imply that we should use broad pulses in time) and short dispersive mediums. On the other hand these constraints are not desirable since shorter light pulses are more favorable for information transfer (if we think about optical pulse train ref [?]) and shorter propagation distances through dispersive mediums mean smaller light reductions. The aim of this thesis is two find optimal trade off between these factors for the light pulses in hot potassium vapor.

2.7 Pockels effect

For creation of short light pulses we'll be using devices capable of modificating light phase and polarization - polarizers, wave-plates, phase retarders etc. These devices are usually made of birifingent anisotropic materials ([81]). Polarization of electromagnetic wave is described by the Johnson vector and the change of polarization introduced by the optical system is described by Johnson matrix ([81]):

$$\begin{pmatrix} A_{2x} \\ A_{2y} \end{pmatrix} = \begin{pmatrix} T_{11} & T_{12} \\ T_{21} & T_{22} \end{pmatrix} \begin{pmatrix} A_{1x} \\ A_{1y} \end{pmatrix} \tag{116}$$

or in condensed form:

$$\vec{J_2} = T\vec{J_2} \tag{117}$$

where $\vec{J_1}$ and $\vec{J_2}$ are the Johnson vectors of incident and transmitted waves respectively and T is the Johnson matrix that describes the optical system.

Lets take a closer look at phase retarders. These devices are used for changing the state of polarization of electromagnetic waves. Phase retarders are usually made of birifringent anisotropic plates and are characterized by phase delay Γ and index of refraction of ordinary (n_o) and extraordinary (n_e) axis. These crystals are usually cut in a way that light propagates along the z-axis(z-cut crystals) and ordinary and extraordinary axes are orthogonal to the direction of propagation. Along these main axes of the crystal normal modes of the electromagnetic wave travel with different speeds c/n_x and c/n_y. If $n_x < n_y$ than x axis is called the "fast" axis. So for the plate of length d we have a phase delay of:

$$\Gamma = (n_x - n_y)k_0 d = 2\pi(n_x - n_y)d/\lambda_0 \tag{118}$$

Johnson matrix of this system can be written as:

$$\begin{pmatrix} 1 & 0 \\ 0 & e^{-i\Gamma} \end{pmatrix} \tag{119}$$

For example if $\Gamma = \pi$ we would get the $\lambda/2$ wave-plate and for $\Gamma = \pi/2$ we get $\lambda/4$ wave-plate.

Some materials change their refractive index in electric field. This effect belongs to the broader group of electro-optic effects ([81]). If those materials are birifringent anisotropic crystals they be used as phase retarders with controllable phase delay. If the change of refraction index is proportional to the applied field then we have the Pockels effect and if the dependence if quadratic we have Kerr effect ([81]). Usual materials used as linear electro-optic mediums are NH_4, H_2PO_4, KH_2PO_4, $LiNbO_3$,

$LiTaO_3$, CdTe .

Lithium niobate ($LiNbO_4$) is one of the materials that have the exhibit the largest Pockels effect. Equations that describe the change of refractive index along x and y axes in applied electrical field $\vec{E}$ are:

$$n_x = n_e(1 - \frac{1}{2}n_e^2 r_{33} E) \tag{120}$$

$$n_y = n_0(1 - \frac{1}{2}n_0^2 r_{13} E) \tag{121}$$

$$\Delta n = n_x - n_y = const + \frac{1}{2}(n_e^3 r_{33} - n_0^3 r_{13})E \tag{122}$$

where n_e and n_o are extraordinary and ordinary index of refraction respectively, and r_{13} and r_{33} are elements of the electro-optic tensor of $LiNbO_3$ ([81]).

2.8 Electro-optic modulator

Electro-optic modulator is a device which uses the electro-optic effect to modulate a light beam passing through it. In most cases Pockels cells are used as electro-optic modulators.

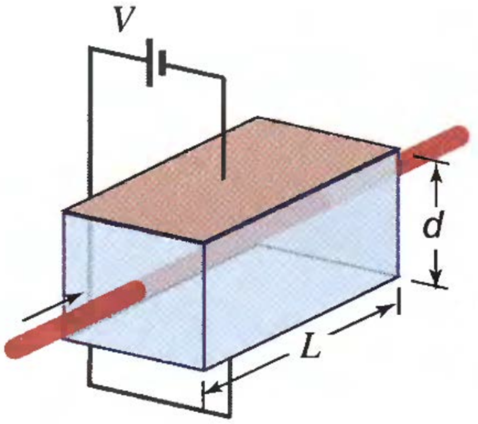

Figure 8: Transversal electro-optic modulator. L - length of the crystal, d - thickness of the crystal, V - applied voltage to the sides of the crystal. The arrow shows the direction of light propagation through the crystal

When an EM wave with wavelength λ_0 passes through a Pockels cell (figure 8) of length L which has voltage V applied to its sides then the phase shift of the EM wave is:

$$\phi = k_0 \Delta n L = 2\pi \Delta n L/\lambda_0 \tag{123}$$

where $k_0 = \omega/c = 2\pi/\lambda_0$ and Δn is the change of index of refraction due to Pockels effect (122). If we denote the crystal thickness as d then electric field inside the crystal is $E = V/d$ and equation (123) gets the following form:

$$\phi = \phi_0 - \pi \frac{V}{V_\pi} \tag{124}$$

where ϕ_0 is the phase shift in absence of electric field and V_π is the voltage that should be applied in order to get a phase shift of π . Then we have that:

$$V_\pi = \frac{d}{L} \frac{\lambda_0}{\tau n^3} \tag{125}$$

where τ is the electro-optic coefficient of the material. Equation (125) expresses the linear dependence between the phase shift and applied voltage. It also shows that it is possible to perform the phase modulation of the EM wave by changing the voltage applied on the crystal.

Phase modulator put in one branch of the optical interferometer can function as a intensity modulator. Lets consider the Mach-Zender interferometer with modulator in one of its branches (fig 8)

If we operate with 50:50 beam splitter and combiner then we have the following relation between the input and the output intensity I_i and I_o:

$$I_o = \frac{1}{2} I_i + \frac{1}{2} I_i \cos\phi = I_i \cos^2(\phi/2) \tag{126}$$

where $\phi = \phi_1 - \phi_2$ is the difference in phase shift accumulated during light propagation through branches 1 and 2 of the interferometer. The essential part of the interferometer is the beam combiner B where light beam from two branches interfere. Since there is a phase modulator in branch 2 the total phase of the light beam accumulated through branch 2 is $\phi_2 = \phi_{20} - \pi V/V_\pi$. Because of the presence of the phase modulator in branch 2 we can control the phase difference ϕ and the output intensity I_o.

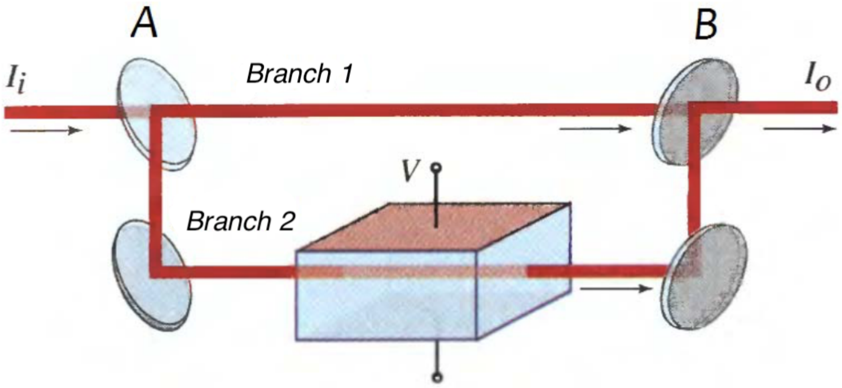

Figure 9: Mach-Zender intensity modulator. Phase modulator is located on branch 2 of the interferometer. A - beam splitter, B - beam combiner. By changing the voltage V we control the phase difference between beams in branches 1 and 2 and by doing so the intensity I_0 at the output of the interferometer. I_i is the light intensity at the input of the interferometer. Arrows show the direction of light propagation.

Transmittance of the interferometer is the quantity that represents the ratio between input and output light intensities, $T = I_o/I_i$. Using (126) we get:

$$T = I_o/I_i = \cos^2(\phi/2) \tag{127}$$

Since the phase difference is controllable by voltage applied to the EOM V it follows that the transmittance is also controllable by V:

$$T(V) = cos^2(\frac{\phi_0}{2} - \frac{\pi}{2}\frac{V}{V_\pi}) \tag{128}$$

Graph of this dependence is given in figure 9

From this figure we see that the device can be used as linear modulator of intensity if we set the phase difference between two branches to about $\pi/4$ and hence work in the area with transmittance of approximately $1/2$. On he other side if set the phase difference to multiple integer integer of $\pi/2$ we would have zero transmittance, $T = 0$. Then if we apply the voltage V_π we would regain the full input intensity at the output, ie $T = 1$. In other words the device acts as an optical switch. It should also be noted that in reality the maximum transmittance is always smaller than 1 because of losses due to reflection, absorption and scattering. Similarly the

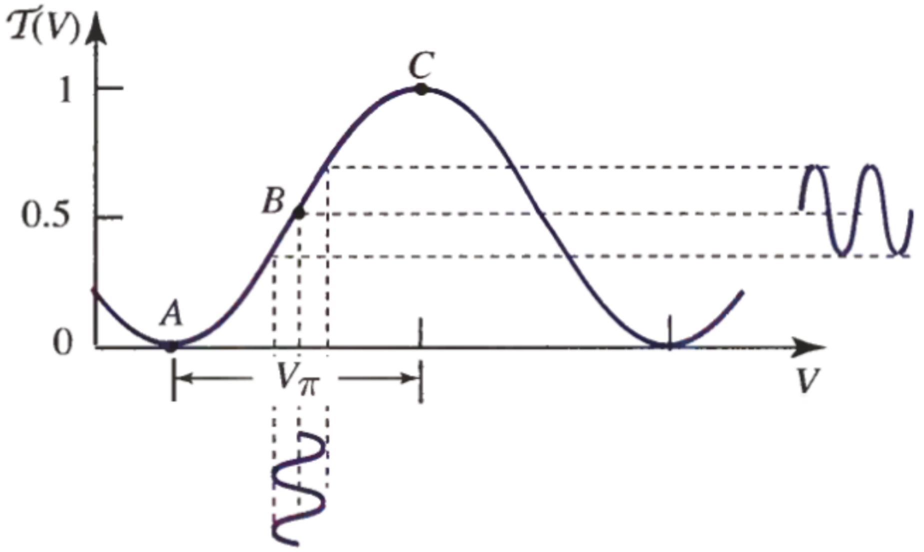

Figure 10: Dependence of transmittance of the EOM and the applied voltage in Mach Zender configuration. In point A we have destructive interference and in point C we have constructive interference. If we want to go from point A to point C we have to change the applied voltage for V_π. Around point B the dependence is approximatelly linear so the dependence of output intensity and the applied voltage is linear in this range.

minimum transmittance is bigger than zero because of non-ideal alignment between axes of polarization of EM wave and axes of the crystal. The ratio between maximal and minimal transmittance is called the extinction ratio. Today it is possible to have EOMs with extinction ratio larger than 30dB ([81]).

3 Four wave mixing in potassium

3.1 Properties of Potassium

Potassium is a member of the first group of periodic table of elements - the group of alkali metals. Its chemical symbol is **K** and atomic number $Z = 19$. Potassium was first isolated by electrolysis of molten potassium hydroxide KOH by Sir Humphry Davy in 1807. Potassium is hydrogen-like atom with one valence electron in the 4s orbital. Potassium has three isotopes - $^{39}K,^{40}K$ and ^{41}K of which ^{40}K is radioactive. Basic properties of potassium isotopes are given in table 1.

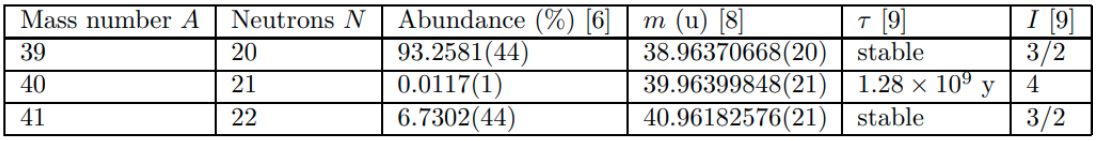

Mass number A	Neutrons N	Abundance (%) [6]	m (u) [8]	τ [9]	I [9]
39	20	93.2581(44)	38.96370668(20)	stable	3/2
40	21	0.0117(1)	39.96399848(21)	1.28×10^9 y	4
41	22	6.7302(44)	40.96182576(21)	stable	3/2

Table 1: Properties of naturally occurring potassium isotopes. ([76])

Potassium has low ionization energy and hence is very reactive. Elemental potassium reacts vigorously with water, generating sufficient heat to ignite hydrogen emitted in the reaction. Because of its high reactivity, elemental potassium is usually stored in paraffin oil. Naturally it occurs only in ionic salts and can be found in many minerals. List of general physical properties of potassium is given in table 2:

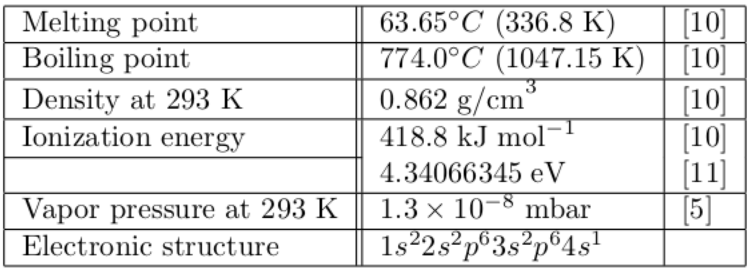

Melting point	63.65°C (336.8 K)	[10]
Boiling point	774.0°C (1047.15 K)	[10]
Density at 293 K	0.862 g/cm^3	[10]
Ionization energy	418.8 kJ mol^{-1}	[10]
	4.34066345 eV	[11]
Vapor pressure at 293 K	1.3×10^{-8} mbar	[5]
Electronic structure	$1s^2 2s^2 p^6 3s^2 p^6 4s^1$	

Table 2: Potassium physical properties. ([76])

In order to perform laser spectroscopic research potassium has to be in vapor state. For this purpose potassium is usually confined in the heated glass vacuum cell where the metal evaporates until the vapor reaches thermodynamic equilibrium. The pressure of the vapor (and simultaneously the density of atoms) is temperature dependent and is given by the following equations ([82]) :

$$(solid) \quad \log p = 7.9667 - \frac{4646}{T} \quad 298K < T < T_m \tag{129}$$

$$(liquid) \quad \log p = 7.4077 - \frac{4453}{T} \quad T_m < T < 600K \tag{130}$$

Graph plot of vapor pressure dependence on temperature is given in figure 9:

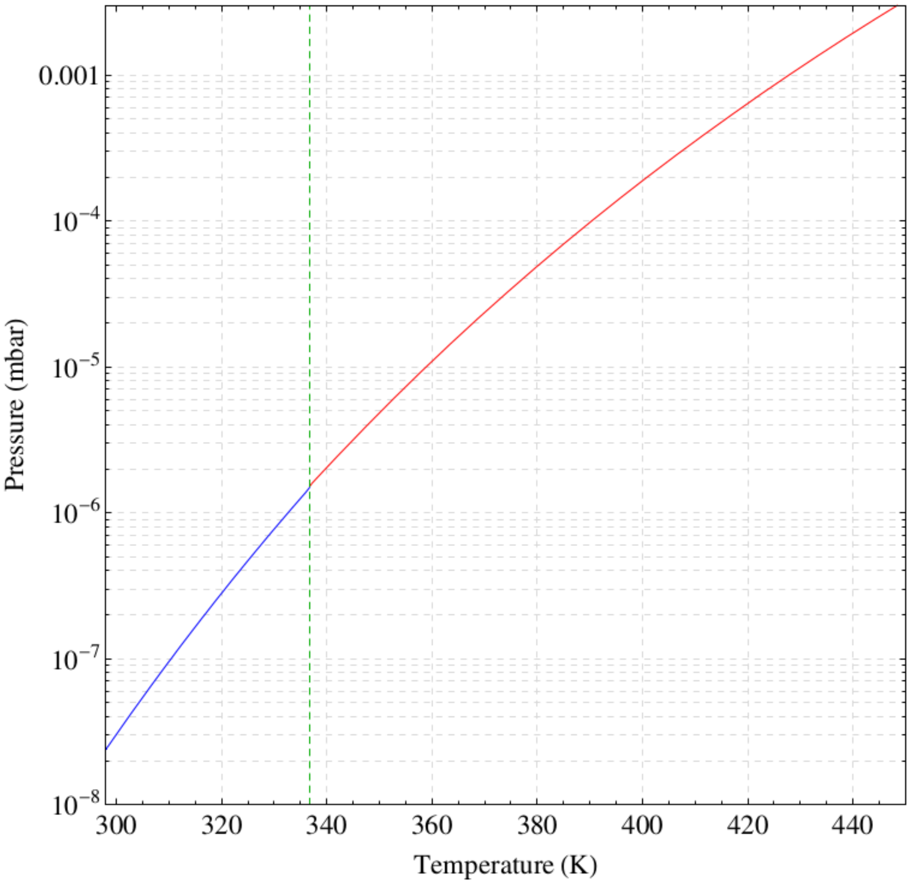

Figure 11: Potassium vapor pressure. $T = 336.8$K is the potassium melting point (dashed green line). Taken from [82]

.

Potassium has two strong spectral lines. First is the so called D1 line on $^2S \longrightarrow ^2 P_{1/2}$transition and so called D2 line on $^2S \longrightarrow ^2 P_{3/2}$ transition. Properties of D1 and D2 lines for three different potassium isotopes are given in the following tables ([83]):

D1 and D2 lines form a fine-structure doublet which is a consequence of spin-orbit interaction. This interaction originates from the coupling of the orbital angular momentum **L** of the valence electron and its spin **S** with corresponding quantum

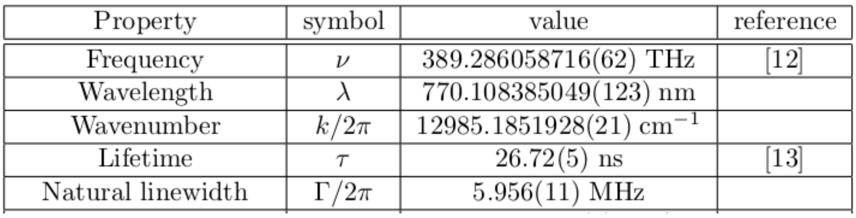

Property	symbol	value	reference
Frequency	ν	389.286058716(62) THz	[12]
Wavelength	λ	770.108385049(123) nm	
Wavenumber	$k/2\pi$	12985.1851928(21) cm^{-1}	
Lifetime	τ	26.72(5) ns	[13]
Natural linewidth	$\Gamma/2\pi$	5.956(11) MHz	

Table 3: D1 line properties of ^{39}K

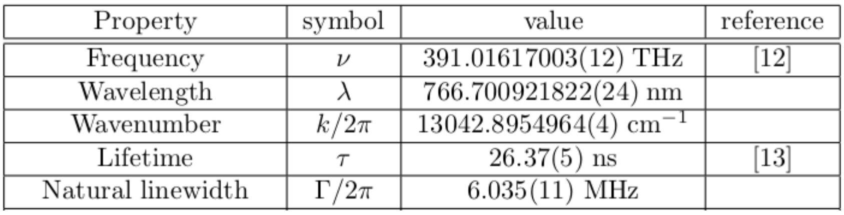

Property	symbol	value	reference
Frequency	ν	391.01617003(12) THz	[12]
Wavelength	λ	766.700921822(24) nm	
Wavenumber	$k/2\pi$	13042.8954964(4) cm^{-1}	
Lifetime	τ	26.37(5) ns	[13]
Natural linewidth	$\Gamma/2\pi$	6.035(11) MHz	

Table 4: D2 line properties of ^{39}K

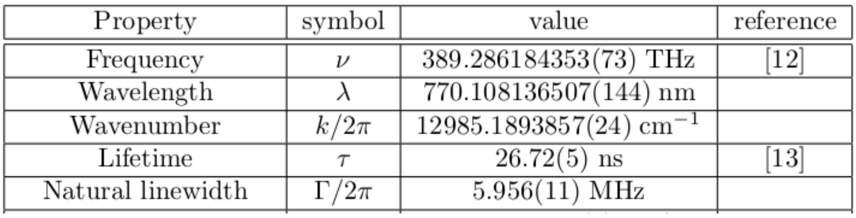

Property	symbol	value	reference
Frequency	ν	389.286184353(73) THz	[12]
Wavelength	λ	770.108136507(144) nm	
Wavenumber	$k/2\pi$	12985.1893857(24) cm^{-1}	
Lifetime	τ	26.72(5) ns	[13]
Natural linewidth	$\Gamma/2\pi$	5.956(11) MHz	

Table 5: D1 line properties of ^{40}K

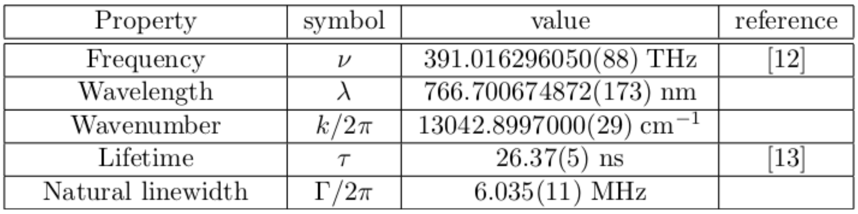

Property	symbol	value	reference
Frequency	ν	391.016296050(88) THz	[12]
Wavelength	λ	766.700674872(173) nm	
Wavenumber	$k/2\pi$	13042.8997000(29) cm^{-1}	
Lifetime	τ	26.37(5) ns	[13]
Natural linewidth	$\Gamma/2\pi$	6.035(11) MHz	

Table 6: D2 line properties of ^{40}K

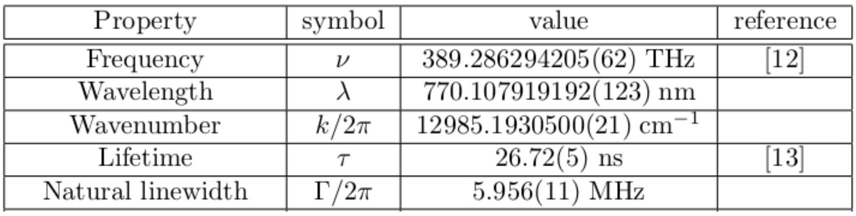

Property	symbol	value	reference
Frequency	ν	389.286294205(62) THz	[12]
Wavelength	λ	770.107919192(123) nm	
Wavenumber	$k/2\pi$	12985.1930500(21) cm^{-1}	
Lifetime	τ	26.72(5) ns	[13]
Natural linewidth	$\Gamma/2\pi$	5.956(11) MHz	

Table 7: D1 line properties of ^{41}K

numbers L and S respectively. Vector sum of orbital and spin angular momentum gives total angular momentum :

$$\mathbf{J} = \mathbf{L} + \mathbf{S} \tag{131}$$

Property	symbol	value	reference
Frequency	ν	391.01640621(12) THz	[12]
Wavelength	λ	766.70045870(2) nm	
Wavenumber	$k/2\pi$	13042.903375(1) cm^{-1}	
Lifetime	τ	26.37(5) ns	[13]
Natural linewidth	$\Gamma/2\pi$	6.035(11) MHz	

Table 8: D2 line properties of ^{41}K

The associated quantum number is denoted as J which takes the following values:

$$|L-S| \leq J \leq L+S \tag{132}$$

Quantum number J gives the magnitude of orbital electronic angular momentum $\mathbf{J}$ which is equal to $\hbar\sqrt{J(J+1)}$. In the case of potassium the ground state is the $4^2S_{1/2}$ level which (being the S state) has orbital momentum $L=0$ and spin $S=1/2$ so the only possible value of J (132) is $J=1/2$. For the first excited P state we have $L=1$ and $S=1/2$ which results in two possible values for J (132) $J=1/2$ and $J=3/2$. This fine structure interaction lifts the degeneracy of the $4^2P_{1/2}$ and $4^2P_{3/2}$ levels and gives rise to the D1 and D2 lines (fine-structure doublet).

The interaction between nuclear angular momentum and total electronic angular momentum further splits the fine-structure levels and gives rise to the hyperfine structure. Coupling of the nuclear spin $\mathbf{I}$ and electronic angular momentum $\mathbf{J}$ gives the total atomic angular momentum $\mathbf{F}$:

$$\mathbf{F} = \mathbf{J} + \mathbf{I} \tag{133}$$

Quantum number F associated with the operator $\mathbf{F}$ takes values in the range:

$$|J-I| \leq F \leq J+I \tag{134}$$

and, similar to J, is the magnitude of total electronic angular momentum $\mathbf{I}$ which is equal to $\hbar\sqrt{I(I+1)}$. The energy shift of the hyperfine levels is given by the following expression ([84]) :

$$\Delta E_{hf} = \frac{a_{hf}}{2}[F(F+1) - I(I+1) - J(J+1)] \tag{135}$$

which for a ground state $J=1/2$ spin $S=1/2$ in zero external field reduces to:

$$\Delta E_{hf} = \frac{a_{hf}}{2}(I+\frac{1}{2}) \tag{136}$$

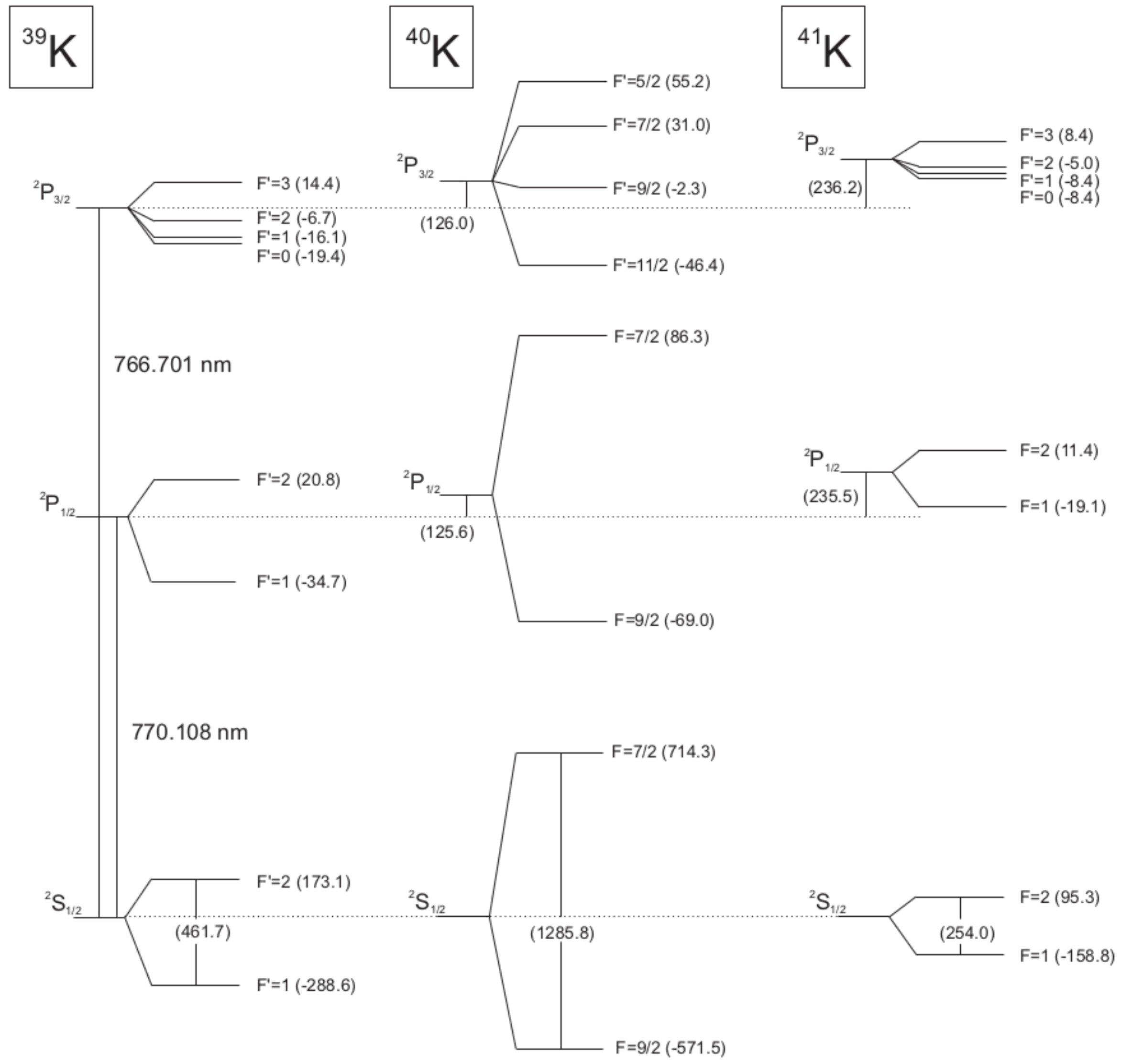

Figure 12: Detailed atomic structure of the D1 and D2 lines given for ^{39}K, ^{40}K and ^{41}K. Hyperfine splitting energies are taken from [84] and [83]

(a_{hf} is the magnetic dipole constant)

Hyperfine structure of potassium isotopes $^{39}K,^{40}K$ and ^{41}K are given in figure 16

The research of coherent effects in this work was done entirely on D1 line of ^{39}K. Because of this we will examine this transition in more detail. Since the atoms in gas follow Maxwell-Boltzmann velocity distribution the D1 line is subjected to Doppler broadening ([85]). The maximum splitting between the four hyperfine transitions of the D1 line (figure 12) is smaller than the Doppler width (825 MHz at

69°C Doppler width ([86]) vs 461.7 MHz hyperfine groundstate splitting for ^{39}K) . Due to this fact hyperfine structure cannot be observed with standard spectroscopic techniques (ie tuning the laser frequency around the atomic transition). Fortunately there are several techniques that can resolve spectral lines with width smaller than the Doppler width (so called *Doppler free* techniques). One of those techniques is *saturated absorption spectroscopy* which uses probe-pump configuration of counter–propagating beams derived from a single laser ([85]). Let z be the axis of propagation of counter-propagating pump and probe beams and v_z be the z-component of the atoms velocity vector. Then in general, due to the Doppler shift, the atoms will see different frequencies of the pump and the probe beam. If the atom is moving towards the pump, in the atom's frame of reference the pump beam will have frequency $\omega_0 + kv_z$ and the probe beam will have $\omega_0 - kv_z$ where ω_0 is the laser frequency in the laboratory frame of reference, kv_z is the scalar product between the laser's wave vector and z-component of atom's velocity. But for the group of atoms with $v_z = 0$ the pump and the probe beam will have the same frequency. When ω_0 is on hyperfine resonance the pump beam would excite atoms form the velocity group $v_z = 0$ (i.e. saturate the transition) and there would be less atoms from this group left to absorb the probe beam. So if we detect the probe photons we will observe increased transparency peak on the hyperfine resonances due to this effect.

In this setup additional structure arises, the so called *cross-over resonances* ([85]). These resonances occur on frequencies halfway between two hyperfine transitions and are also caused by the Doppler shift of the pump and the probe beams in the atoms reference frame in the situation where one beam is resonant with the lower and other beam with the higher transition. The observed features are useful for stabilization of laser frequency with respect to an atomic transition, as well as for determining the properties of atomic vapor (number density, temperature, hyperfine splitting), etc. but on the other side complicate the spectrum and can lead to the spectral lines overlap if the lines are close or the other line broadening effects are strong. Typical hyperfine spectrum of the ^{39}K is shown in figure 13.

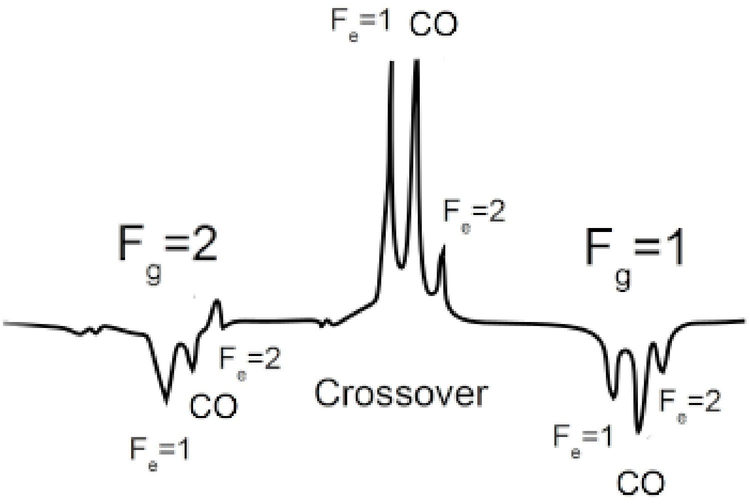

Figure 13: Typical hyperfine structure of the D1 line of ^{39}K obtained by saturation spectroscopy and lock-in amplification detection ([86]). Three groups of three lines correspond to different ground states and a crossover. Within each group there are three peaks corresponding to different hyperfine and crossover resonances.

3.2 Double lambda scheme on D1 line of Potassium and theoretical motivation

In our work double lambda scheme was implemented on D1 line of potassium ^{39}K (figure 19)

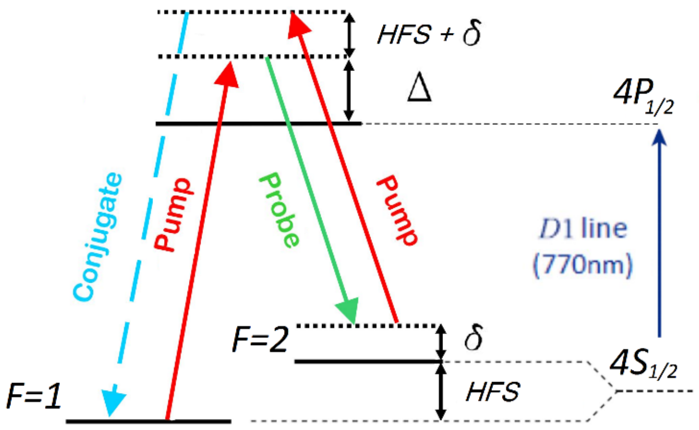

Figure 14: Double lambda scheme on D1 line of ^{39}K. Picture taken from [34]

Ground-state level ${}^4S_{1/2}$ has two hyperfine sublevels with quantum numbers $F = 1$ and $F = 2$. Hyperfine splitting of ${}^4S_{1/2}$ level is $HFS = 461.7$MHz. Hyperfine splitting of the first excited state ${}^4P_{1/2}$ is 55.5MHz and can be omitted. Intensive laser beam - the pump, couples hyperfine sublevel of the ground-state with first excited state ${}^4P_{1/2}$. The detuning of this coupling is called *one-photon detuning* and is denoted by Δ. Weak laser beam - the probe, couples the excited level with $F = 2$ hyperfine sublevel of the ground state. The detuning of this coupling is called *two-photon detuning* and is denoted by δ. Beacuse of its strong intensity the pump also couples $F = 2$ sublevel of the ground-state with a virtual level which is energetically above the excited ${}^4P_{1/2}$ level by $\Delta + HFS + \delta$. Lastly the virtual level is coupled with the lower hyperfine sublevel $F = 1$ via so called conjugate beam which effectively closes this cyclical four-wave mixing scheme.

Atomic susceptibilities govern the four-wave mixing process and affect the amplification of probe and conjugate beams. The dependence of the probe - conjugate cross susceptibility $|\chi_{pc}|$ on hyperfine splitting and two-photon detuning is shown in figure 15 and is calculated according to equations A12–A20 given in the appendix of [77].

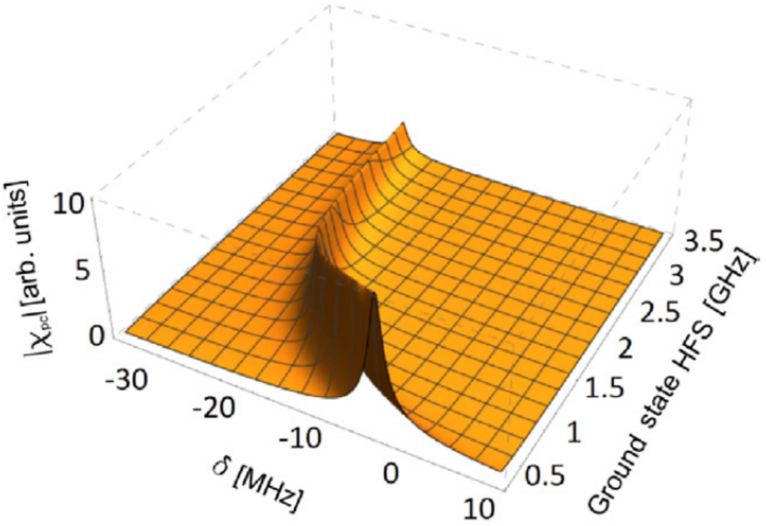

Figure 15: Dependence of $|\chi_{pc}|$ on ground state hyperfine splitting and two-photon detuning δ. The one-photon detuning ($\Delta = 700$MHz) and dipole matrix elements of the double-Λ scheme transitions were kept constant. Picture taken from [34].

The equations enable the calculation of the stationary values of $|\chi_{pc}|$ as a function of the relevant experimental parameters: one-photon detuning, two-photon detuning, ground state hyperfine splitting, pump laser Rabi frequencies, and the concentration of the atoms, i.e. the temperature. The equations are given under the assumption that Rabi frequencies for both pump transitions in figure 14 are equal. The probe and conjugate fields are assumed to be weak and their contribution is kept only to the first order. Since we want to estimate the influence of ground state hyperfine splitting of alkali atoms on the efficiency of four-wave mixing we kept all other quantities constant and varied two-photon detuning only. The results show that the maximum of $|\chi_{pc}|$ increases as hyperfine splitting decreases. The model also predicts that the two-photon detuning δ, corresponding to the maximum $|\chi_{pc}|$, also decreases, indicating that both Λ schemes should be closer to n resonance.

This analysis, besides the ones pointed out in Introduction, motivated us to try to achieve four-wave mixing in potassium since it has the lowest hyperfine splitting of the ground-state level among all alkalis (taking into account stable isotopes only).

3.3 The Laser System

Our laser system for the experiment consist of Coherent MBR 110 Ti:Sapphire laser pumped by Coherent Verdi 5 Nd:YVO$_4$.

- **Verdi 5 Pump** Verdi 5 by Coherent is a laser system itself which consists of strong pump diode laser and Neodymium Vanadate (Nd:YVO$_4$) laser. Nd:YVO$_4$ single frequency, solid state laser provides single-frequency green (532 nm) output at power levels greater 5 Watts. The major optical elements of the laser include:
    - ∗ Vanadate as the gain medium
    - ∗ LBO (lithium triborate) as the frequency doubling crystal
    - ∗ An etalon as the single-frequency optic
    - ∗ Optical diode
    - ∗ Astigmatic compensator and three cavity mirror

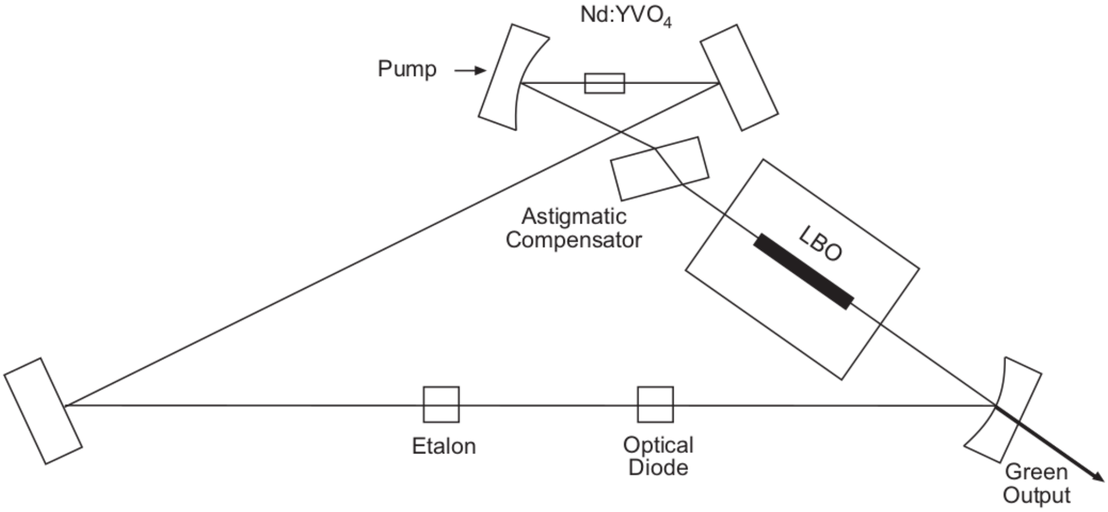

Figure 16: Verdi 5 optical scheme

Scheme of the Verdi 5 is given in figure 16.

The frequency doubling nonlinear crystal is LBO which is non-critically phase matched. The crystal is heated to around 150°C by a resistive heater in order to have the best possible nonlinear efficiency. The temperature of the Vanadate and etalon is also controlled for best possible efficiency. For this purpose thermo-electric coolers (TECs) are used which can either cool down or heat when necessary. Bidirectional wave propagation inside the ring resonator is prevented by using the so called optical diode which favors one direction over the other by utilising the Faraday rotation effect ([81]). The function of the etalon is to reinforce single mode operation. Nd:YVO$_4$ gain medium is pumped by strong FAP-I (Fiber Array Package – Integrated) laser diode which operates at 808nm. Diode laser light is fiber coupled with Verdi 5.

- **MBR 110** is single frequency, solid state laser that utilizes Ti:Sapphire crystal as its gain medium. The major optical elements of the laser include (figure 19):

  ∗ Ti:Sapphire as the gain medium

  ∗ Birifringent filter for coarse frequency tuning

  ∗ An etalon for single-frequency operation and fine frequency tuning

∗ Optical diode for unidirectional operation

∗ Bruster plates for frequency scaning

∗ Temperature stabilized Reference Cavity for frequency locking and linewidth reduction

The gain medium is pumped by 5W, 532nm green light from Vergi 5 which travels through free space from Verdi 5 to MBR 110.

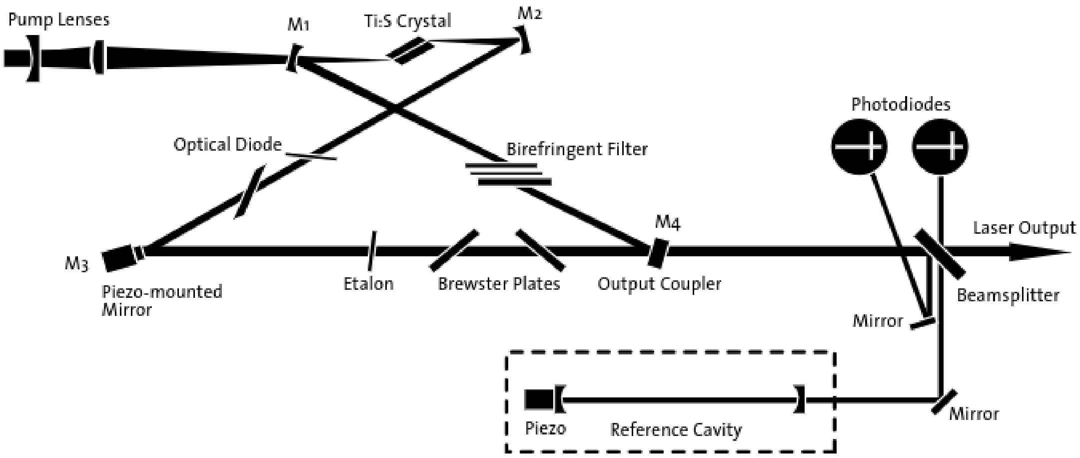

Figure 17: MBR 110 optical scheme

MBR laser uses ring resonator and unidirectional propagation achieved by an optical diode to avoid spatial hole burning effect ([85]). Reducing spatial burning effect leads to single mode operation and increased laser power. Ti:Sapphire has a very broad emission spectrum 720 - 940 nm at pump power of 5W. In order to tune across the entire tuning range, whilst maintaining single frequency operation and preventing mode-hops, two intracavity filters are required. Tuning element used to obtain the required wavelength from a laser is a birefringent filter. This is a relatively coarse wavelength control and so an intracavity thin etalon ensures single frequency operation and is used to allow fine tuning of the laser wavelength as well. This etalon is also used to prevent laser mode-hops whilst the laser is being fine tuned, and scanned. The method used to prevent mode-hopping is a locking scheme whereby the transmission of the etalon is locked to the laser frequency.Within the laser cavity are two Brewster angled glass plates. These plates are mounted in such a way that when they are rotated they alter the optical length of the laser without diverting the intracavity laser beam path. Using this technique the laser frequency can be scanned in a controlled manner. Scanning range specified by the manufacturer is ± 30 GHz but we've never achieved more than ± 10GHz without loosing frequency lock. A fraction of the Ti:Sapphire laser output is directed into a temperature controlled, hermetically sealed, Invar stabilized reference cavity. By locking the laser to one of the fringes of the high finesse reference cavity the laser linewidth can be reduced to less than 75 kHz. Using a long extension piezo ceramic the reference cavity length can be scanned. Strain gauges monitor the reference cavity length with a high degree of linearity and precision. Consequently, the laser can be scanned by maintaining the laser lock to the scanning reference cavity. The ring resonator is made from a single block of aluminum which gives the laser stability and consequently a narrower linewidth.

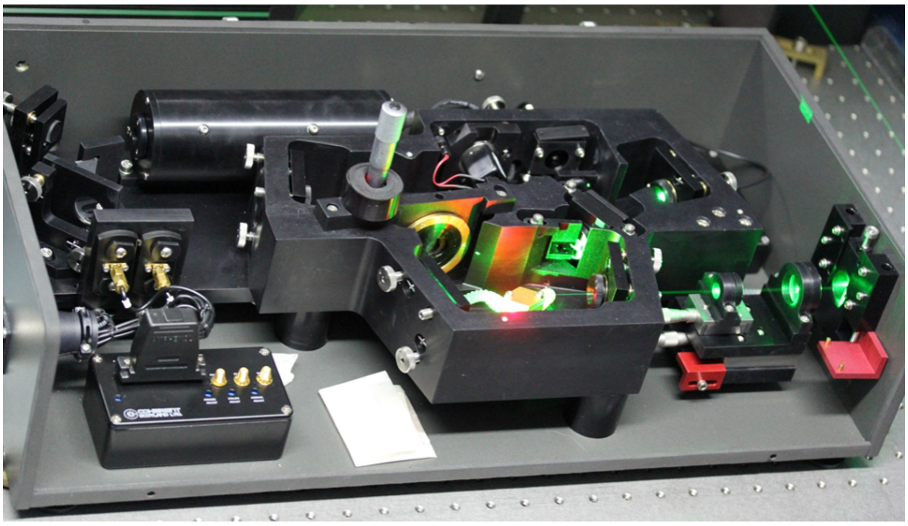

Figure 18: MBR 110 in operation

3.4 Experimental setup

Experimental setup is based on [32] with certain changes and additions. Scheme of the experimental design is shown in figure 19.

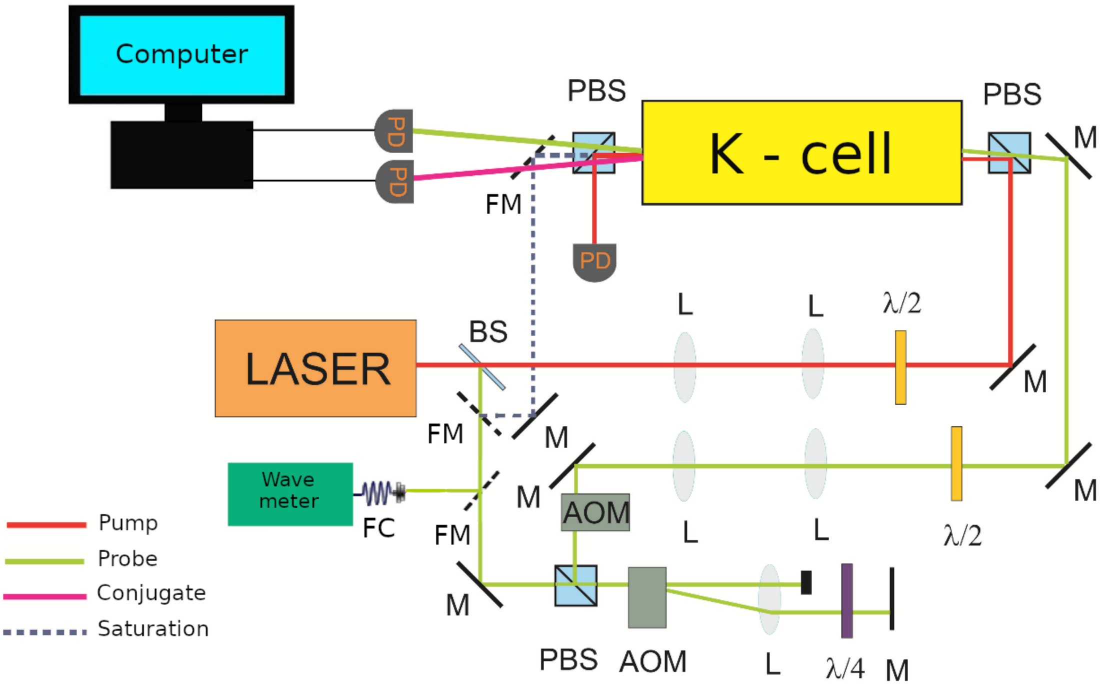

Figure 19: Scheme of experimental setup for four-wave mixing in potassium. BS - beam splitter, PBS - polarization beam splitter, M - mirror, FM - flip-mirror, FC - fiber coupler, AOM - acousto-optic modulator, L - lens, $\lambda/2$ - lambda-half wave plate, $\lambda/4$ - lambda-quarter wave plate, PD - photo diode

MBR-110 Ti:Sapphire delivers up to 600mW of light at D1 line of ^{39}K (770.108 nm) and it is used for both the pump and probe beams. The beam is first split by the 90:10 beam splitter. Stronger, non reflected beam is used as a pump beam in the experiment (red beam in figure 19). The reflected beam (green beam in figure 19) has several purposes. When the flip mirrors are up it serves as a pump in saturation spectroscopy scheme (see **3.4.1**). Also a small fraction of the beam is picked on the plane-parallel plate, fiber-coupled and sent to the wave-meter for coarse frequency measurement. Effectively we have two steps of laser frequency calibration - first, coarse using wave-meter and second, fine using saturation spectroscopy. Finally the reflected beam serves as a probe in our FWM experiment. The beam is sent to acoustooptic modulator in double pass configuration (see **3.4.2**) where its frequency is shifted for approximately hyperfine splitting of the ^{39}K ground state. Two-photon detuning δ is scanned by changing the RF frequency fed to the first AOM (also see

3.4.2). Using two $\lambda/2$ wave plates we alter the plane of polarization of the pump and probe beams in order to make them mutually orthogonal. The beams are then combined at a polarization beam splitter and sent through the 50 mm long, natural-abundance vacuum potassium vapor cell (see **3.4.3**). The cell is heated using system based on hot air (see **3.4.3**). Pump and probe beam intersect inside the cell at a small angle that is changed by the mirror in the range 2-10 mrad. Both beams, the pump and the probe seed, are focused at the intersection by using a pair of AR-coated lenses and their waists are 1.05 mm and 0.8 mm, respectively. After passing through the vapor cell, the pump beam is reflected by the second polarizing beam splitter. The newly created conjugate beam (which has the same polarization as the probe seed) and the amplified probe beam are detected by two photodiodes (Hamamatsu S3883).

3.4.1 Frequency calibration and stability - saturation spectroscopy and frequency drift

As mentioned in **3.1** saturation spectroscopy (SS) setup had two counter-propagating beams with same frequency. First beam, the pump, saturates (in our case hyperfine) transitions while the probe probes those transitions and gets detected. In order to determine the long term frequency stability of the laser and to determine one photon detuning we have incorporated the saturation spectroscopy (SS) setup into our experiment. To this end we have added two flip mirrors which divert the probe beam before the double-pass AOM making it the saturation beam in SS configuration (dashed gray beam in figure 19) which counter propagates the pump in the vapor cell. The intense pump (red beam in figure 19) becomes the probe. Because of its high intensity this beam is strongly attenuated by using $\lambda/2$ plate and polarization beam splitter. SS pump and probe overlap in the potassium vapor cell and after the interaction with the atoms the probe beam gets detected on the photodiode.

Spectrum with hyperfine resolved features is given in figure 20. The temperature of the vapor was 67^0C, pump power 7mW and probe power 400μW. This spectra is obtained by subtracting Doppler profile from the SS signal. We can distinguish three groups of lines corresponding to different sublevels of the ground state of ^{39}K.

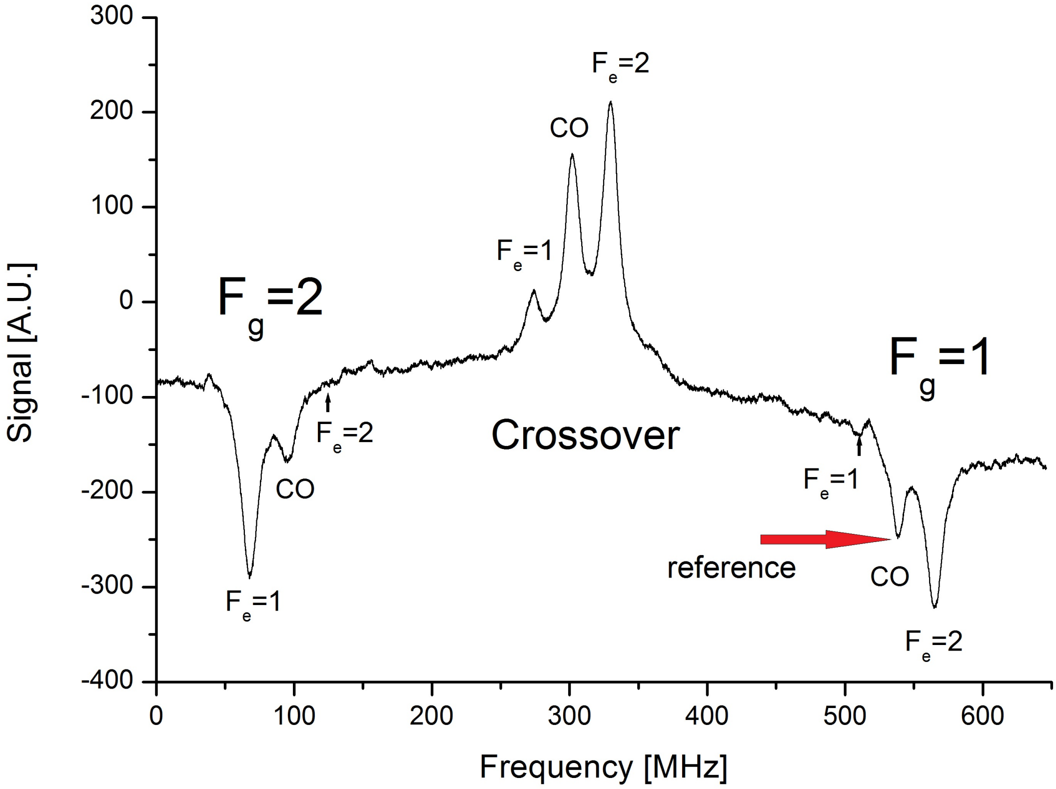

Figure 20: Saturation spectra of the D1 line of ^{39}K

Within these three groups there are three peaks (except for $Fg = 2$ group) which correspond to different hyperfine transitions. We have used the $Fg = 1 \longrightarrow CO$ transitions as our reference for one-photon detuning.

In order to perform quality measurements the temporal frequency stability of the laser is essential. For measuring the potential frequency drift of the laser we have locked our laser frequency to the reference peak (Figure 24) and observed the change of the level of the signal from the photodiode. The change of the level of the signal corresponds to frequency drift of the laser.

First we've calibrated laser frequency drift to the corresponding change of photodiode signal. After that we've performed multiple measurements of the laser frequency drift (10 times) and linearly fitted the results. Example of one frequency drift measurement and the linear fit is shown in figure 21. From the linear fit we obtain the value of the slope which is (0.01 ± 0.002) MHz/s. This translates to about 0.5 MHz/min. Since FWM process is very sensitive to two-photon detuning and two-photon detuning is usually in order of several MHz we've put a time limit

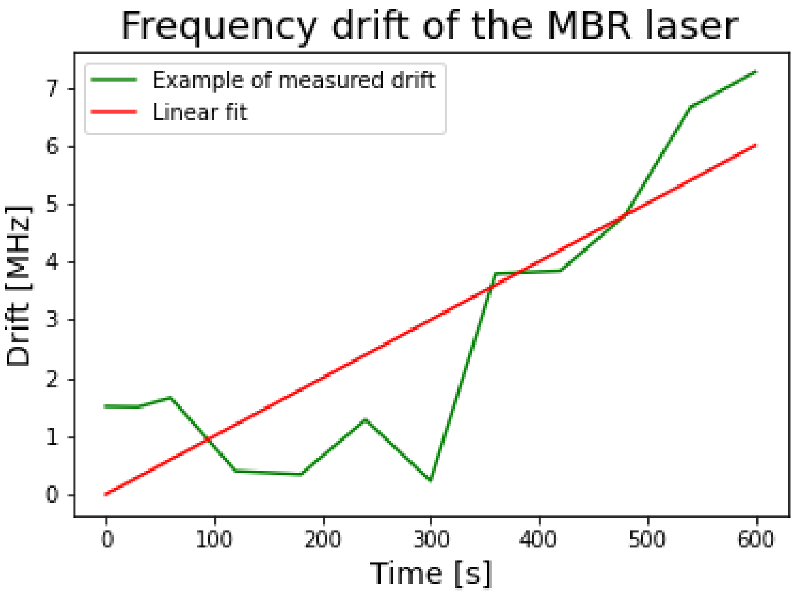

Figure 21: Measuring temporal frequency drift of the MBR 110 laser. Example of one measurement is shown in green, while the linear fit is given in red

of our single FWM measurements to one minute. After a single FWM measurement we would quickly put the experiment in saturation spectroscopy mode and look for unexpected large frequency jumps. If the jump occurred we would disregard the measurement.

3.4.2 Double-pass acoustooptic modulator

As mentioned in 3.4 we use acoustooptic modulator in double-pass configuration for two-photon detuning scanning. AOM is an optical device that uses the interaction between light and ultrasound waves to change the intensity, phase, frequency and direction of the incident optical beam ([81])(figure 22).

Its main part is an optical crystal in which the diffraction of light can be realized. When an ultrasonic wave propagates through the crystal a series of stresses occur which spread through the crystal. In parts where the sound pressure is higher a small crystal compression occurs which causes a large change in the refractive index at that location. Consequently in the parts where the pressure is lower the refractive index is also lower so we get modulation of the refractive index within the whole crystal ([81]). The modulation effectively acts as a diffraction grating on which scat-

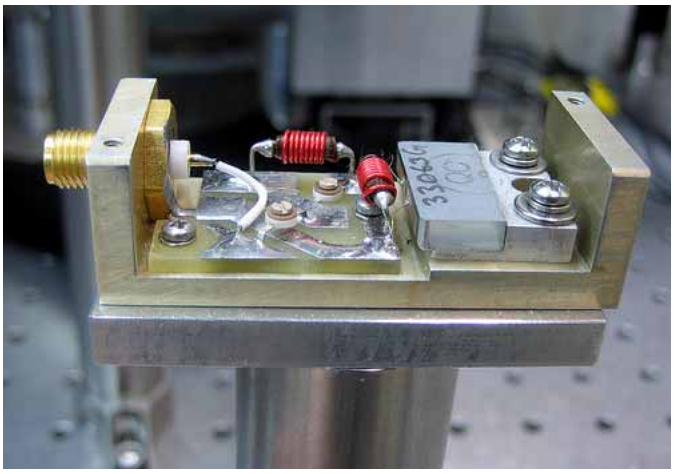

Figure 22: Acoustooptic modulator - Isomet 1205-C

tering of photons occurs. The dominant effects that lead to diffraction are Bragg and Raman-Nath diffraction ([81]). The result is that the light beam passing through the crystal is diffracted into several diffraction orders. An important consequence is that every diffraction order has a light frequency shift equal to integer product of the sound wave frequency. For example, light in the first diffraction order would have frequency $\omega_0 + \Omega$ where ω_0 is the frequency of the incident light and Ω is the acoustic wave frequency.

The second important part of the AOM is the piezoelectric transducer which is in contact with the optical crystal. Piezoelectric materials change their physical dimensions in the electric field. When radio frequency voltage is applied to piezoelectric it expands and contracts at the frequency of the applied RF voltage. These oscillations are transferred to the crystal resulting in a sound wave with a flat wave front. The frequency of this wave is equal to the frequency of alternating voltage.

Diffracted beam stands at a certain angle relative to the incident beam. Magnitude of this angle is a function of the frequency of the sound wave traveling through the crystal, $\phi = \phi(\Omega)$. Since we use the AOM not just to make a frequency offset from the pump but also for frequency scanning (two-photon detuning scanning) the fact that angle and consequently the direction of the diffracted beam changes with sound wave frequency is not desirable. In order to remedy this effect we use AOM in so called double-pass configuration (figure 23)

We first add a polarizing beam splitter before the AOM to ensure that light

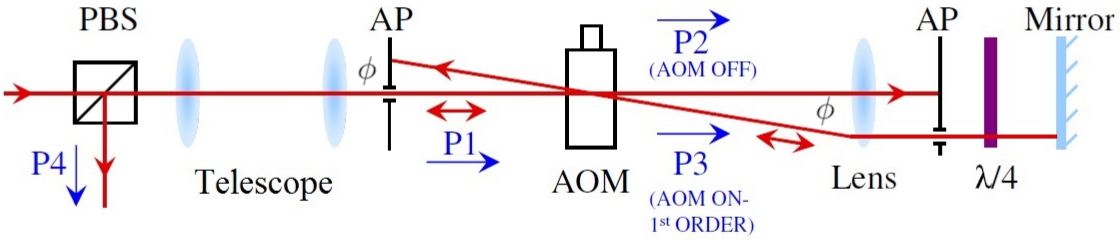

Figure 23: Scheme of AOM in double-pass configuration. PBS - polarizing beam splitter, AP - aperture, AOM - acoustooptic modulator, ϕ - diffraction angle, $\lambda/4$ - lambda-quarter wave plate, P1 - beam entering AOM, P2 - undiffracted beam, P3 - first order diffracted beam, P4 - double diffracted beam

coming to the AOM (P1) is linearly polarized. Before the AOM we place two lenses in telescope configuration. Its function is to shape the beam in order to get the best performance of the AOM. After the AOM we place a lens so that the output aperture of the AOM is in the focus of the lens. The function of the lens is as follows: the beam diffraction angle ϕ is, as mentioned, a function of the frequency of the sound wave through the crystal $\phi = \phi(\Omega)$. This implies that by changing the sound wave frequency Ω the direction of the diffracted beam P3 will also be changed. But since the P3 beam source is in the focus of the lens the beam becomes parallel to the optical axis of the system (defined by the direction of P1) after passing through the lens. Behind the lens we place a mirror (normal to the optical axis) which reflects the diffracted beam in the same direction. After the second pass through the lens the reflected beam focuses on the AOM aperture. After passing through the AOM again, the beam is diffracted by an angle Ω one more time leading to it now becoming collinear with the incident beam P1. The function of the lambda-quarter plate is to separate double-diffracted beam from the incident beam. In the double passage through the $\lambda/4$ plate the plane of polarization of the wave is rotated by a total of $2 \times \pi/4 = \pi/2$ which makes it orthogonally polarized with respect to the input beam. Due to this the double diffracted beam is reflected at the polarization beam splitter (R4). We see that for any change of the frequency of the sound wave through the crystal Ω the direction of the doubly diffracted beam remains the same which is the purpose of the double-pass method.

3.4.3 Potassium vapor cell and the heating system

As mentioned in section **3.1** potassium is usually confined in the glass vacuum cell. We use 50 mm long, natural-abundance vacuum vapor cell (figure 24)

Figure 24: Potassium vapor cell with Brewster angled windows

The windows of the cell are Brewster angled in order to minimize the reflection. The cell is rotated to provide the maximal pump transmission (95% per window). Since the probe seed is polarized perpendicularly to the pump, its transmission is lower (70% per window).

In order to get desired concentration of the potassium atoms we need to heat the cell and control its temperature. To this end we've designed and implemented heating system based on hot air (figure 25).

Our lab is equipped with pressurized air source. Using the valve for air we control the pressure of the air in the system. The pressurized air first goes through flow control. Flow control is made out of aluminum cylinder inside which we've mounted an air fan. The fan generates electric current via electromagnetic induction. This current is fed to the PID controller that essentially detects the presence of the current. If the air flow stops PID controller shuts down the air heater by switching off its power supply. For air heating we use 1kW solenoidal heater. The heater is confined in two concentric aluminum cylinders (figure 25) in order to reduce power and heat dissipation (Appendix blabla).

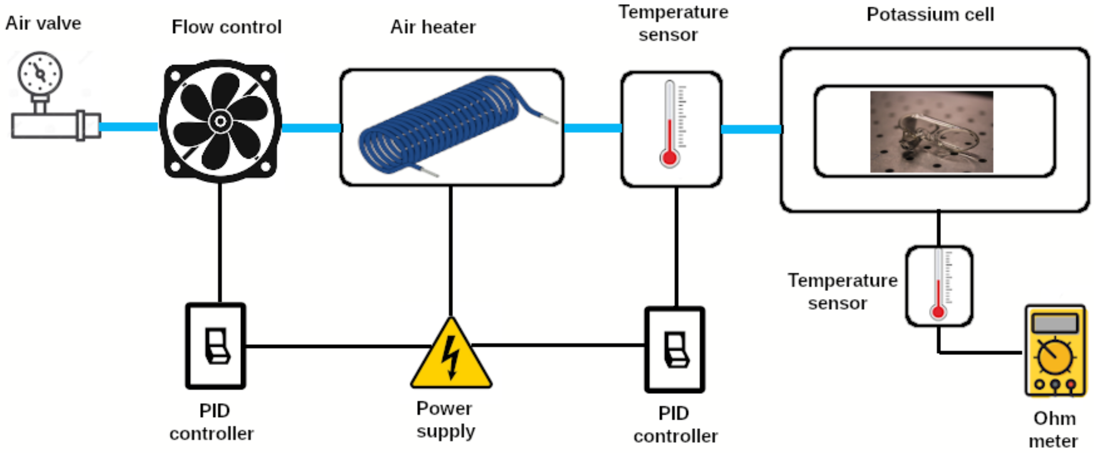

Figure 25: Potassium vapor cell heating and temperature control system

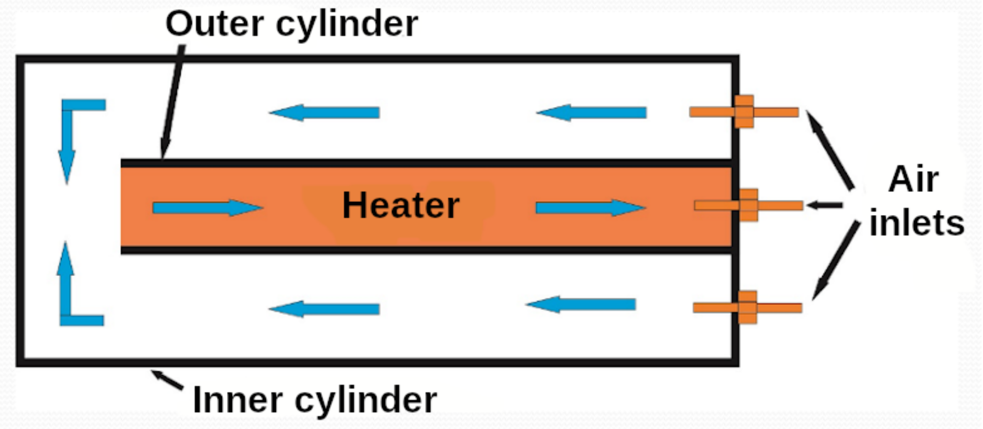

Figure 26: Air heater and double aluminum cylinders scheme. Air flow is represented by blue arrows

The heated air then passes through small aluminum cylinder that contains platinum resistance thermometer pt1000. This is platinum based sensor, with high precision and accuracy capable over a wide range of temperatures ($-200°C$ to $850°C$). This sensor is used for air temperature control. To this end we've assembled another PID controller (appendix balabla) which uses signal from pt1000 sensor. The controller is connected with the power supply of the air heater on and controls it in other to achieve the wanted temperature by turning it off and on. During the experiment integration and differentiation parts of the controller proved to be excessive so we've used only the proportional part.

For the purpose of heating the potassium cell we've machined an aluminum container with cavities for hot air flow (figure 37).

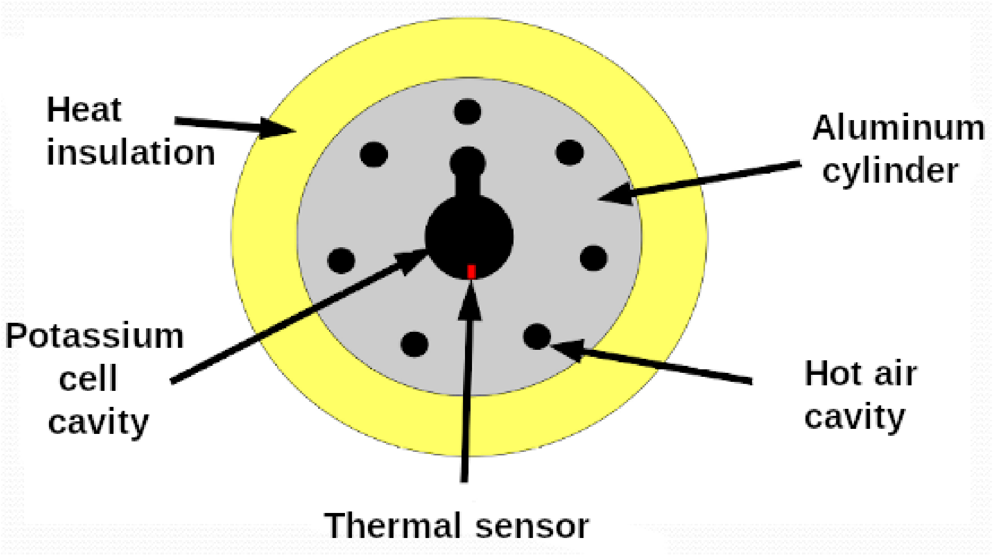

Figure 27: Scheme of aluminum container for potassium vapor cell

When flowing through the cavities hot air heats up the container and consequently the potassium vapor cell. The temperature inside the container is measured by another pt1000 sensor which is placed in the vicinity of the vapor cell. We use the standard lab multimeter for measurement of sensor's electrical resistance and then look up the pt1000 resistance temperature table in order to infer the temperature. Before performing any measurements we would wait for the temperature measured by this sensor to stabilize completely indicating the state of thermal equilibrium between the container and the cell is achieved. On opposite ends of the container we have drilled small openings that allow laser light to go through the vapor cell. The container itself is placed inside the cylindrical shell made out of temperature resistive plastic which serves as heat insulator. The schematics of both the aluminum container and the plastic a heat insulator are given in the Appendix blabla.

3.5 Results and discussion

As mentioned in the Introduction this the first time that the four-wave mixing in potassium vapor in co-propagating geometry was observed. So apart from identifying the conditions that would lead to the highest possible gain we were also motivated to explore this phenomena under different experimental conditions in order to achieve deeper insights. On the other side, due to the high number of parameters, it was not feasible to perform measurements over the whole parameter space so we were forced to investigate parts of this space that we considered the most important. Nonetheless this work can serve as a basis for building intuition about the phenomena and for choosing optimal experimental solutions in the future investigations.

The efficiency of the four wave mixing process is measured by the **gain** of probe and conjugate beams. The gains of the probe and the conjugate are defined as:

$$G_p = \frac{P_p}{P_{in}} \tag{137}$$

$$G_c = \frac{P_c}{P_{in}} \tag{138}$$

respectively, where P_p and P_c are the measured powers of the probe and the conjugate beams, respectively, and P_{in} is initial power of the probe seed inside the amplifying medium

As suggested by equation (99) a certain two-photon detuning is required to compensate AC-Stark light shift and thus maximize transparency. We also note that theoretical calculations (section **3.2**) hint that two-photon detuning needed for AC-Stark compensation decreases with ground state hyperfine splitting. In order to experimentally investigate the of two-photon detuning influence on FWM process we've performed measurements of probe and conjugate gains with one-photon detuning Δ as a parameter. The δ step was 2 MHz. The results for various values of Δ are shown in figure 32.

The maximal conjugate gain $G_c = 82$, was obtained at $\Delta = 700$ MHz and $\delta = -6$ MHz. The probe gain for the same parameters was $G_p = 58$. The reason for the maximum gains occurring at a particular Δ is the competition of two effects: FWM

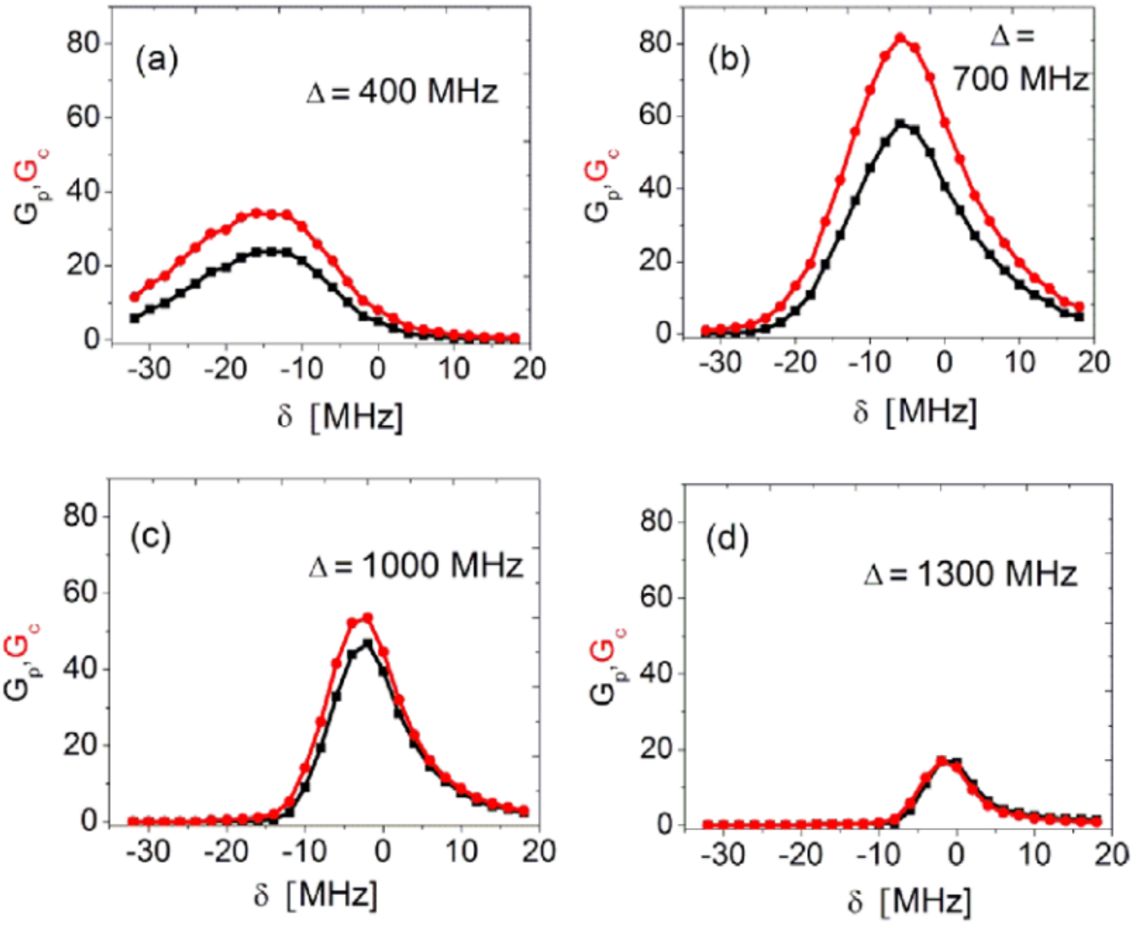

Figure 28: The probe (black squares) and the conjugate (red circles) gain curves versus two-photon detuning δ in the vicinity of Raman resonance ($\delta = 0$) at Δ equal to (a) 400 MHz, (b) 700 MHz, (c) 1000 MHz and (d) 1300 MHz. The pump power was $P_0 = 400$ mW and the probe seed power was $P_{in} = 200$ μW. Vapor temperature was kept constant at 120°C ($\approx 3 \times 10^{12}$ atoms/cm^3 and angle between the pump and the probe was $\phi = 3$ mrad. The lines are to guide the eye. Picture taken from [34].

amplification and one-photon absorption ([32], [77]). When Δ increases, the FWM amplification of the probe and the conjugate beams decreases due to the one-photon Raman detuning, but so does one-photon absorption since we are moving away from the one-photon resonance. The best trade-off in our case is for $\Delta = 700$ MHz (figure 28(b)). Since the frequency offset between the probe and the conjugate beams is $\approx$ 920MHz (approximately double the HFS) and the probe beam is tuned closer to the resonance, one-photon absorption is stronger for the probe beam (figure 29).

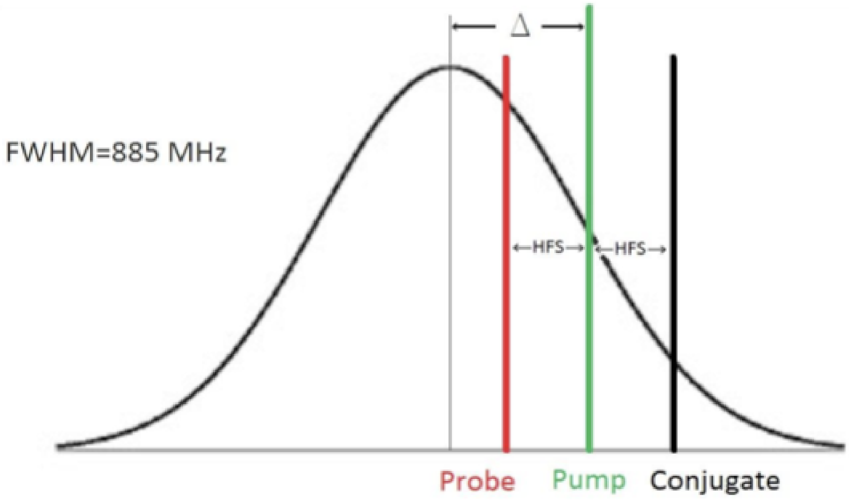

Figure 29: Frequency of the probe, pump and conjugate beams versus one-photon absorption Doppler profile. Δ - one-photon detuning, FWHM - full width half maximum, HFS - hyperfine splitting of the ground state. Due to the vicinity to the resonance the probe beam is experiencing stronger one-photon absorption.

This is the reason why we observe different G_p and G_c for smaller Δ (figures 4(a) and (b)). At larger Δ, one-photon absorption becomes smaller, so does the difference between G_p and G_c (figure 4(d)), but are rather small due to detuning far from resonance. We can also observe that point of maximal gain moves closer to $\delta = 0$MHz as we increase one-photon detuning Δ. This is with accordance with (99) from which we see that the two-photon detuning needed for canceling the AC-Stark shift is inversely proportional to the one-photon detuning. According to our expectations, qualitatively supported by results in figure 28, we have obtained higher gains than in other alkali atoms under comparable experimental conditions. For more detailed theoretical study and quantitative comparison between experimental and theoretical results one might consider adjusting the theoretical model from [77] for particular properties of potassium. Unlike rubidium, all the transitions forming the double$-\Lambda$ scheme in potassium are overlapped due to large Doppler broadening at specified temperatures. Moreover, one might also consider the geometry and intensity profiles of overlapping laser beams and their spectral properties.

The dependence of G_p and G_c on the temperature for various values of Δ is shown in figure 30.

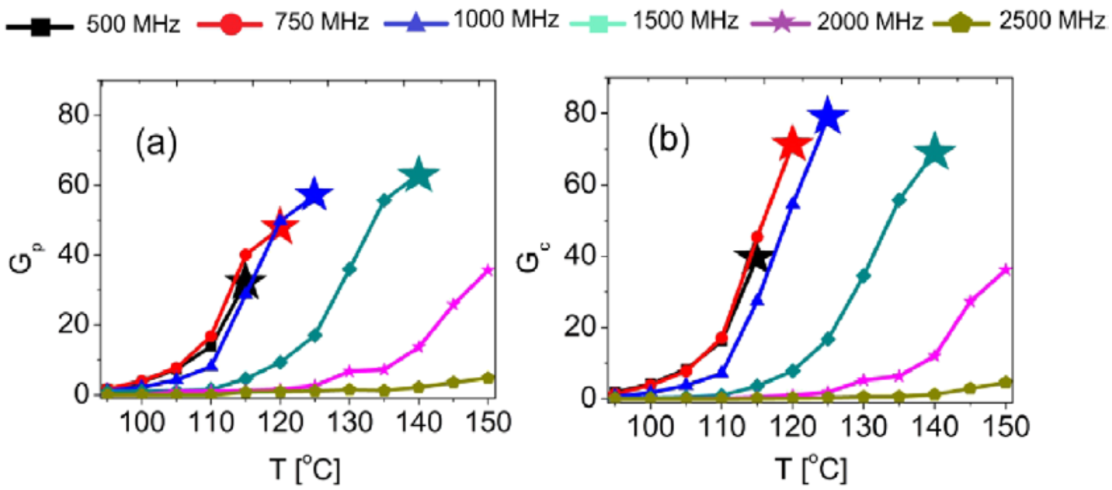

Figure 30: Temperature dependence of (a) the probe gain G_p and (b) the conjugate gain G_c. Different colors correspond to the different values of Δ (given in the legend above). For the given range of the temperature of potassium vapor the number density of the atoms, calculated according to[76], is between 3.710^{11} atoms/cm^3 (at $90°C$) and 1.710^{13} atoms/cm^3 (at $150°C$). Stars denote the temperatures at which filamentation and self-focusing of the probe and the conjugate beams occur. Parameters are $P_0 = 400$mW, $P_{in} = 200\mu$W, $\Delta = 700$, $\phi = 2$mrad. Picture taken from [34].

For each Δ on the graph, we set δ to maximize the gains of the probe and the conjugate beams. As the concentration of potassium atoms increases, the cross-susceptibilities (χ_{cp} and χ_{pc}) also increase ([77]). On the other hand, large susceptibilities lead to large values of the refractive index and its transverse gradient that cause beam self-focusing and beam filamentation ([17], [77]). Stars in figure 30 indicate the highest temperatures for particular values of Δ, above which aforementioned effects prevent the proper measurement of the intensities of the probe and the conjugate beams. At high vapor temperatures and/or pump intensities self-focusing of the probe and conjugate beams appears gradually, ending up with beam break-up ([17]). As the pump intensity and/or vapor temperature increases the probe and the conjugate beams become more divergent due to self-focusing. This makes the beams partially overlapped and hinders proper measurement of the powers independently. Varying the temperature and Δ we have determined that the values of T $= 140°C$ and $\Delta = 1500$ MHz provide the highest probe gain, $G_p = 63$ (we found $G_c = 69$ for the same set of parameters). The dependence of G_p and G_c on the mutual angle between the pump and the probe beam is presented in figure 31.

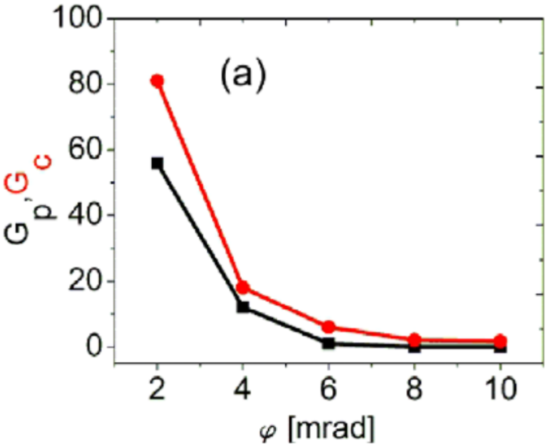

Figure 31: Dependence of the probe (black squares) and the conjugate (red circles) gain on the angle ϕ between the pump and the probe beams. Parameters are P_0 = 400mW, P_{in} = 200μW, Δ = 700 MHz, T = 120°C. Picture taken from [34].

While in rubidium ([77]) the dependence on this angle has a maximum at 5 mrad, in potassium it monotonically decreases. This is in accordance with[28] where, in their configuration of counter-propagating pumps and degenerate FWM, the probe reflectivity can be considered as an analogue to the probe gain, since both are affected by atomic susceptibility. Lastly we've measured the dependence of the probe and the conjugate gains on the pump power (figure 32).

We found that the lowest pump intensity, at which we were able to detect the conjugate beam, is about 10 W cm^{-2} corresponding to laser power of ≈100mW. This, relatively low, laser power can easily be attained with conventional lasers diodes. On the other side we were able to measure even higher gains (96 for the conjugate, 73 for the probe) at a pump intensity of 51 W cm^{-2} but the laser becomes unstable at high powers. This indicates that further improvements could be made with even stronger lasers.

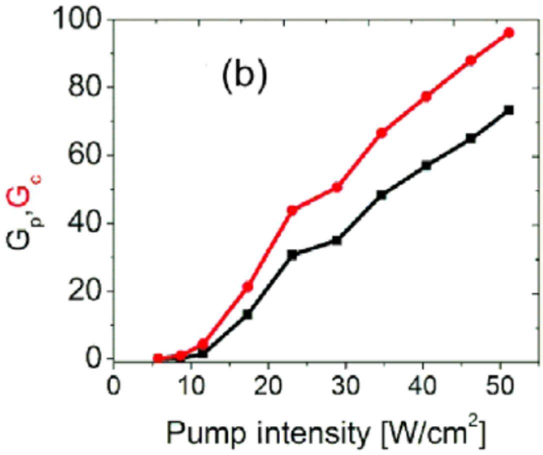

Figure 32: Dependence of the probe (black squares) and the conjugate (red circles) gain on the pump intensity between the pump and the probe beams. Parameters are $P_{in} = 200\mu$W, $\Delta = 700$ MHz, $\phi = 2$mrad, T $= 120°C$. Picture taken from [34].

4 Slowing short light pulses in hot potassium vapor

For the investigation of slowing short light pulses we have used the double-Λ scheme realized on the $D1$ line of potassium as explained in section **3.2**. as our slowing medium. We have also used the same laser system (section **3.3**) , frequency calibration (section **3.4.1**) , technique for two-photon detuning scanning (section **3.4.2**) and potassium vapor cell and heating system (section **3.4.3**) as for the four wave mixing research. The experimental setup (section **3.4**) is slightly modified in order to make the research of slowing light pulses viable and is presented in the next section.

4.1 Experimental setup

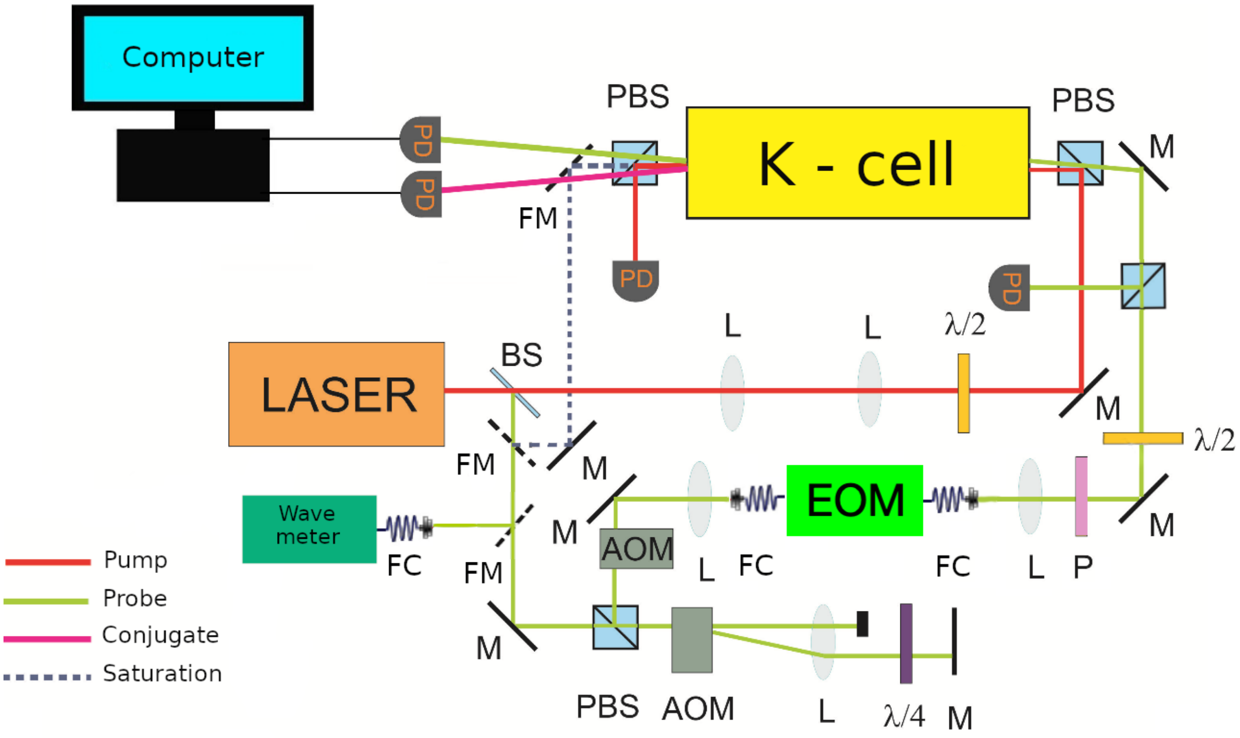

Figure 33: Scheme of experimental setup for slowing of short light pulses. BS - beam splitter, PBS - polarization beam splitter, M - mirror, FM - flip-mirror, FC - fiber coupler, AOM - acousto-optic modulator, L - lens, $\lambda/2$ - lambda-half wave plate, $\lambda/4$ - lambda-quarter wave plate, PD - photo diode, EOM - electro-optic modulator

The main difference from the setup in section **3.4** is adding the electro-optic (EOM) modulator after the second AOM. We use fiber coupled $LiNbO_3$ electro-optic modulator, manufactured by EO-SPACE, model : AZ-0K5-10-PFU-PFU-780-S (appendix z). More detailed charasteristics of the EOM are given in subsection **4.1.1**. EOM is followed by a polarizer. By applying Gaussian voltage signals from the signal generator to the EOM we were able to create Gaussian polarization pulse in the plane of the polarizer. The polarizer transforms this signal to the Gaussian intensity pulse (see **4.1.2**) The pulse peak power of the Gaussian pulse was 20μW. For the reference pulse, a fraction of the probe pulse was picked by a polarization beam splitter and detected before the vapor cell by an avalanche photodiode (see **4.1.3**) . We used pump with intensity of 200 mW and polarization orthogonal to the probe beam. The waist of the pump and the probe are, as before, 1.05 mm and 0.8 mm, respectively. These two beams intersect at the constant angle of 3 mrad inside the vapor cell. The cell temperature was 120^0C. Probe and conjugate pulses are detected by two PIN photodiodes.

4.1.1 Electro-optic modulator

As mentioned we've used AZ-0K5-10-PFU-PFU-780-S electro-optical modulator manufactured by EO-SPACE (see Apendix B). The modulator has the structure of Mach-Zender interferometer with phase modulator in one branch (section **2.8**). Active medium of the modulator is lithium-niobate ($LiNbO_3$) The crystal is cut along its z axis (z-cut [81]) which also is the axis of light propagation. The refractive index for x and y axis is the same - n_O. Advantage of z-cut crystals is that they are less sensitive to photorefractive effect (the phenomena of changing of index of refraction with temperature ([81])). Namely index of refraction along x and y axes is the same (n_O) and the change of that index with temperature dn_O/dT is also the same so the uncontrolled change of phase between two interferometer branches that originates from fluctuation of index of refraction between these two axes is minimized. In order to measure EOM's characteristics we've set up a simple experimental scheme given in figure 34.

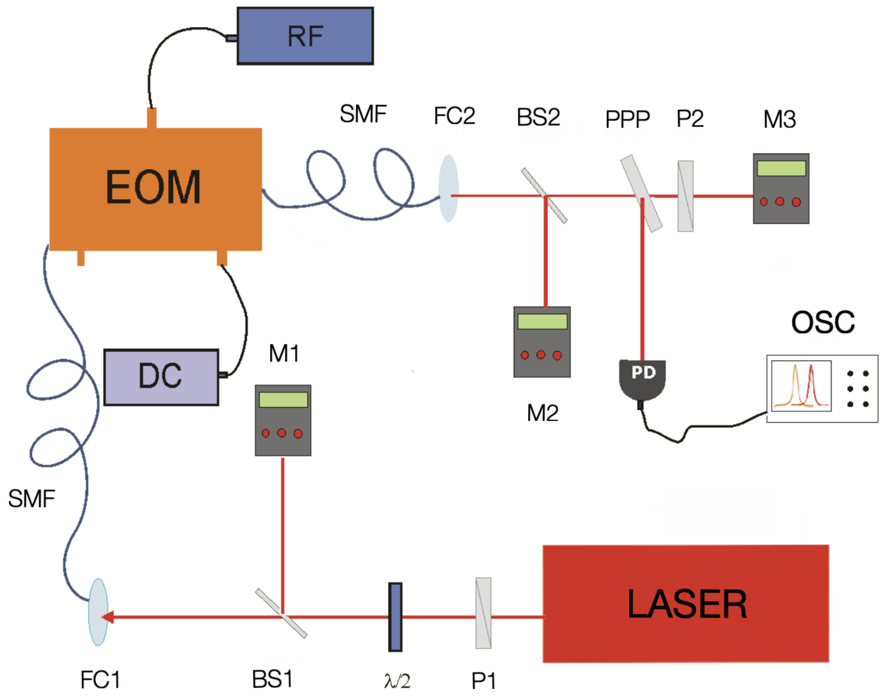

Figure 34: Scheme of experimental setup for EOM characteristics determination. P1, P2 polarizers, BS1, BS2 - beam splitters, M1, M2, M3 - optical power meters $\lambda/2$ - lambda-half wave plate, FC1, FC2 - fiber couplers, SMF - single mode polarization maintaining optical fiber, RF - RF signal generator, DC - DC source, EOM - electro-optic modulator, PD - photo diode, PPP - plan-parallel plate, OSC - oscilloscope.

V_π measurement As mentioned in section **2.8** V_π is the DC voltage that generates a phase shift of π when applied to the EOM. In order to determine this quantity we've measured the dependence between DC voltage applied to the EOM and output laser intensity using scheme presented in figure 34. Experimental results are presented in figure 35.

Theoretically the dependence is given by the squared harmonic function (126) so we've fitted the results with this function. The fit was done using Origin Pro software. We've also presented the results of the fit in table 9.

From the table we see that we've got very good match between theoretical dependence and experimental results as seen from adjusted r-square of 0.9787. The

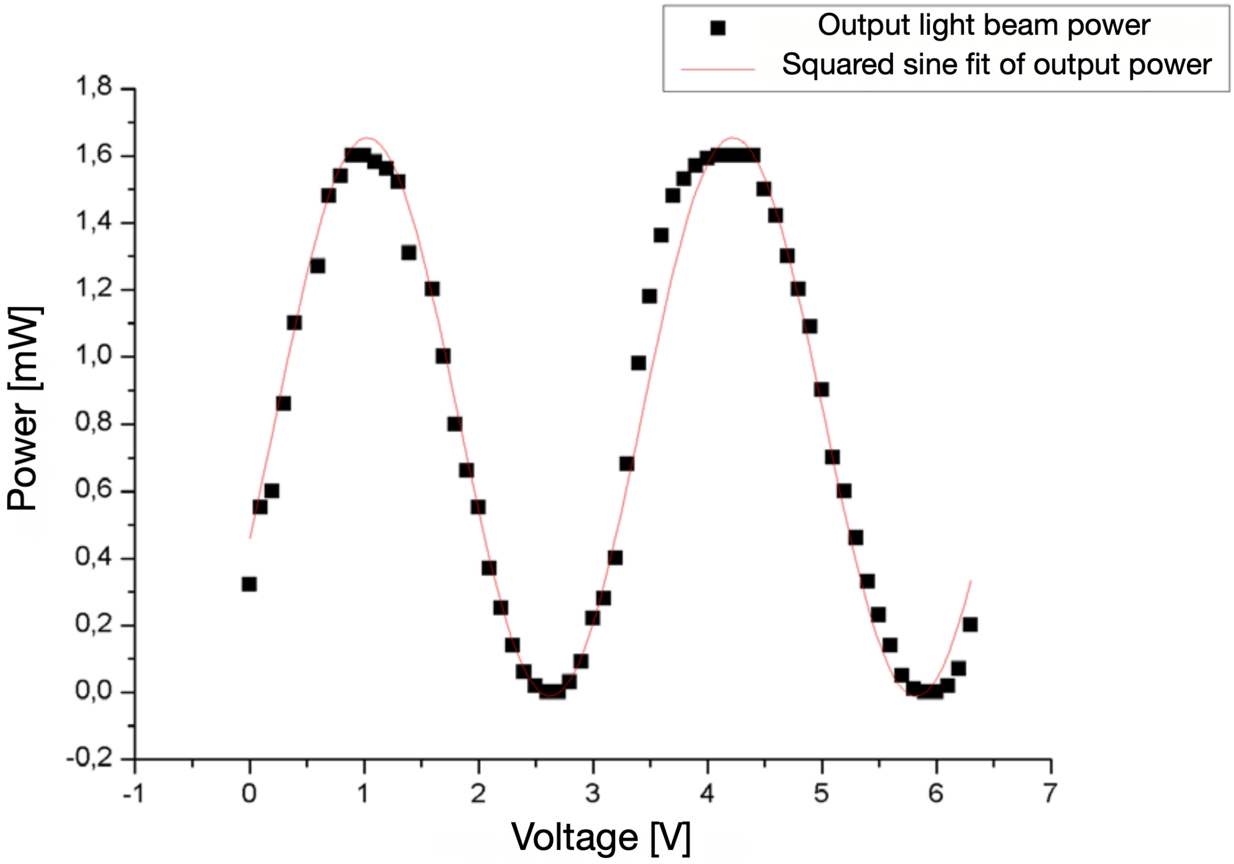

Figure 35: Dependence of EOM output light beam power and DC voltage applied to the EOM

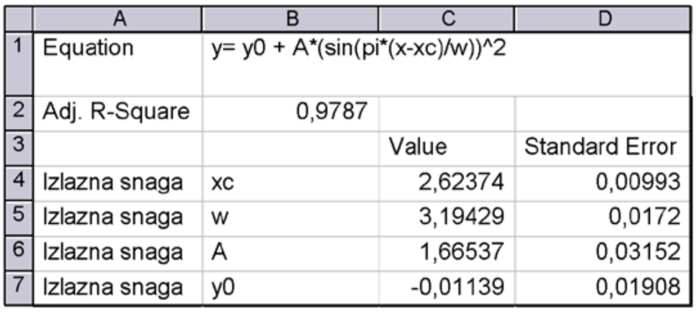

	A	B	C	D
1	Equation	y= y0 + A*(sin(pi*(x-xc)/w))^2		
2	Adj. R-Square	0,9787		
3			Value	Standard Error
4	Izlazna snaga	xc	2,62374	0,00993
5	Izlazna snaga	w	3,19429	0,0172
6	Izlazna snaga	A	1,66537	0,03152
7	Izlazna snaga	y0	-0,01139	0,01908

Table 9: Dependence of EOM output light beam power and DC voltage applied to the EOM

period of the fitted function is the half of the voltage V_π. Then from the table 3 we read the value for V_π:

$$V_\pi = 1.60 \pm 0.02V \tag{139}$$

The measured value deviates from the the value given in the manufacturer's specification by $0.1V$ which underlines the need for this measurement.

The assessment of EOM's speed EOM's speed can in this context be defined as how fast the EOM reacts when a voltage is applied. In other words how fast the index of refraction in the EOM's medium changes when the voltage is applied to its sides. To investigate this we've deployed RF signal generator for fast signal generation and a fast photodiode for measurement (figure 34). The two signals were monitored using an oscilloscope. In figure 36 we can see the results of the measurement with 5 MHz signal.

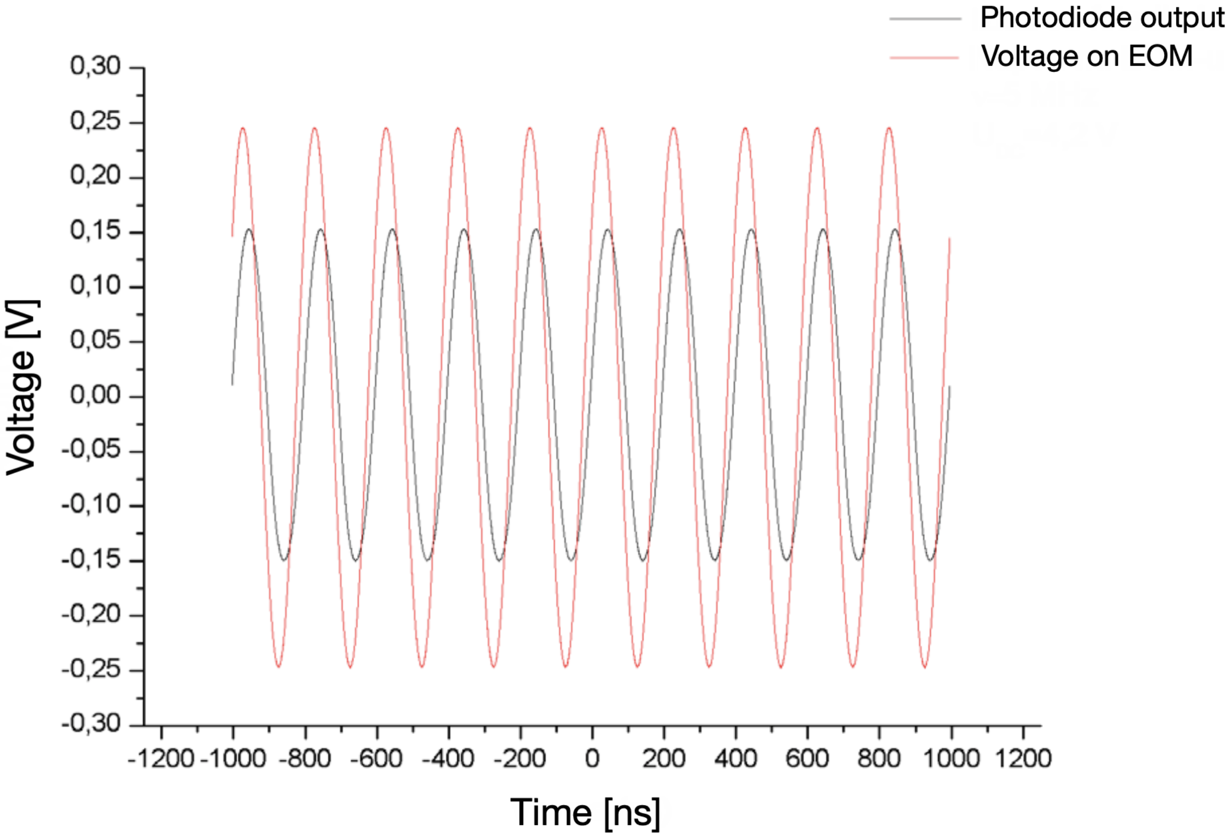

Figure 36: Time dependence of photodiode signal and voltage applied to the EOM. The frequency of the voltage iz 5 MHz

We can notice that there is a delay between the voltage applied to the EOM and the signal picked up by the photodiode. In order to investigate the reasons for this delay we've adjusted the DC voltage on the EOM to achieve zero output intensity and then excited the EOM with single voltage pulse. The results are shown in figure 37.

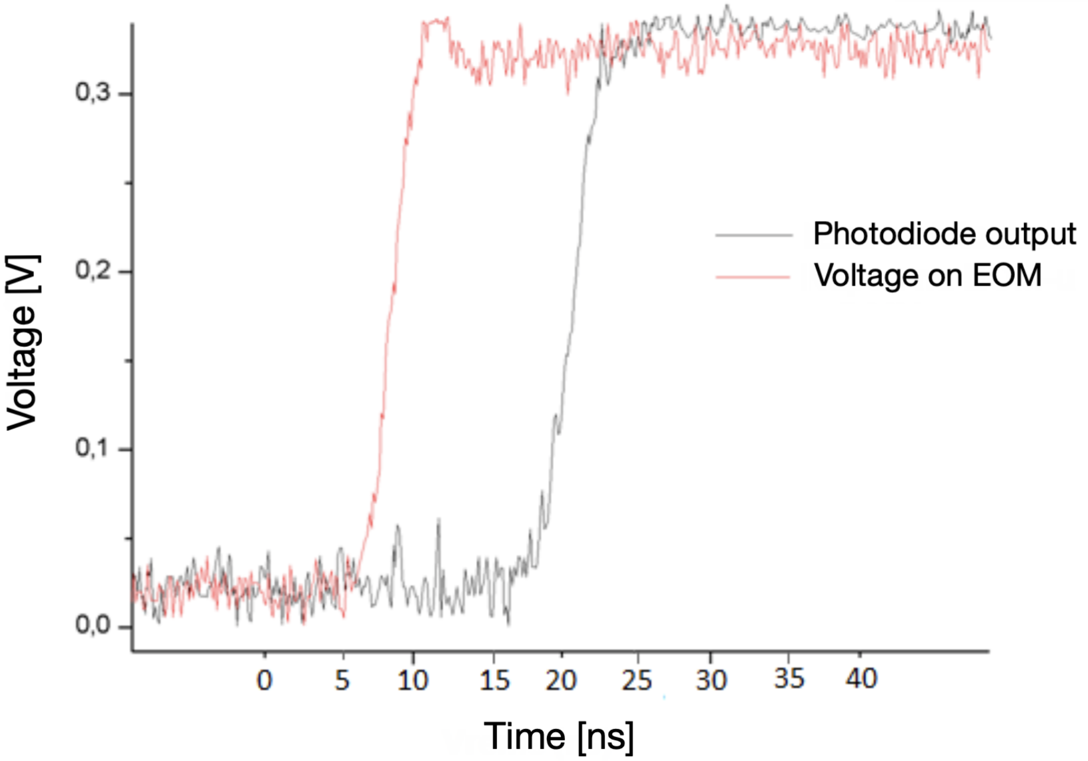

Figure 37: Time dependence of photodiode signal and single voltage pulse applied to the EOM.

First we can see that there is a delay between the beginning of the rise of voltage and photodiode signal. The photodiode signal is late for about 10 ns. This difference is present because of the finite time of signal propagation through cables and BNC connectors (The cable for photodiode signal was around 1.5 meters longer than the cable carrying EOM voltage. Since the speed of signal in the copper wire is around 200000 m/s we have a difference about 7.5 ns between the two signals . We should also account for additional time needed for photodiode signal amplification, filtering, and other electronic manipulation which brings us close to the measured difference of 10ns. It is important to note that this delay isn't caused by the EOM's speed. Next let's observe that there is a difference between the rise time of voltage and photodiode signal of about 1 ns (voltage rise time is 4.2 ns and photodiode signal rise time is 5.2 ns). This difference can be attributed both to the speed of the photodiode (as mentioned the speed of the photodiode is 12 GHz) and to the speed of the EOM. This experimental setup alone isn't sufficient for making this differentiation but since the difference of 1 ns is of the magnitude of experimental error for slow light measurement we haven't further investigated this matter. The conclusions made at this stage were later incorporated for the calibration of slow light measurements (section **4.1.3**)

4.1.2 Generation of short light pulses

As previously mentioned in section **4.1** EOM is used for generation of short light pulses. In order to examine the features of generated short light pulses we again used the setup given in figure 34 with one modification: instead of RF generator we put programmable pulse generator (Metrix GX5000-MoD). This generator is capable of producing rectangle signals with widths down to 5ns and rise times below 1ns. It is also possible to set a pause between the pulses to up to two seconds. Using rectangle signals directly is not suitable for slow light measurements. Voltage rectangle signals would result in light rectangle signals in time-domain. Spectrum of rectangle signals is sinc function which is unbounded in frequency domain ([87]) . Spectral components which are far from the window of high dispersion don't experience slowing and the net effect of this is the broadening (in time domain) of the light pulse which is the unwanted effect. Having light pulses which have Gaussian shape in time domain are a better choice. Fourier transform of Gaussian is also a Gaussian so the spectrum of Gaussian pulses in time are also Gaussian. This spectrum is bounded and we have less of spectral components far from the high dispersion window and hence the broadening is lower.

In order to produce the Gaussian voltage signals from rectangle signals we have used Gaussian filters. Filters were made in the electronics laboratory of the Photonics Center by Milan Minic. Schematics are given in Appendix ZBLJ. Filters are suited for producing Gaussian pulses with 20ns, 40ns, 80ns and 120ns full width half maximum (FWHM) . These signals are then brought to the EOM and used for light modulation. Modulated light was detected by photodiode and analyzed using oscilloscope. An example of modulated light pulse and its Gaussian fit are presented in figure 38.

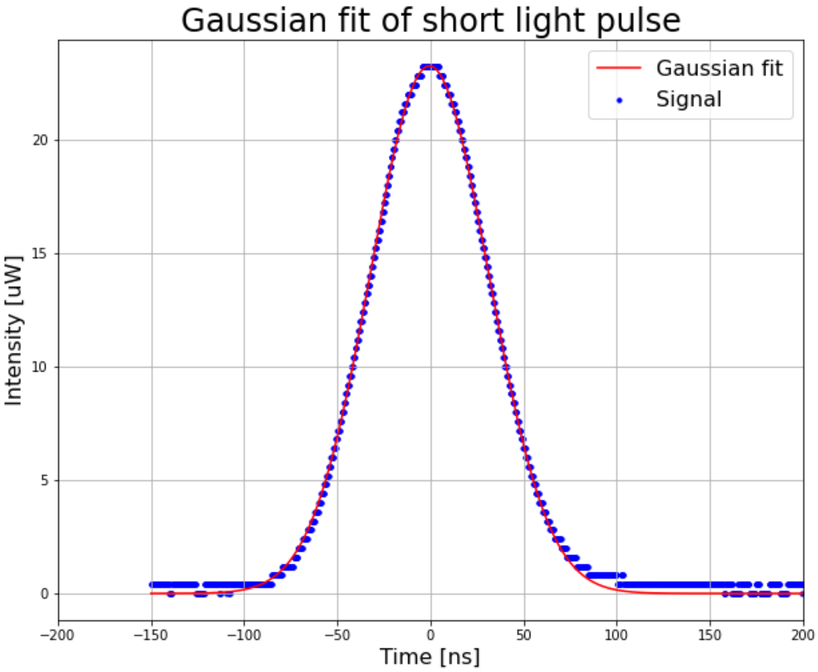

Figure 38: Gaussian fit and the light pulse modulated by Gaussian voltage signal. Signal (blue dots) was averaged over 500 samples. Gaussian fit is given in red.

In order to check whether the modulated light pulses have Gaussian form we've performed Gaussian fit using LMFIT library for Python ([88]). Results are presented in table 10.

```
[[Model]]
    Model(gaussian)
[[Fit Statistics]]
    # fitting method   = leastsq
    # function evals   = 17
    # data points      = 2500
    # variables        = 3
    chi-square         = 257.130379
    reduced chi-square = 0.10297572
    Akaike info crit   = -5680.15686
    Bayesian info crit = -5662.68472
[[Variables]]
    amplitude:  1849.70631 +/- 1.86466378 (0.10%) (init = 2568.24)
    center:    -0.54906486 +/- 0.03695798 (6.73%) (init = -0.9)
    sigma:      31.7498851 +/- 0.03695798 (0.12%) (init = 36.9)
    fwhm:       74.7652644 +/- 0.08702939 (0.12%) == '2.3548200*sigma'
    height:     23.2418508 +/- 0.02342976 (0.10%) == '0.3989423*amplitude/max(1e-15, sigma)'
[[Correlations]] (unreported correlations are < 0.250)
    C(amplitude, sigma) = 0.577
```

Table 10: Statistics for Gaussian fit of the light signal modulated with Gaussian voltage signal

Looking at the chi-square statistics and the confidence levels of Gaussian function parameters we can see that the fit is excellent and we can regard our light pulses as Gaussian in time. We also see that the FWHM of the fit is 75ns and we will use this value as our FWHM of light pulse.

Gaussian fits for 20ns, 40ns and 120ns were also performed and the results were equally good and due to similarity are not presented here.

4.1.3 Detection

Analog to the CW case we now have three type of pulses; reference, amplified probe and newly generated conjugate pulses. These pulses were detected by an avalanche and two PIN photo diodes, respectively. Due to very low intensity of the reference pulses we've used Si avalanche photo diode (APD) Hamamatsu S12023-10 for its detection. The APD was biased with 160 V which provided the gain of 100 and the bandwidth of 600 MHz. For amplified probe and conjugate pulses, two identical Si PIN photodiodes Hamamatsu S5973-02 were used. The Si PIN photodiodes were biased with 9 V providing the bandwidth of 1.4 GHz. In all cases the photo current was fed to 50Ω load and DC coupled to the oscilloscope. Each photodiode had enough bandwidth for detection of pulses in the duration range 20-120 ns that was used in the experiment.

4.2 Results and discussion

4.2.1 Definition of measured quantities and the initial delay

In this subsection we will define quantities which are important in the context of slowed light pulses.

In order to quantify the effects of the dispersion medium on light pulses we need to have a reference light pulse. The reference pulse represents the behavior of light pulse without the medium and, as its name suggests, gives a reference against which the effects of amplifying medium are measured. As already mentioned in **4.1** this is achieved by picking a fraction of the probe pulse at the 50:50 polarization beam splitter before the vapor cell. In this way the probe and the reference pulse have the same shape in time. Also by picking the half of the probe beam we also have the intensity reference that would help us quantify the amplification effects of the FWM medium.

As in the CW case we have the notion of the gain which is the measure of probe and conjugate amplification. In this case the gain is defined as ratio of probe or conjugate peak intensities and reference peak intensity:

$$G_p = \frac{I_p}{I_r} \tag{140}$$

$$G_c = \frac{I_c}{I_r} \tag{141}$$

where G_p and G_c stand for the probe and the conjugate gain respectively and I_p, I_c and I_r stand for probe, conjugate and reference peak intensity respectively.

The main quantities that describe slowing of optical pulses are the fractional delay and the fractional broadening.

Fractional delay is defined as the ratio between absolute delay, which is the time difference between the probe (or the conjugate) peak and reference peak, and refer-

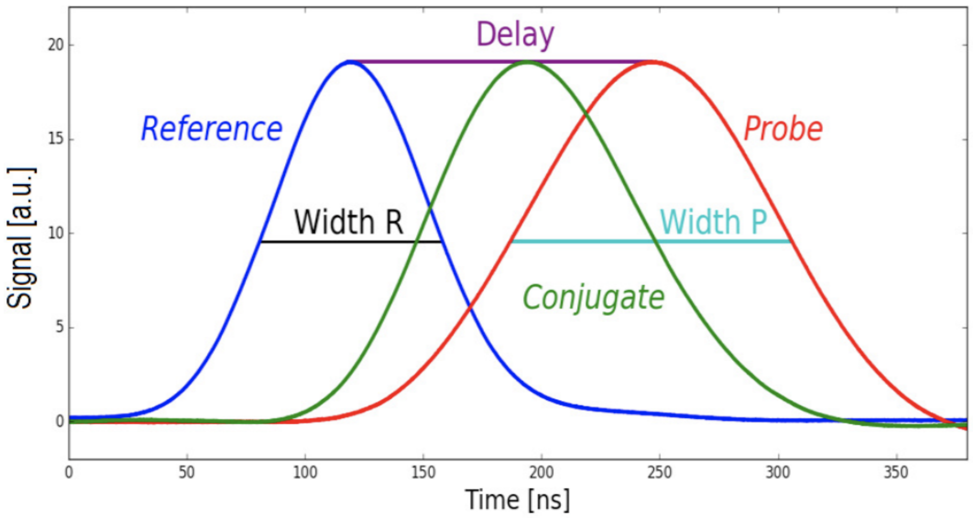

Figure 39: The appearance of typical pulses order and basic definitions.

ence pulse width. If we take a look at figure 48 that would be the ratio between the 'Delay' and the 'Width R'. Fractional delay gives us information about the delay of the light pulse normalized to the width of the reference pulse and should be as large as possible. Likewise, fractional broadening is defined as the ratio of the probe (or the conjugate) pulse width to the reference pulse width, ratio of 'Width P' and 'Width R' in figure 48. This parameter is informative about the broadening of the slowed light pulse and should be as close as possible to one.

To represent the real situation in the experiment the definition of absolute (and consequently fractional) delay has to be modified. As mentioned previously the reference beam is detected before the vapor cell. To have a proper reference we need to take into account the longer path traversed by the probe and conjugate before the detection and the effects of additional beam splitters and vapor cell windows. Also as mentioned in **4.1.1** different lengths of cables and type of connectors can introduce additional delays. To remedy these effects we've measured the **initial delay** between the reference and the pulse probe by measuring the delay between the two pulses with vapor cell on room temperature. On room temperature the concentration of potassium atoms is so small that the effects of FWM are negligible and can be regarded as non existent. So in this conditions we can measure the amount of delay unrelated to the effects of dispersion medium (figure 40).

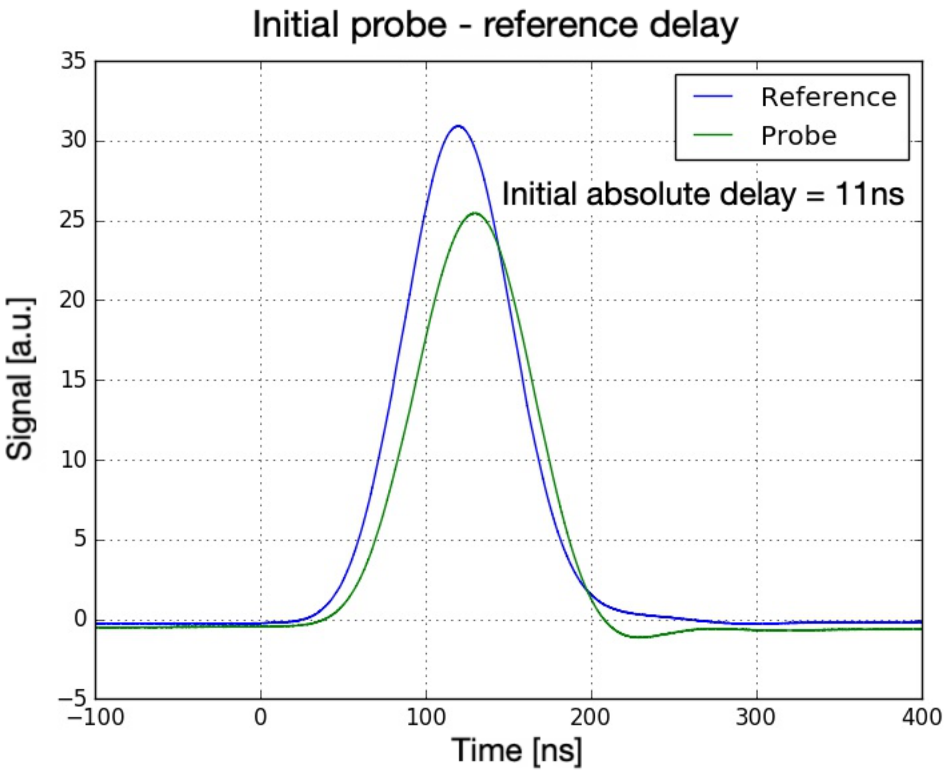

Figure 40: Measurement of the initial absolute delay between the probe and the reference pulse

Initial absolute delay between the probe and the reference is 11ns. This amount of initial delay is present in all the following measurements of the delay and is subtracted in all results so we could quantify the effects of FWM medium only.

4.2.2 Results

Typical measurements for input pulse duration of 120 ns and 20 ns for delayed amplified probe and conjugate pulses are shown in figure 41 a) and b). These pulse durations are extremal in our case and illustrate the fastest and the slowest signal intensity variation in the experiment. Due to similarity we are not showing typical measurements for 40ns and 80ns pulses.

Let's look at the results more closely. In figure 41 a) we have presented the slowing of 120ns wide reference pulse. Results were obtained by averaging 1000 measurements. Here the one-photon detuning was set to $\Delta = 1$ GHz and two photon detuning was kept at resonance, $\delta = 0$ MHz. We've also normalized all the

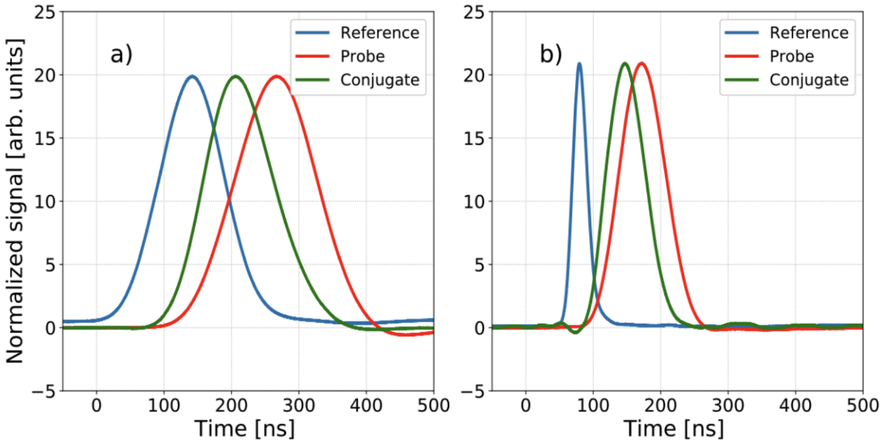

Figure 41: Example of the slowing of optical pulses by FWM in K vapor. Conjugate and probe are Gaussian. The waveforms are obtained upon 1000 averaged measurements and the peaks are normalized. (a) τ = 120 ns, δ = 0 MHz, Δ = 1 GHz (b) τ = 20 ns, δ= 0 MHz, Δ = 0.7 GHz. Other parameters were kept constant for both measurements: T = 120^oC, Δ = 1 GHz, I_{pump} = 200 mW, I_{ref} = 20μW, Θ = 3mrad. Picture taken from [75]

signals so their time characteristics would become more visible. In this particular example we have observed amplified probe and conjugate pulse, both with Gaussian shape. The gain of the probe pulse was 16 and the measured absolute delay was 124 ns. This gives fractional delay of 1.1 and the fractional broadening was 1.2. The conjugate pulse had fractional delay of 0.56 and fractional broadening of 1.05 respectively. The emergence of the peak of the conjugate pulse before the peak of the amplified probe was also observed in rubidium ([69]) and sodium ([74]) was confirmed by this measurements for the case of potassium as well.

In figure 41 b) the typical measurement for the 20ns pulse is shown. Now the photon detuning was set to Δ = 700 MHz and two photon detuning was again at resonance δ = 0 MHz. The shapes of amplified probe and newly created conjugate pulse were again Gaussian. Like in the 120ns pulse case the conjugate pulse had smaller absolute delay than the amplified probe pulse. The gain of amplified probe was 14.5, while fractional delay and fractional broadening were 3.7 and 3.2 respectively. For conjugate we have measured 10 for the gain and 2.7, 2,7 for fractional delay and fractional broadening respectively. It should be noted that the separation between probe and conjugate at the exit of the cell can be tuned by choosing different experimental parameters.

The Gaussian shape of the exiting pulses is not always retained (figure 42). For some choice of parameters pulses become distorted and the measurements of pulse width, delay and broadening become impossible. According to [69] the distortion of the waveform could come from complex dynamics of the interplay between parametric amplification and Raman absorption. Balance between losses and gains of probe pulse are critical for temporal shapes of probe and conjugate pulses, which means that the range of δ in which we would retain Gaussian shape of the pulses will be different for different Δ and for different potassium densities. Also, note that the gain of the amplified probe pulse in figure 42 is around 0.9 which is very low in potassium. Due to small leakage of the light through the EOM and parasitic differentiation of the signal in the detection and acquisition circuits the false undershoot at the times larger than 320 ns (figure 42)) becomes visible since it is magnified in the normalization procedure.

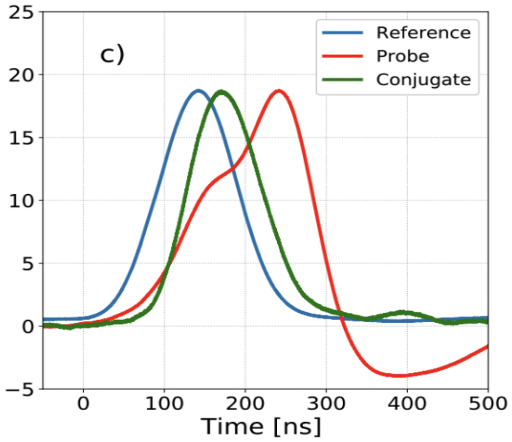

Figure 42: Example of the slowing of optical pulses by FWM in K vapor. Gaussian shape of probe and conjugate is lost.The waveforms are obtained upon 1000 averaged measurements and the peaks are normalized. τ = 120ns, δ = -4 MHz, Δ = 1 GHz, T = 120^oC, Δ = 1 GHz, I_{pump} = 200 mW, I_{ref} = 20μW, Θ = 3mrad.Picture taken from [75]

In order to investigate the influence of two-photon detuning we've scanned δ from -20 MHz to 10 MHz with the step of 2 MHz for all of our measurements (figure 43). In general for the values of δ on the edges of this range the pulse profile becomes distorted and loses its Gaussian shape.This is the already mentioned case where quantities of interest cannot be measured (figure 43 for δ = -10, 4 and 6 MHz).

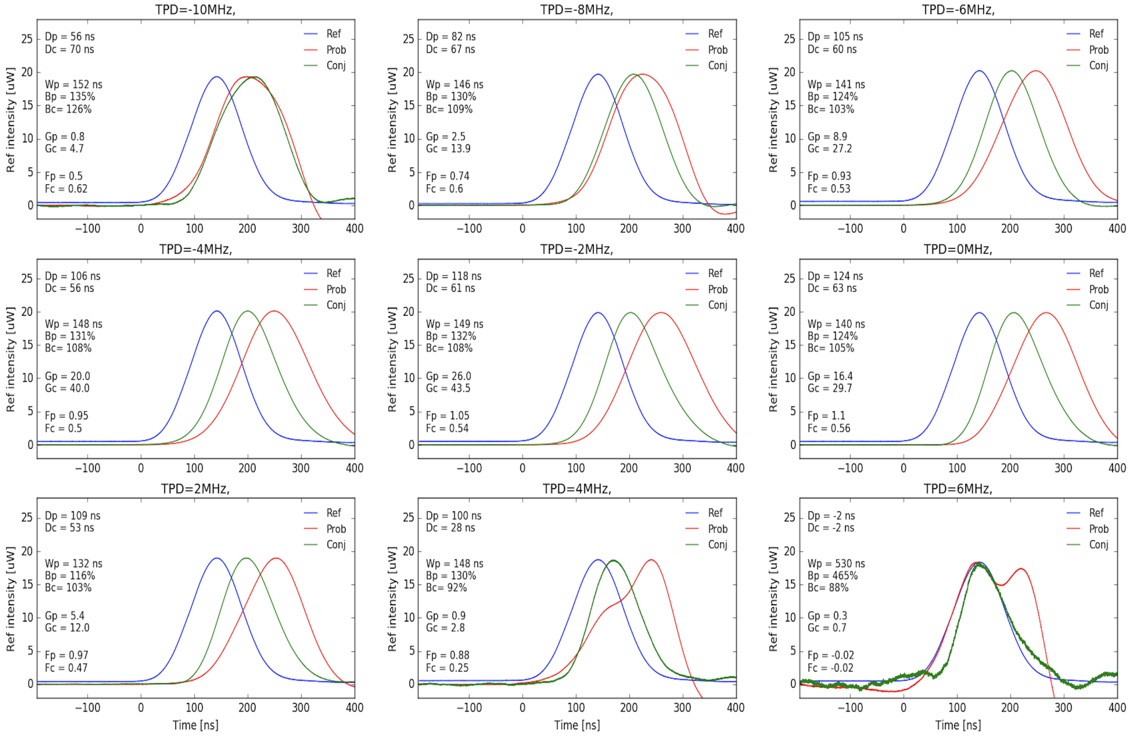

Figure 43: Varying two-photon detuning δ. As before the waveforms are obtained upon 1000 averaged measurements and the peaks are normalized. The following information is provided on the graphs: $\mathrm{D_p}$ - probe delay, $\mathrm{D_c}$ - conjugate delay, $\mathrm{W_p}$ - probe FWHM, $\mathrm{B_p}$ - probe broadening, $\mathrm{B_c}$ - conjugate broadening, $\mathrm{G_p}$ - probe gain, $\mathrm{G_c}$ - conjugate gain, $\mathrm{F_p}$ - probe fraction delay, $\mathrm{F_c}$ - conjugate fractional delay. Constant parameters: τ = 120 ns, Δ = 1 GHz, T = 120^oC, I_{pump} = 200 mW, I_{ref} = 20μW, Θ = 3mrad.

In order to have a better overview we have plotted the dependence of fractional broadening, fractional delay and gain for probe and conjugate pulse as a function of δ for Δ = 1 GHz.(figure 44)

The dependence of fractional broadening and fractional delay is nearly constant in the interval of two-photon detuning for which we have nonzero gain. The best trade-off between fractional delay and fractional delay was achieved at δ = 0 where we had the fractional delay of 1.1 and fractional broadening of 1.2. The gain at this δ is 16 which is close to a half of maximum gain of 26 (achieved for δ = 2 MHz) for this choice of experimental parameters. Our results are qualitatively different in comparison with results obtained in rubidium [69] and sodium [74]. In the case of

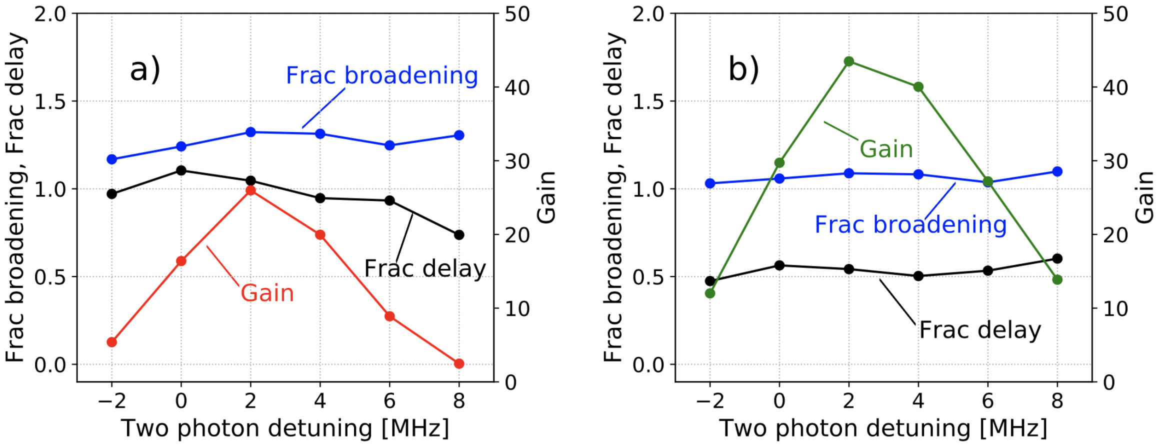

Figure 44: Fractional delay, fractional broadening and gain dependence on δ for (a) amplified probe (b) conjugate. Parameters: τ = 120 ns, Δ = 1 GHz, T = 120^oC, I_{pump} = 200 mW, I_{ref} = 20μW, Θ = 3mrad. Picture taken from [75]

rubidium the delay is also largest in the vicinity of the bare state 2-photon resonance. The difference is that dependence between delay and two-photon detuning is sharp and the delay drops down quickly as the δ moves away from resonance. In the case of sodium although the dependence of fractional delay and fractional broadening on pump Rabi frequency (i.e. intensity) is not depicted in [74] we can still conclude that the gain and the delay are in trade-off relation in Na since both gain and delay are monotonic functions of pump Rabi frequency. In other words, for sodium vapor one can say that higher the gain, smaller the delay and and vice versa while in potassium we do not see such strong dependence of delay (or broadening) on gain. This difference might arise from the fact that potassium, unlike rubidium and sodium, has smaller hyperfine splitting than the Doppler width and hence the condition, set in [69], Δ+ HFS $\gg \Delta$ is not fulfilled in the case of potassium.

We have systematically presented the results of slowed optical pulses in alkali vapors investigated so far in table 11. We conclude that the results in potassium are better or comparable to those in rubidium and sodium for similar experimental conditions and similar length of the optical pulses.

If the information is carried by a train of optical pulses it becomes apparent that the amount of information transferred in time would be higher if we would have shorter optical pulses. So it favorable to transfer information with the short-

Medium	Rb	Na	K
Reference pulsewidth [ns]	70	109	120
Gain	13	28	16
Fractional delay	0.57	1.03	1.1
Fractional broadening	-	1.12	1.2

Table 11: Summary of the results for slowing of short optical pulses via FWM in Rb, Na and K. Table taken from [75].

est possible optical pulses while retaining large fractional delays accompanied with small fractional broadening. In order to find the shortest input pulse duration with those characteristics, we have performed the measurements of fractional delay and fractional broadening for different pulse durations (figure 45).

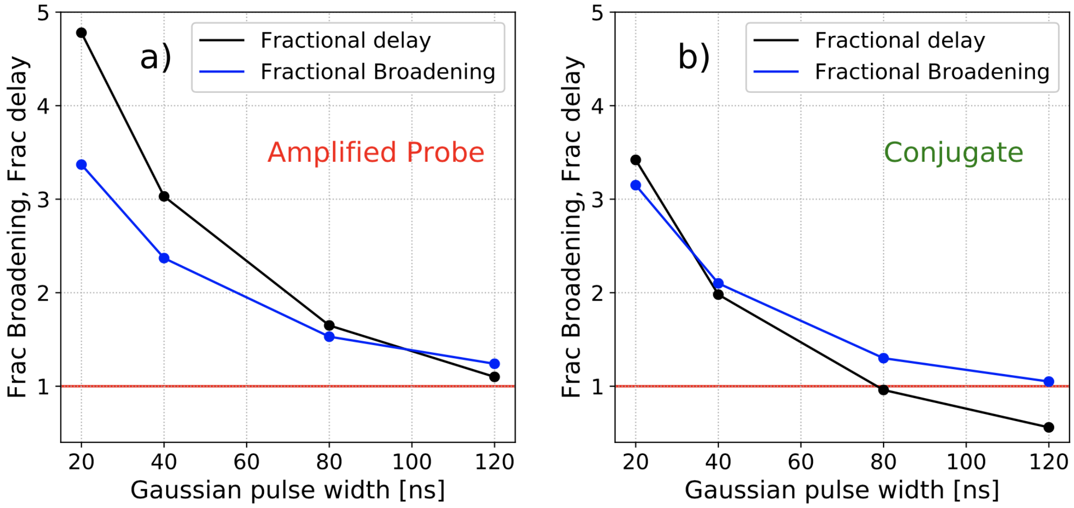

Figure 45: Dependence of fractional broadening and fractional delay on incident pulse duration in slow light process via FWM in K vapor for (a) amplified probe (b) conjugate pulses. Parameters: $\delta = 0$ MHz, $\Delta = 1$ GHz, T = 120^oC, $I_{pump} = 200$ mW, $I_{ref} = 20\mu$W, $\Theta = 3$mrad. The red line represents the value with no broadening. Picture taken from [75].

As seen from figure 45 we've performed measurements with 20ns, 40ns, 80 ns and 120ns Gaussian pulses. In general, for shorter light pulses we observe that fractional delay and fractional broadening are increase simultaneously. The broadening of the pulses with shortening of their duration can be understood in the following way ([89]). The shorter pulses in time domain are wider in the frequency domain i.e. they are spectrally broader. Because of this fact larger number of Fourier components of the optical pulse get slowed down differently (due to the dispersive medium and the fact that refractive index varies with frequency) which manifests as broadening in time domain. An alternative explanation can be given using equations for group velocity and group delay given in [90] characterizing the slow light effect related to the EIT effect. The group delay is linearly proportional to optical depth and inversely proportional to the (EIT) control (the probe in our case) intensity. Since the latter two parameters are fixed when the the pulse duration is decreased, the group delay should be fixed and thus the fractional broadening will increase when decreasing input pulse duration.

As already mentioned one of the possible applications of slow light would be in optical delay lines - devices capable of producing arbitrary delays of optical signals. For this application it is necessary that the fractional delay is one or higher. In this sense the pulse duration of 120 ns has the best performances in terms of delay and broadening (figure. 45). We see that for this pulse duration we have only about 20% of widening while the fractional delay is above one which makes the pulse duration of 120 ns best suited for usage in potassium medium.

One of the more important parameters in this research is the pump intensity used in the experiment. It is favorable to use the smallest possible pump intensity for the achievement of the wanted slow light properties. Apart from energy consumption reduction when using lower pump intensities low intensities are desirable from perspective of using other, less expensive, types of lasers. To that end we've measured the dependence of fractional delay and fractional broadening on pump intensity (figure 46). All of the other parameters were kept constant.

We see that unlike in sodium vapor ([74]) fractional delay and fractional broadening in our case don't depend strongly on the pump intensity, although the trend is the

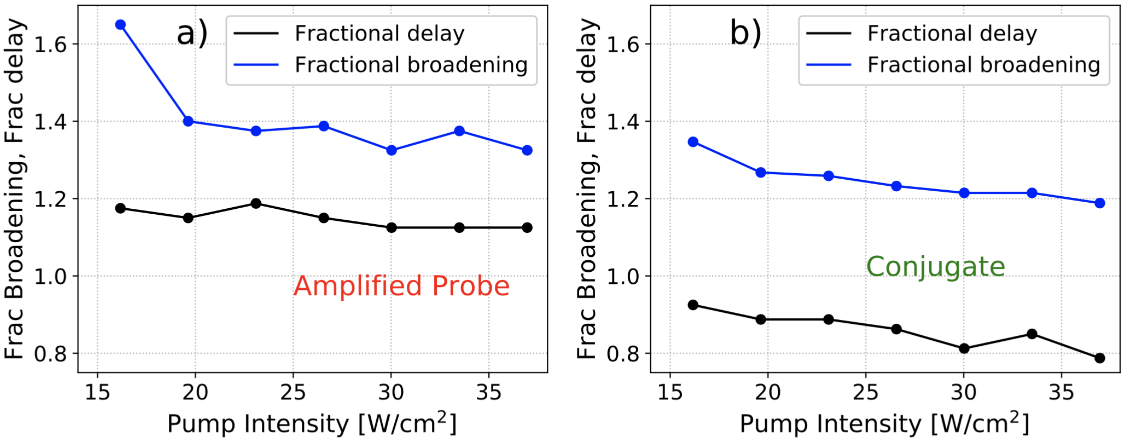

Figure 46: Dependence of fractional broadening and fractional delay on pump intensity in slow light process via FWM in K vapor for (a) amplified probe (b) conjugate pulses. Parameters: τ = 80ns, δ = 4 MHz, Δ = 1.3 GHz, T = 120^oC, I_{ref} = 20μW, Θ = 3mrad. Picture taken from [75]

same: fractional delay and fractional broadening decrease as the pump intensity increases. We also have a very good performance in the sense of ratio between the fractional delay and fractional broadening over wide range of pump intensities. Intensities for which we still have good values of fractional delay and fractional broadening are achievable with diode lasers which opens the door for usage of this types of lasers in this kind of research.

The measured dependencies on two-photon detuning and the pump intensity are rather modest to almost uniform(figures 44 and 46). These dependencies are in contrast to those measured in cases of rubidium ([69]) and sodium ([74]). Rubidium and sodium are very similar quantum systems with similar fine and hyperfine structures and quantum numbers associated. Also the experimental conditions are almost the same (geometry, laser intensities, temperatures, etc). We conclude that the smallest ground state hyperfine splitting among all stable isotopes of alkalis that we have for ^{39}K and a large Doppler broadening that is approximately as twice as large as the hyperfine splitting at our experimental temperatures (rubidium and sodium have larger hyperfine splittings than Doppler widths) are behind the reason of the discrepancy in the results found in these works. However there is a need for development of detailed theoretical models for light propagation in hot potassium vapor which would take into account all the specifics of potassium like aforementioned ground state hyperfine splitting, Doppler broadening at exact experimental temperatures, dipole matrix elements and so on. One should also take care with approximations used in the model since they could be valid for one type of atoms but not for other.

5 Conclusion

The research presented in this thesis was set out to explore the possibility of achieving and describing an optical four-wave mixing in hot potassium vapor, and slowing of short light pulses using this phenomena. To that end we have assembled the experimental setup which could both be used for saturation spectroscopy and observing four-wave mixing with co-propagating pump and probe beams. Saturation spectroscopy was used for identification of potassium spectroscopic lines, frequency calibration of the laser and for determining the frequency drift of the laser. We have also build the heating system for the potassium cell based on hot air and equipped with temperature control system. For fine frequency scanning we've deployed acoustooptic modulator in double-pass configuration.

Using this setup we were able to observe non-degenerate FWM in hot potassium vapor at the D1 line using co-propagating pump and probe beams and a double-Λ coupling scheme. To the best of our knowledge this is the first observation of this phenomena in potassium vapor. After the initial successful observation we've proceeded with the investigation of parameters space in search of best possible efficiency of the FWM process. The efficiency is measured by the amplification or the gain of the amplified probe and the newly created conjugate beam.

First we've investigated the influence of two-photon detuning δ for four different one-photon detunings Δ (400 MHz, 700 MHz, 1000 MHz and 1300MHz) with all the other experimental parameters kept constant. Theoretical and experimental works in other metallic vapors indicated that a small δ is needed to compensate AC-Stark light shift. We've confirmed this in the case of potassium as well by observing maximum gains at non-zero values of δ. It is also suggested that the AC-Stark light shift decreases with one-photon detuning Δ which was also experimentally observed by the smaller δ needed for achieving maximal gain at larger Δ.

The influence of one-photon detuning can be seen through prism of two competing processes. One being the FWM which efficiency increases when we are closer to the one-photon resonance ie when Δ decreases. Second being one photon absorption which also increases with increasing Δ. The best trade-off is found on the edge of Doppler profile at $\Delta = 700$ MHz. At this one-photon detuning and for $\delta =$ -6 MHz (with pump power $P_0 = 400$ mW, probe seed power $P_{in} = 200\ \mu$W, vapor temperature $T = 120°C$ ($\approx 3 \times 10^{12}$ atoms/cm^3), angle between the pump and the probe $\phi = 3$ mrad) we've found the highest gain of the conjugate beam $G_c = 82$ (The probe gain for the same parameters was $G_p = 58$). This is one of the largest gains achieved in alkali vapors.

We've also explored the influence of temperature on the FWM efficiency. With raising temperature the concentration of atoms in the vapor also raises which leads to the increase of FWM cross-susceptibilities χ_{cp} and χ_{pc}. On the other hand, large susceptibilities lead to large values of the refractive index and its transverse gradient that cause beam self-focusing and beam filamentation which hinders the correct measurement of the beams intensities. In our work we have determined the maximal temperatures for which the measurement is possible for wide range of one-photon detunings Δ (500 MHz, 750 MHz, 1000 MHz, 1500 MHz, 2000 MHz, 2500MHz). We've showed that the maximal temperature in this sense is directly proportional to the one-photon detuning which is in accordance to the fact that dispersion and one-photon detuning are inversely proportional. For the values of $T = 140°C$ and $\Delta = 1500$ MHz we've found the highest probe gain $G_p = 63$ ($G_c = 69$ for the same set of parameters)

Lastly we've investigated the FWM efficiency versus the angle between the pump and the probe beam and versus the pump intensity. Unlike in other alkali vapors we've found that dependence of the probe and the conjugate gain on the angle between the pump and the probe is monotonically decreasing. On the other side the measured dependence on the pump power was monotonically increasing as expected. The lowest pump power at which we were able to detect the conjugate beam was around 100 mW. This laser power is achievable with (cheaper and easily maintainable) diode lasers which opens the possibilities of using them in this kind of research. We were also able to measure even higher gains (96 for the conjugate, 73 for the probe) at pump powers over 500 W but due to the unstable operation of the laser at this power we were not confident enough about the accuracy of our measurement. Nevertheless this indicates that further improvements could be made with using stronger pump powers.

The observation the optical FWM in potassium vapor might be significant in multiple ways. High gains obtained indicate large amount of relative intensity squeezing which is needed for precise spectroscopic sub-shot-noise measurements. The existence of relative intensity squeezing is the necessary condition for the existence of entanglement between the pump and the probe photons. High gains are also directly proportional to the amount of the entanglement which could make potassium vapor one of the best sources of continuous entangled light. High nonlinearities are followed by large dispersion which is responsible for the another important phenomena in photonics - slow light. Slow light was the subject of the second part of the research presented in this thesis.

For the investigation of slowing of short light pulses in hot potassium vapor the experimental setup was modified by the introduction of electro-optic modulator. After detailed examination of EOMs characteristics the EOM was deployed for the purpose of creating the Gaussian light pulses of the following length - 20ns, 40ns, 80ns and 120ns. The aim of the research was to determine the influence of different experimental parameters to the slowing of short light pulses and in the same time to find the values of these parameters at which we would have the optimal trade-off between the fractional delay and the fractional broadening.

First we've investigated the influence of two-photon detuning δ while keeping the other parameters constant. Short light pulses kept their Gaussian profile only in the narrow interval around the two-photon resonance (in the order of few tens of MHz). Outside this interval the Gaussian shape was lost and the measurement of the pulse delay and width became impossible. The distortion of the waveform could come from complex dynamics of the interplay between parametric amplification and Raman absorption. Also the balance between losses and gains of probe pulse is important for temporal shapes of light pulses, which means that the precise range of δ in which we have Gaussian shape of the pulses depends on one-photon detuning, temperature (density) and pump intensity which we've also observed. Due to the fact that the probe pulse experiences higher dispersion this pulse is more slowed than the conjugate pulse. As a consequence the probe pulse experiences larger spectral broadening than the conjugate pulse. Unlike in other alkali vapors the dependence of fractional broadening and fractional delay on two-photon detuning is rather flat. The difference might stem from the fact that in potassium, unlike the other investigated alkalis, the ground state hyper fine splitting is smaller than the Doppler width so the condition Δ+HFS $\gg \Delta$ set in the seminal paper [16] is not fulfilled. Additional theoretical work should be done in order to understand this behaviour clearly.

The best trade-off between the fractional delay and fractional broadening was found for the following parameters: $\delta = 0$ MHz, $\tau = 120$ ns, $\Delta = 1$ GHz, T = 120^oC, $I_{pump} = 200$ mW, $I_{ref} = 20\mu$W, $\Theta = 3$mrad. We've measured the fractional delay of 1.1 with fractional broadening of 1.2. The probe gain was 16. This result is better than measurements performed in rubidium vapor and comparable to those achieved in sodium vapor.

Next we've performed the measurements for several different pulse lengths - 20ns, 40ns, 80ns and 120ns. In general the fractional delay and the fractional broadening increase with shortening of the temporal length of the light pulse. The shorter pulses in time domain are wider in the frequency domain so the larger number of Fourier components of the optical pulse get slowed down by different amount which leads to broadening in time domain. From the perspective of transfer of information by light and optical delay lines specifically, time broadening is an unwanted effect. In that sense the pulse length of 120ns proved to be the best choice since there is only about 20% of widening while the fractional delay is above one.

Finally the influence of pump intensity was also studied. Again contrary to the case of rubidium and sodium we've obtained weak dependencies of fractional delay and fractional broadening on the pump intensity although the trend is the same - they decrease together with decreasing pump intensity. This result again shows that it is possible to investigate these kind of effects using conventional, less expensive and less power consuming diode lasers.

In our work we have proved that hot potassium vapor is an interesting medium for non-linear and quantum optical research. High gains achieved in our measurements indicate the possibility of generating relative intensity squeezed light with high amount of squeezing. This could give way to high precision, below standard quantum noise spectroscopic measurements around D1 and D2 lines of potassium.

Secondly the existence relative intensity squeezed light is a necessary condition for existence of quantum entangled light. Entangled light is a resource for the very promising field of quantum informatics and sources of continuous entangled light are becoming more important due to their robustness, smaller price and lesser complexity than the sources of entangled single photons. In that sense the next step is the creation and research of continuous light created by FWM in potassium vapor.

Also the very good results of slowed light pulses achieved in potassium indicate that the future theoretical insights about the core mechanism of this improved performance could lead to new ways of generating slow light. Slowing systems with gains are important for qubits manipulation and this work highlights hot potassium vapor as medium of choice for this application.

A The heating system

A.1 Aluminium potassium vapor cell carrier

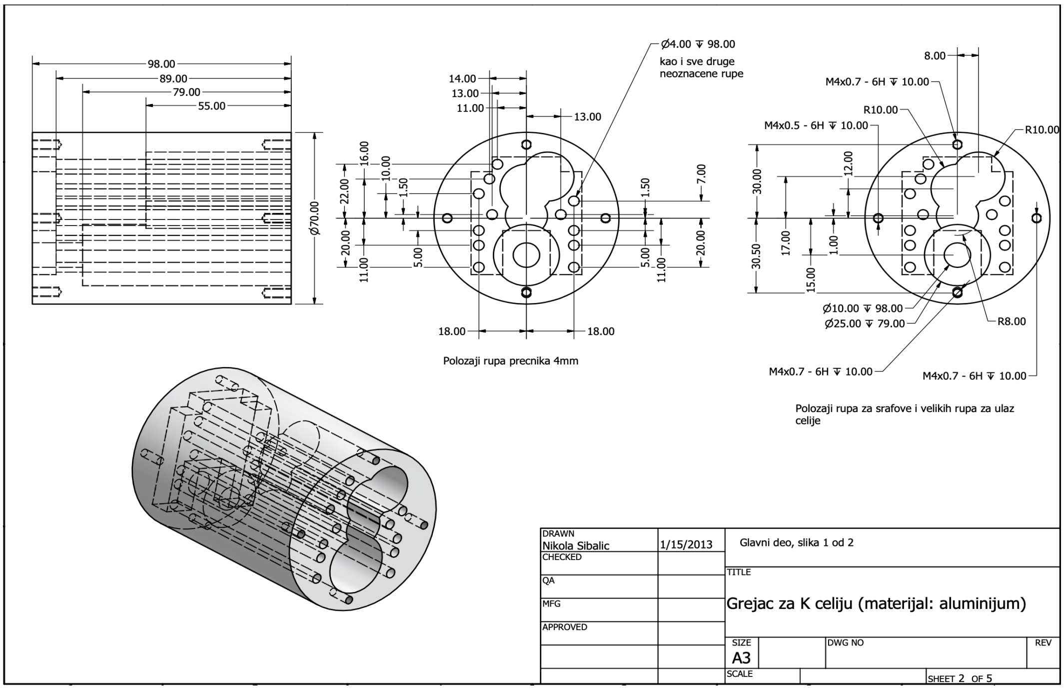

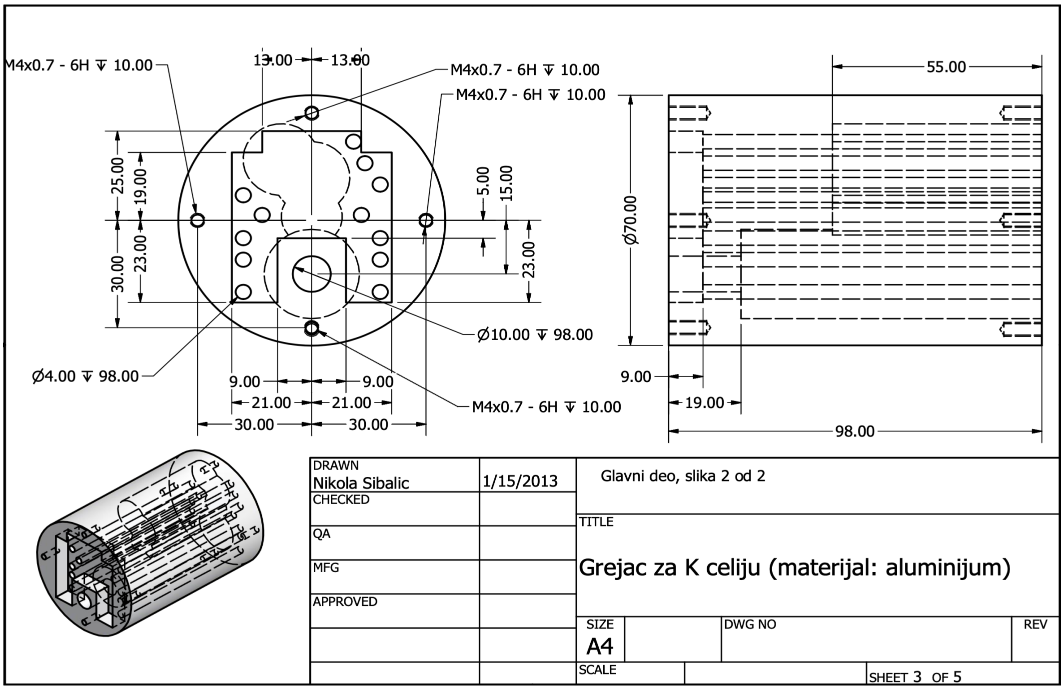

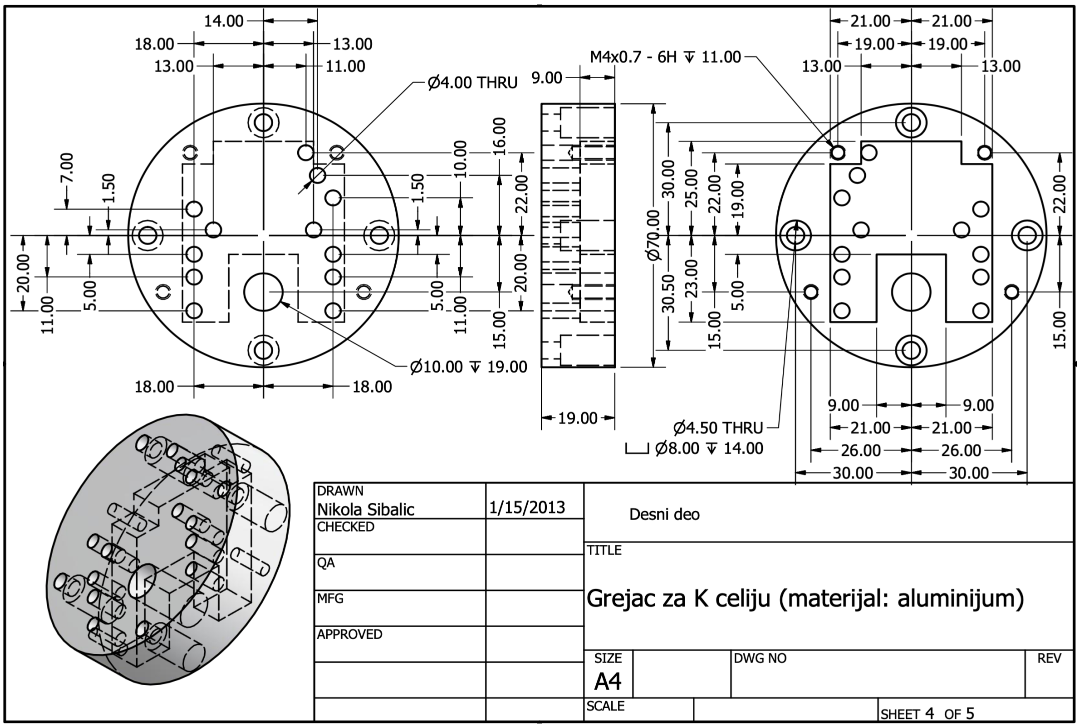

DRAWN
Nikola Sibalic 1/15/2013
CHECKED
QA
MFG
APPROVED

Desni deo

TITLE
Grejac za K celiju (materijal: aluminijum)

SIZE A4
DWG NO
REV
SCALE
SHEET 4 OF 5

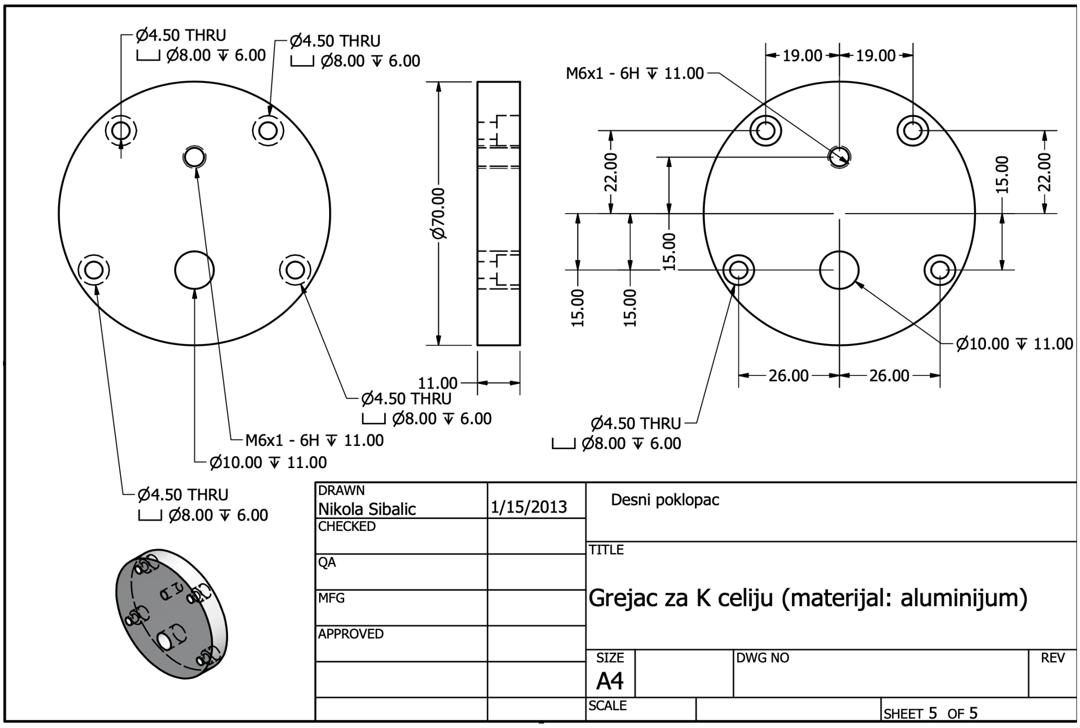

DRAWN
Nikola Sibalic 1/15/2013
CHECKED
QA
MFG
APPROVED

Desni poklopac

TITLE
Grejac za K celiju (materijal: aluminijum)

SIZE A4
DWG NO
REV
SCALE
SHEET 5 OF 5

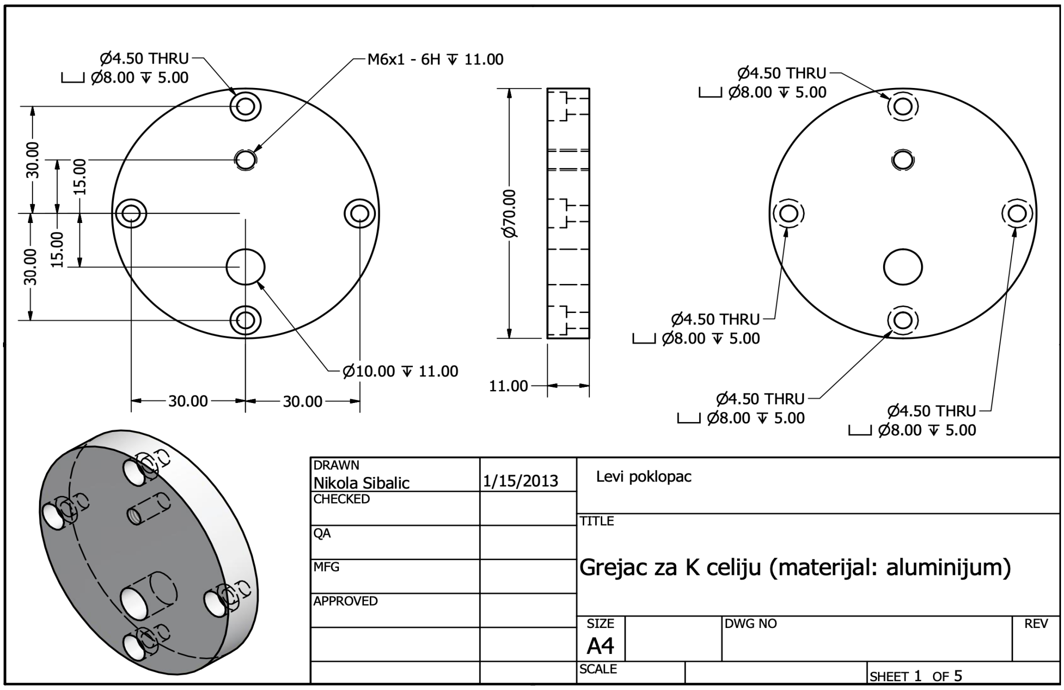

DRAWN
Nikola Sibalic 1/15/2013
CHECKED
QA
MFG
APPROVED

Levi poklopac

TITLE
Grejac za K celiju (materijal: aluminijum)

SIZE A4
DWG NO
REV
SCALE
SHEET 1 OF 5

A.2 Teflon thermal insulator

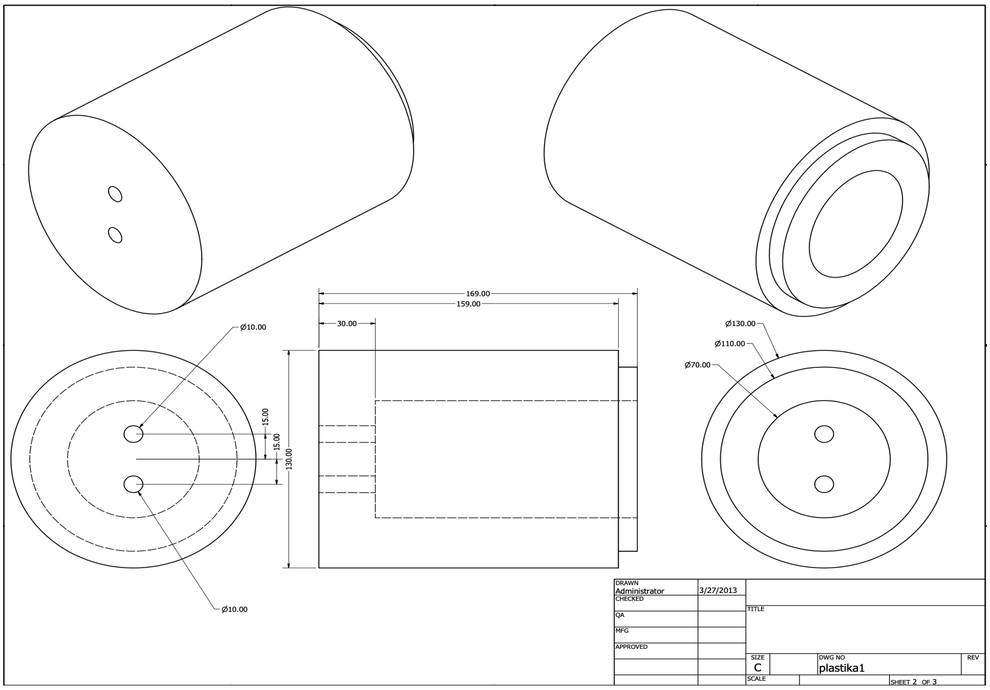

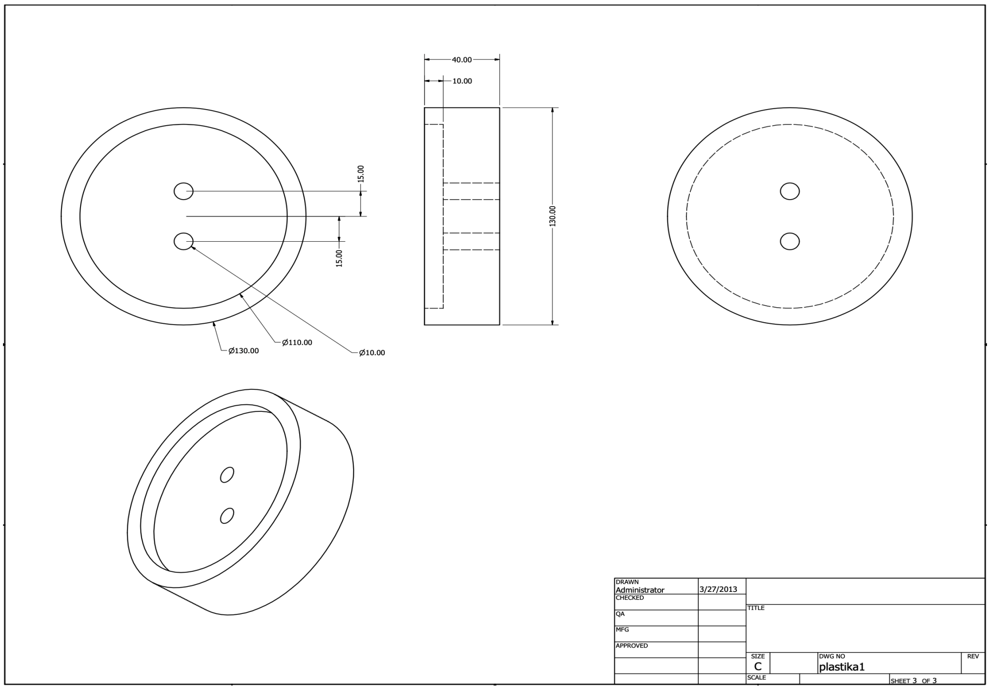

A.3 The temperature controller

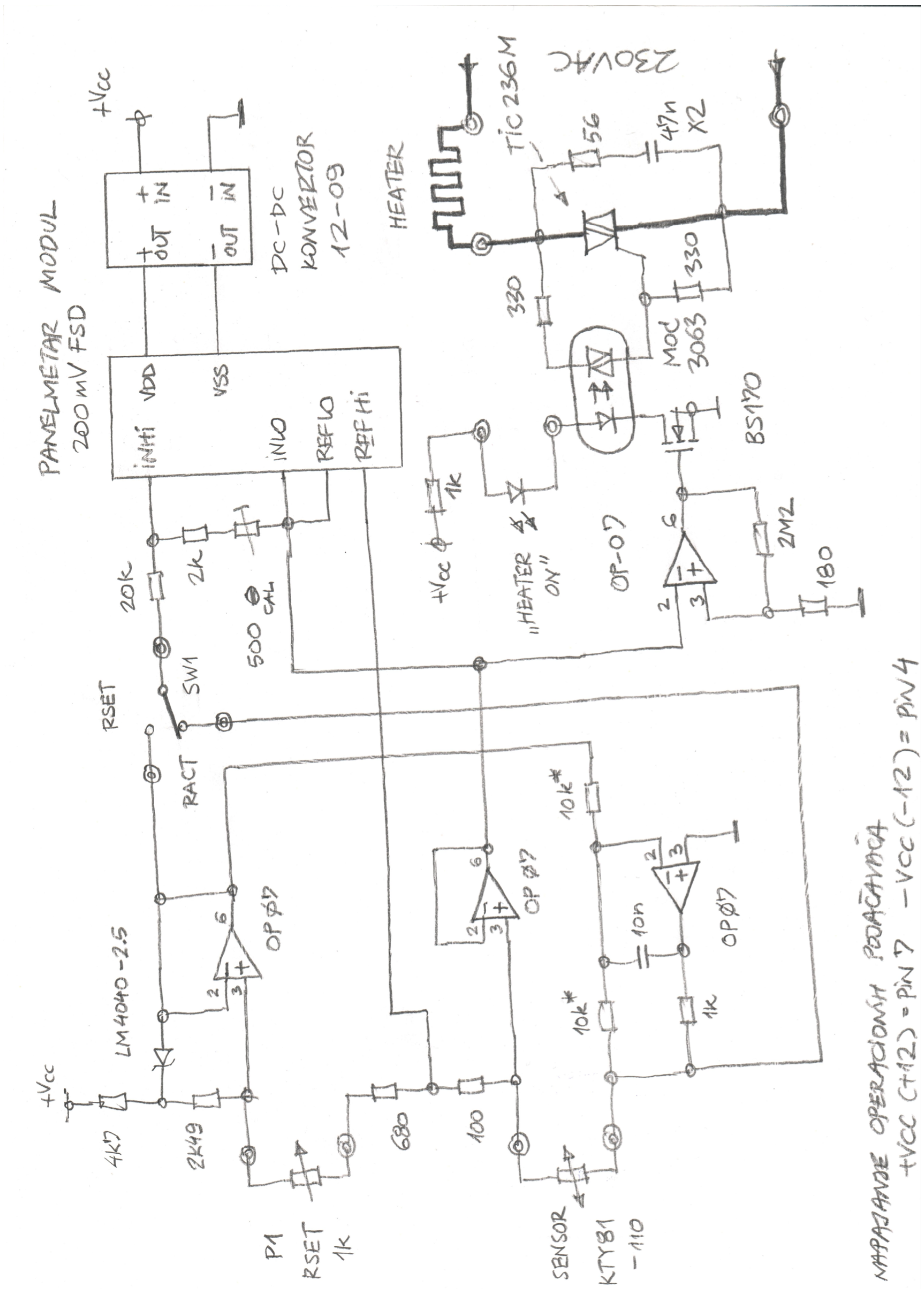

B Electro-optic modulator information

B.1 EOM Characteristics

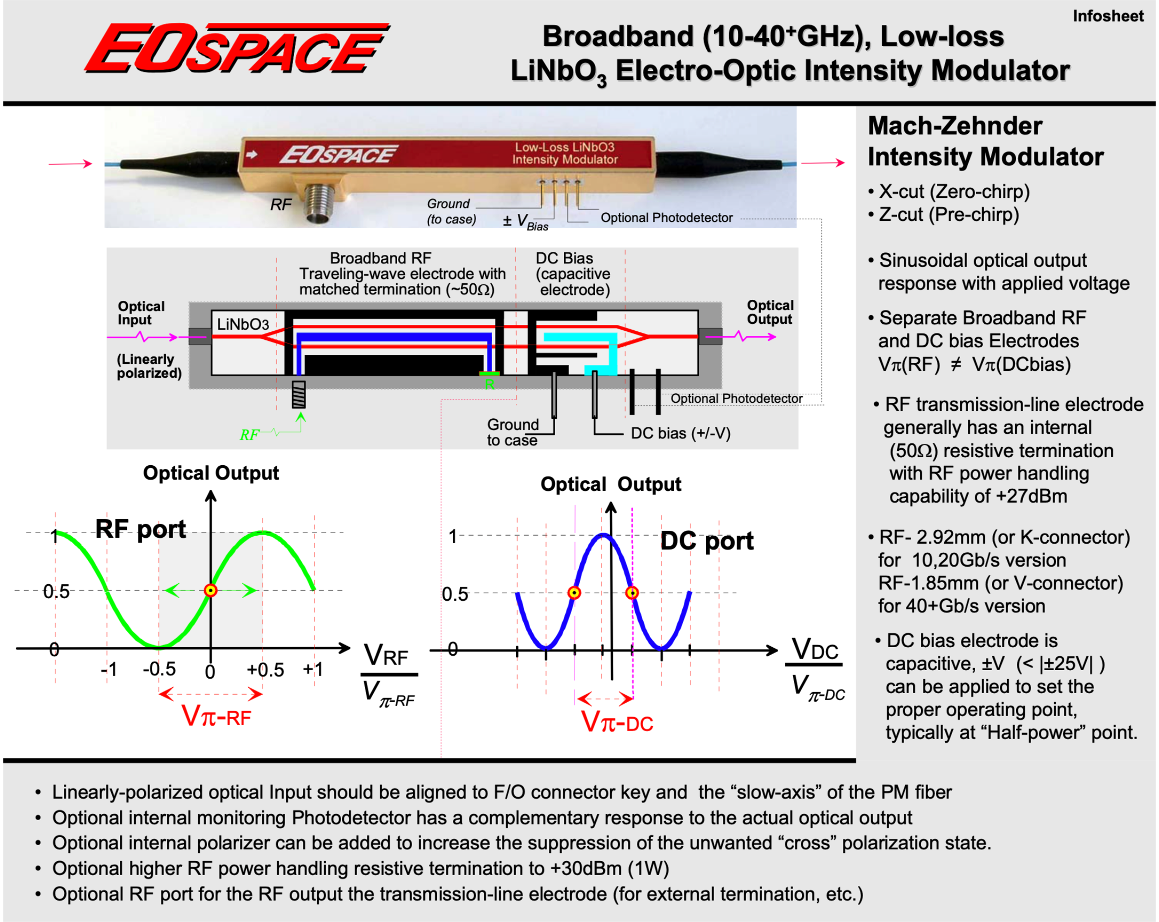

Broadband (10-40⁺GHz), Low-loss
$LiNbO_3$ Electro-Optic Intensity Modulator

Mach-Zehnder Intensity Modulator

- X-cut (Zero-chirp)
- Z-cut (Pre-chirp)

- Sinusoidal optical output response with applied voltage
- Separate Broadband RF and DC bias Electrodes Vπ(RF) ≠ Vπ(DCbias)
- RF transmission-line electrode generally has an internal (50Ω) resistive termination with RF power handling capability of +27dBm
- RF- 2.92mm (or K-connector) for 10,20Gb/s version RF-1.85mm (or V-connector) for 40+Gb/s version
- DC bias electrode is capacitive, ±V (< |±25V|) can be applied to set the proper operating point, typically at "Half-power" point.

- Linearly-polarized optical Input should be aligned to F/O connector key and the "slow-axis" of the PM fiber
- Optional internal monitoring Photodetector has a complementary response to the actual optical output
- Optional internal polarizer can be added to increase the suppression of the unwanted "cross" polarization state.
- Optional higher RF power handling resistive termination to +30dBm (1W)
- Optional RF port for the RF output the transmission-line electrode (for external termination, etc.)

B.2 EOM Measures

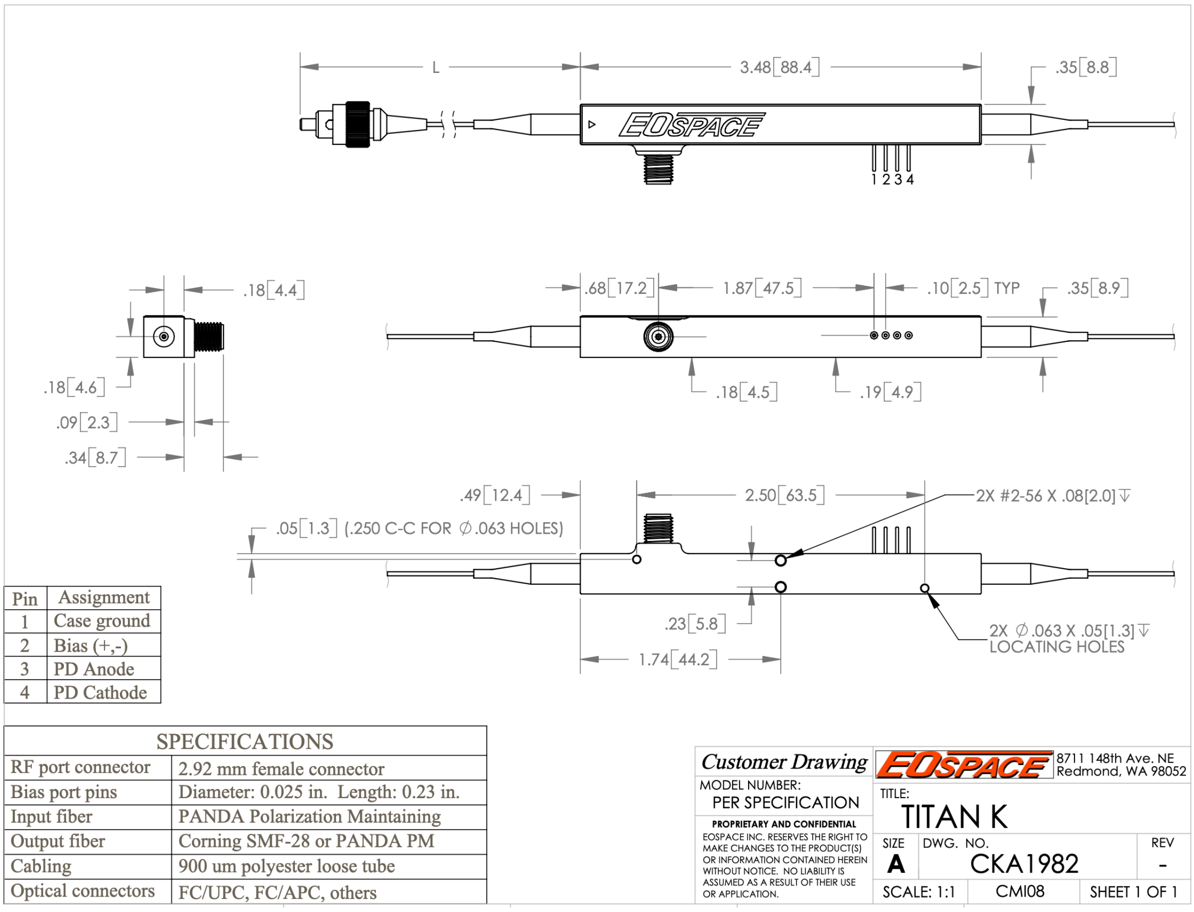

Pin	Assignment
1	Case ground
2	Bias (+,-)
3	PD Anode
4	PD Cathode

SPECIFICATIONS	
RF port connector	2.92 mm female connector
Bias port pins	Diameter: 0.025 in. Length: 0.23 in.
Input fiber	PANDA Polarization Maintaining
Output fiber	Corning SMF-28 or PANDA PM
Cabling	900 um polyester loose tube
Optical connectors	FC/UPC, FC/APC, others

Customer Drawing

EOSPACE

8711 148th Ave. NE
Redmond, WA 98052

MODEL NUMBER:
PER SPECIFICATION

TITLE:
TITAN K

PROPRIETARY AND CONFIDENTIAL

EOSPACE INC. RESERVES THE RIGHT TO MAKE CHANGES TO THE PRODUCT(S) OR INFORMATION CONTAINED HEREIN WITHOUT NOTICE. NO LIABILITY IS ASSUMED AS A RESULT OF THEIR USE OR APPLICATION.

SIZE	DWG. NO.	REV
A	CKA1982	-
SCALE: 1:1	CMI08	SHEET 1 OF 1

C Generation of Gaussian pulses

C.1 Trapezoidal to Gaussian signal converter

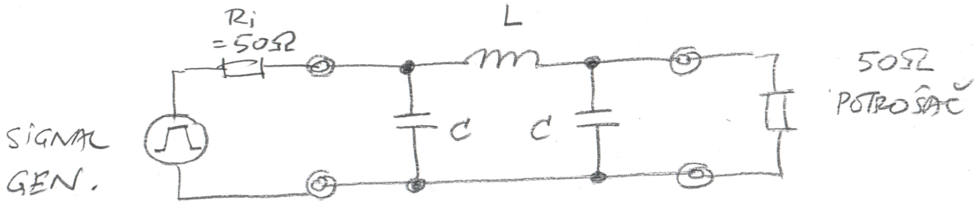

C.2 Table of circuit parameters for the generation of different Gausian pulses

	L	C	$t_r = t_f$	pw
T=20ns	160nH	127pF (120+6.8)	17ns	20ns
T=40ns	318nH	255pF (220+33)	34ns	40ns
T=80ns	637nH	509pF (470+39)	68ns	80ns
T=120ns	955nH	764pF (680+82)	101ns	120ns

Literature

[1] PA Franken, Alan E Hill, CW el Peters, and Gabriel Weinreich. Generation of optical harmonics. *Physical Review Letters*, 7(4):118, 1961.

[2] TH Maiman. Optical and microwave-optical experiments in ruby. *Physical review letters*, 4(11):564, 1960.

[3] JA Giordmaine. Mixing of light beams in crystals. *Physical Review Letters*, 8(1):19, 1962.

[4] Gisela Eckhardt, RW Hellwarth, FJ McClung, SE Schwarz, D Weiner, and EJ Woodbury. Stimulated raman scattering from organic liquids. *Physical Review Letters*, 9(11):455, 1962.

[5] G Alzetta, A Gozzini, and L Moi. Nuovo cimento b 36, 5 (1976); e. arimondo and g. orriols. *Lett. Nuovo Cimento*, 17:333, 1976.

[6] HR Gray, RM Whitley, and CR Stroud. Coherent trapping of atomic populations. *Optics letters*, 3(6):218–220, 1978.

[7] Stephen E Harris, JE Field, and A Imamoğlu. Nonlinear optical processes using electromagnetically induced transparency. *Physical Review Letters*, 64(10):1107, 1990.

[8] K-J Boller, A Imamoğlu, and Stephen E Harris. Observation of electromagnetically induced transparency. *Physical Review Letters*, 66(20):2593, 1991.

[9] JE Field, KH Hahn, and SE Harris. Observation of electromagnetically induced transparency in collisionally broadened lead vapor. *Physical review letters*, 67(22):3062, 1991.

[10] Marlan O Scully. Enhancement of the index of refraction via quantum coherence. *Physical Review Letters*, 67(14):1855, 1991.

[11] AS Zibrov, MD Lukin, Leo Hollberg, DE Nikonov, MO Scully, HG Robinson, and VL Velichansky. Experimental demonstration of enhanced index of refraction via quantum coherence in rb. *Physical review letters*, 76(21):3935, 1996.

[12] Stephen E Harris. Lasers without inversion: Interference of lifetime-broadened resonances. *Physical review letters*, 62(9):1033, 1989.

[13] Marlan O Scully, Shi-Yao Zhu, and Athanasios Gavrielides. Degenerate quantum-beat laser: Lasing without inversion and inversion without lasing. *Physical review letters*, 62(24):2813, 1989.

[14] AS Zibrov, MD Lukin, DE Nikonov, Leo Hollberg, MO Scully, VL Velichansky, and HG Robinson. Experimental demonstration of laser oscillation without population inversion via quantum interference in rb. *Physical Review Letters*, 75(8):1499, 1995.

[15] MD Lukin, PR Hemmer, M Löffler, and MO Scully. Resonant enhancement of parametric processes via radiative interference and induced coherence. *Physical review letters*, 81(13):2675, 1998.

[16] MD Lukin, PR Hemmer, and Marlan O Scully. Resonant nonlinear optics in phase-coherent media. *Advances in Atomic, Molecular, and Optical Physics*, 42:347–386, 2000.

[17] Boyd R. W. *Nonlinear Optics*. New York: Academic, 2003.

[18] Amnon Yariv and David M Pepper. Amplified reflection, phase conjugation, and oscillation in degenerate four-wave mixing. *Optics letters*, 1(1):16–18, 1977.

[19] David M Bloom, PF Liao, and NP Economou. Observation of amplified reflection by degenerate four-wave mixing in atomic sodium vapor. *Optics letters*, 2(3):58–60, 1978.

[20] JRR Leite, P Simoneau, D Bloch, S Le Boiteux, and M Ducloy. Continuous-wave phase-conjugate self-oscillation induced by na-vapour degenerate four-wave mixing with gain. *EPL (Europhysics Letters)*, 2(10):747, 1986.

[21] DS Glassner, B Ai, and RJ Knize. Low-intensity degenerate four-wave mixing at the cesium d1 resonance in thin cells. *Optics letters*, 19(24):2071–2073, 1994.

[22] B Ai and RJ Knize. Degenerate four-wave mixing in two-level saturable absorbers. *JOSA B*, 13(11):2408–2419, 1996.

[23] RT Bratfalean, GM Lloyd, and P Ewart. Degenerate four-wave mixing for arbitrary pump and probe intensities. *JOSA B*, 16(6):952–960, 1999.

[24] M Ducloy and D Bloch. Polarization properties of phase-conjugate mirrors: angular dependence and disorienting collision effects in resonant backward four-wave mixing for doppler-broadened degenerate transitions. *Physical Review A*, 30(6):3107, 1984.

[25] Martti Kauranen, Daniel J Gauthier, Michelle S Malcuit, and Robert W Boyd. Polarization properties of optical phase conjugation by two-photon resonant degenerate four-wave mixing. *Physical Review A*, 40(4):1908, 1989.

[26] E Köster, J Mlynek, and W Lange. Zeeman coherence effects in degenerate backward four-wave mixing: saturation studies on coupled transitions. *Optics communications*, 53(1):53–58, 1985.

[27] SM Wandzura. Effects of atomic motion on wavefront conjugation by resonantly enhanced degenerate four-wave mixing. *Optics Letters*, 4(7):208–210, 1979.

[28] DS Glassner and RJ Knize. Reduced angular dependence for degenerate four-wave mixing in potassium vapor by including nitrogen buffer gas. *Applied physics letters*, 66(13):1593–1595, 1995.

[29] AS Zibrov, MD Lukin, and Marlan O Scully. Nondegenerate parametric self-oscillation via multiwave mixing in coherent atomic media. *Physical Review Letters*, 83(20):4049, 1999.

[30] Tian Li, Ryan P Baker, and Jonathan D Weinstein. Degenerate four-wave mixing in atomic ytterbium. *JOSA B*, 29(10):2848–2851, 2012.

[31] Ken-ichi Harada, Kenji Mori, Junji Okuma, Nobuhito Hayashi, and Masaharu Mitsunaga. Parametric amplification in an electromagnetically-induced-transparency medium. *Physical Review A*, 78(1):013809, 2008.

[32] CF McCormick, Vincent Boyer, Ennio Arimondo, and PD Lett. Strong relative intensity squeezing by four-wave mixing in rubidium vapor. *Optics letters*, 32(2):178–180, 2007.

[33] Miaojun Guo, Haitao Zhou, Dan Wang, Jiangrui Gao, Junxiang Zhang, and Shiyao Zhu. Experimental investigation of high-frequency-difference twin beams in hot cesium atoms. *Physical Review A*, 89(3):033813, 2014.

[34] B Zlatković, AJ Krmpot, N Šibalić, M Radonjić, and BM Jelenković. Efficient parametric non-degenerate four-wave mixing in hot potassium vapor. *Laser Physics Letters*, 13(1):015205, 2015.

[35] R_E Slusher, LW Hollberg, Bernard Yurke, JC Mertz, and JF Valley. Observation of squeezed states generated by four-wave mixing in an optical cavity. *Physical review letters*, 55(22):2409, 1985.

[36] MD Reid and PD Drummond. Quantum correlations of phase in nondegenerate parametric oscillation. *Physical review letters*, 60(26):2731, 1988.

[37] PH Souto Ribeiro, Catherine Schwob, Agnès Maître, and Claude Fabre. Sub-shot-noise high-sensitivity spectroscopy with optical parametric oscillator twin beams. *Optics letters*, 22(24):1893–1895, 1997.

[38] Jiangrui Gao, Fuyun Cui, Chenyang Xue, Changde Xie, and Peng Kunchi. Generation and application of twin beams from an optical parametric oscillator including an?-cut ktp crystal. *Optics letters*, 23(11):870–872, 1998.

[39] Raphael C Pooser and Benjamin Lawrie. Ultrasensitive measurement of microcantilever displacement below the shot-noise limit. *Optica*, 2(5):393–399, 2015.

[40] Vincent Boyer, Alberto M Marino, Raphael C Pooser, and Paul D Lett. Entangled images from four-wave mixing. *Science*, 321(5888):544–547, 2008.

[41] Samuel L Braunstein and Peter Van Loock. Quantum information with continuous variables. *Reviews of modern physics*, 77(2):513, 2005.

[42] John S Bell. On the einstein podolsky rosen paradox. *Physics Physique Fizika*, 1(3):195, 1964.

[43] Tomasz Wasak, Augusto Smerzi, and Jan Chwedeńczuk. Role of particle entanglement in the violation of bell inequalities. *Scientific Reports*, 8(1):1–6, 2018.

[44] L-M Duan, Mikhail D Lukin, J Ignacio Cirac, and Peter Zoller. Long-distance quantum communication with atomic ensembles and linear optics. *Nature*, 414(6862):413–418, 2001.

[45] Ryan M Camacho, Praveen K Vudyasetu, and John C Howell. Four-wave-mixing stopped light in hot atomic rubidium vapour. *Nature Photonics*, 3(2):103–106, 2009.

[46] Alberto M Marino, Raphael C Pooser, Vincent Boyer, and Paul D Lett. Tunable delay of einstein–podolsky–rosen entanglement. *Nature*, 457(7231):859–862, 2009.

[47] RW Boyd and DJ Gauthier. Slow and fast light. *Progress in Optics vol 43,*, 2002.

[48] Jacob B Khurgin and Rodney S Tucker. *Slow light: Science and applications.* CRC press, 2018.

[49] Lene Vestergaard Hau, Stephen E Harris, Zachary Dutton, and Cyrus H Behroozi. Light speed reduction to 17 metres per second in an ultracold atomic gas. *Nature*, 397(6720):594–598, 1999.

[50] Michael M Kash, Vladimir A Sautenkov, Alexander S Zibrov, Leo Hollberg, George R Welch, Mikhail D Lukin, Yuri Rostovtsev, Edward S Fry, and Marlan O Scully. Ultraslow group velocity and enhanced nonlinear optical effects in a coherently driven hot atomic gas. *Physical Review Letters*, 82(26):5229, 1999.

[51] Ryan M Camacho, Michael V Pack, and John C Howell. Low-distortion slow light using two absorption resonances. *Physical Review A*, 73(6):063812, 2006.

[52] M Klein, M Hohensee, Y Xiao, R Kalra, David F Phillips, and Ronald Lee Walsworth. Slow-light dynamics from electromagnetically-induced-transparency spectra. *Physical Review A*, 79(5):053833, 2009.

[53] Jiepeng Zhang, Gessler Hernandez, and Yifu Zhu. Slow light with cavity electromagnetically induced transparency. *Optics letters*, 33(1):46–48, 2008.

[54] Ryan M Camacho, Michael V Pack, John C Howell, Aaron Schweinsberg, and Robert W Boyd. Wide-bandwidth, tunable, multiple-pulse-width optical delays using slow light in cesium vapor. *Physical review letters*, 98(15):153601, 2007.

[55] BS Ham and J Hahn. Coherent dynamics of self-induced ultraslow light for all-optical switching. *Optics letters*, 33(23):2880–2882, 2008.

[56] Yoshitomo Okawachi, Matthew S Bigelow, Jay E Sharping, Zhaoming Zhu, Aaron Schweinsberg, Daniel J Gauthier, Robert W Boyd, and Alexander L Gaeta. Tunable all-optical delays via brillouin slow light in an optical fiber. *Physical review letters*, 94(15):153902, 2005.

[57] Elisa Baldit, Kamel Bencheikh, Paul Monnier, Juan Ariel Levenson, and Vincent Rouget. Ultraslow light propagation in an inhomogeneously broadened rare-earth ion-doped crystal. *Physical Review Letters*, 95(14):143601, 2005.

[58] Hai-Hua Wang, Yun-Fei Fan, Rong Wang, Lei Wang, Dun-Mao Du, Zhi-Hui Kang, Yun Jiang, Jin-Hui Wu, and Jin-Yue Gao. Slowing and storage of double light pulses in a pr 3+: Y 2 sio 5 crystal. *Optics letters*, 34(17):2596–2598, 2009.

[59] AV Turukhin, VS Sudarshanam, MS Shahriar, JA Musser, BS Ham, and PR Hemmer. Observation of ultraslow and stored light pulses in a solid. *Physical Review Letters*, 88(2):023602, 2001.

[60] Matthew S Bigelow, Nick N Lepeshkin, and Robert W Boyd. Superluminal and slow light propagation in a room-temperature solid. *Science*, 301(5630):200–202, 2003.

[61] Jay E Sharping, Yoshitomo Okawachi, and Alexander L Gaeta. Wide bandwidth slow light using a raman fiber amplifier. *Optics Express*, 13(16):6092–6098, 2005.

[62] Jiepeng Zhang, Gessler Hernandez, and Yifu Zhu. Copropagating superluminal and slow light manifested by electromagnetically assisted nonlinear optical processes. *Optics letters*, 31(17):2598–2600, 2006.

[63] KJ Jiang, L Deng, and MG Payne. Ultraslow propagation of an optical pulse in a three-state active raman gain medium. *Physical Review A*, 74(4):041803, 2006.

[64] A Eilam, AD Wilson-Gordon, and H Friedmann. Slow and stored light in an amplifying double-λ system. *Optics letters*, 33(14):1605–1607, 2008.

[65] Nikolai Lauk, Christopher O'Brien, and Michael Fleischhauer. Fidelity of photon propagation in electromagnetically induced transparency in the presence of four-wave mixing. *Physical Review A*, 88(1):013823, 2013.

[66] Ya-Fen Hsiao, Pin-Ju Tsai, Chi-Ching Lin, Yong-Fan Chen, A Yu Ite, and Ying-Cheng Chen. Coherence properties of amplified slow light by four-wave mixing. *Optics letters*, 39(12):3394–3397, 2014.

[67] Ying Wu and Xiaoxue Yang. Highly efficient four-wave mixing in double-λ system in ultraslow propagation regime. *Physical Review A*, 70(5):053818, 2004.

[68] Yanpeng Zhang, Andy W Brown, and Min Xiao. Matched ultraslow propagation of highly efficient four-wave mixing in a closely cycled double-ladder system. *Physical Review A*, 74(5):053813, 2006.

[69] V Boyer, CF McCormick, Ennio Arimondo, and Paul D Lett. Ultraslow propagation of matched pulses by four-wave mixing in an atomic vapor. *Physical review letters*, 99(14):143601, 2007.

[70] Caspar H van der Wal, Matthew D Eisaman, Axel André, Ronald L Walsworth, David F Phillips, Alexander S Zibrov, and Mikhail D Lukin. Atomic memory for correlated photon states. *Science*, 301(5630):196–200, 2003.

[71] CF McCormick, Alberto M Marino, Vincent Boyer, and Paul D Lett. Strong low-frequency quantum correlations from a four-wave-mixing amplifier. *Physical Review A*, 78(4):043816, 2008.

[72] Quentin Glorieux, Luca Guidoni, Samuel Guibal, Jean-Pierre Likforman, and Thomas Coudreau. Quantum correlations by four-wave mixing in an atomic vapor in a nonamplifying regime: Quantum beam splitter for photons. *Physical Review A*, 84(5):053826, 2011.

[73] Martijn Jasperse, LD Turner, and RE Scholten. Relative intensity squeezing by four-wave mixing with loss: an analytic model and experimental diagnostic. *Optics express*, 19(4):3765–3774, 2011.

[74] Junji Okuma, Nobuhito Hayashi, Akihiko Fujisawa, and Masaharu Mitsunaga. Ultraslow matched-pulse propagation in sodium vapor. *Optics letters*, 34(11):1654–1656, 2009.

[75] B Zlatković, MM Ćurčić, IS Radojičić, D Arsenović, AJ Krmpot, and BM Jelenković. Slowing probe and conjugate pulses in potassium vapor using four wave mixing. *Optics Express*, 26(26):34266–34273, 2018.

[76] Tobias Tiecke. Properties of potassium.

[77] MT Turnbull, PG Petrov, CS Embrey, AM Marino, and V Boyer. Role of the phase-matching condition in nondegenerate four-wave mixing in hot vapors for the generation of squeezed states of light. *Physical Review A*, 88(3):033845, 2013.

[78] PR Hemmer, DP Katz, J Donoghue, M Cronin-Golomb, MS Shahriar, and Prem Kumar. Efficient low-intensity optical phase conjugation based on coherent population trapping in sodium. *Optics letters*, 20(9):982–984, 1995.

[79] Y R Shen. Principles of nonlinear optics. 1 1984.

[80] Nicolaas Bloembergen and Yuen-Ron Shen. Quantum-theoretical comparison of nonlinear susceptibilities in parametric media, lasers, and raman lasers. *Physical Review*, 133(1A):A37, 1964.

[81] Bahaa EA Saleh, Malvin Carl Teich, and OF FUNDAMENTALS. *Photonics*. Wiley, 2019.

[82] CB Alcock, VP Itkin, and MK Horrigan. Vapour pressure equations for the metallic elements: 298–2500k. *Canadian Metallurgical Quarterly*, 23(3):309–313, 1984.

[83] H Schnatz, G Grosche, E Tiemann, Ch Lisdat, et al. The transition frequencies of the d lines of 39k, 40k, and 41k measured with a femtosecond laser frequency comb. In *Quantum Electronics and Laser Science Conference*, page JTuD61. Optical Society of America, 2006.

[84] Ennio Arimondo, M Inguscio, and P Violino. Experimental determinations of the hyperfine structure in the alkali atoms. *Reviews of Modern Physics*, 49(1):31, 1977.

[85] Wolfgang Demtröder. *Laser spectroscopy 1: basic principles*. Springer, 2014.

[86] D Bloch, M Ducloy, N Senkov, V Velichansky, and V Yudin. Doppler-free spectroscopy of the d˜ 1 line of potassium. *LASER PHYSICS-LAWRENCE-*, 6:670–678, 1996.

[87] Tony J Rouphael. *RF and digital signal processing for software-defined radio: a multi-standard multi-mode approach*. Newnes, 2009.

[88] Matthew Newville, Till Stensitzki, Daniel B Allen, Michal Rawlik, Antonino Ingargiola, and Andrew Nelson. Lmfit: Non-linear least-square minimization and curve-fitting for python. *Astrophysics Source Code Library*, pages ascl–1606, 2016.

[89] MD Lukin and Ataç Imamoğlu. Controlling photons using electromagnetically induced transparency. *Nature*, 413(6853):273–276, 2001.

[90] Michael Fleischhauer, Atac Imamoglu, and Jonathan P Marangos. Electromagnetically induced transparency: Optics in coherent media. *Reviews of modern physics*, 77(2):633, 2005.